Prostate Registration Using Magnetic Resonance Elastography for Cancer Localization

by

Guy Nir

B.Sc., Technion – Israel Institute of Technology, 2006
M.Sc., Technion – Israel Institute of Technology, 2010

A THESIS SUBMITTED IN PARTIAL FULFILLMENT OF
THE REQUIREMENTS FOR THE DEGREE OF

DOCTOR OF PHILOSOPHY

in

The Faculty of Graduate and Postdoctoral Studies

(Electrical and Computer Engineering)

THE UNIVERSITY OF BRITISH COLUMBIA

(Vancouver)

December 2014

© Guy Nir 2014

Abstract

Noninvasive detection and localization of prostate cancer in medical imaging is an important, yet difficult task. Benefits range from diagnosis of cancer, to planning and guidance of its treatment. In order to characterize cancer and evaluate its localization in volumetric images, such as ultrasound or magnetic resonance imaging (MRI), their spatial correspondence with the "gold standard" provided by histopathology must be established.

In this thesis, we propose a general framework for a multi-slice to volume registration that is applied to register a stack of sparse, unaligned two-dimensional histological slices to a three-dimensional volumetric imaging of the prostate. The approach uses particle filtering that allows deriving optimal pose parameters of the slices in a Bayesian approach.

We then propose a novel registration method between *in vivo* and *ex vivo* MRI of the prostate to facilitate its registration to histopathology. The method incorporates elasticity information, acquired by magnetic resonance elastography (MRE), to generate a patient-specific biomechanical model of the prostate and periprostatic tissue.

Next, we propose a registration method between preoperative MRI and intraoperative transrectal-ultrasound. The method can be incorporated with a robotic surgical system to augment the surgeon's visualization during robot-assisted prostatectomy. We also study the use of elasticity-based registration of ultrasound elastography and MRE.

We then present an image processing approach for enhancing MRE data. The approach employs registration to compensate for motion of patients during the scan to improve the accuracy of the reconstructed elastogram. A super-resolution technique is employed to increase the resolution of the acquired images by utilizing unique properties of MRE.

Finally, we develop a theory for optimization-based design of motion encoding in MRE that allows reducing scanning time and increasing signal-to-noise ratio of elasticity reconstruction. We formulate the displacement estimation of the mechanical wave as an experimental design problem, by which we quantify performance of sequences, and optimize multidirectional designs.

The proposed methods have been evaluated in simulations and on a diverse set of clinical data. Results may pave the way for a broader clinical deployment of elastography and elastography-based image processing.

Preface

This thesis is based on several manuscripts, resulting from collaboration between multiple researchers. All publications have been modified to make the thesis a coherent document. Ethical approval for conducting this research has been provided by the Clinical Research Ethics Board, certificate numbers: H09-03163, H08-02696.

- A version of Chapter 2 has been published as:

  G. Nir, R. S. Sahebjavaher, P. Kozlowski, S. D. Chang, E. C. Jones, S. L. Goldenberg, and S. E. Salcudean, "Registration of whole-mount histology and volumetric imaging of the prostate using particle filtering," *IEEE Transactions on Medical Imaging*, 2014, vol. 33, no. 8, pp. 1601–1613.

  The author's contribution in that article was proposing and developing the idea, formulating and implementing the algorithm, conducting numerical simulations, collecting the data, conducing the experiments, evaluating the results, and writing the manuscript. Dr. Sahebjavaher contributed to the MRI data collection, sectioning the specimens, and scanning the histological slides. Dr. Kozlowski contributed to the 7-Tesla MRI data collection and provided the histology sectioning device. Dr. Chang assisted in segmentation of the data and identification of corresponding landmarks. Dr. Jones processed the whole-mount histological slices and provided the histopathological analysis. Dr. Goldenberg contributed to the US data collection, performed the radical prostatectomy procedures, and provided the postoperative specimens. Dr. Salcudean provided guidance, support, and assisted in editing the manuscript.

- A version of Chapter 3 has been published as:

  G. Nir, R. S. Sahebjavaher, P. Kozlowski, S. D. Chang, R. Sinkus, S. L. Goldenberg, and S. E. Salcudean, "Model-based registration of *ex vivo* and *in vivo* MRI of the prostate using elastography," *IEEE Transactions on Medical Imaging*, 2013, vol. 32, no. 7, pp. 1349–1361.

  The author's contribution in that article was proposing and developing the idea, formulating and implementing the algorithm, conducting numerical simulations, collecting the data, conducing the experiments, evaluating the results, and writing the manuscript. Dr. Sahebjavaher contributed to the article through discussions and collected the MRI data. Dr. Kozlowski contributed to the article through discussions and assisted with the 7-Tesla MRI data collection. Dr. Chang assisted in segmentation of the data and identification of corresponding landmarks. Dr. Sinkus helped to set up the MRE system at UBC. Dr. Goldenberg performed the radical prostatectomy procedures and provided the postoperative specimens. Dr. Salcudean provided guidance, support, and assisted in editing the manuscript.

- A version of Chapter 6 is in press for publication as:

  G. Nir, R. S. Sahebjavaher, R. Sinkus, and S. E. Salcudean, "A framework for optimization-based design of motion encoding in magnetic resonance elastography," *Magnetic Resonance in Medicine*, 2014, DOI: 10.1002/mrm.25280.

  The author's contribution in that article was proposing and developing the idea, providing mathematical formulation and analysis, conducting numerical simulations, collecting the phantom data, processing the data, evaluating the results, and writing the manuscript. Dr. Sahebjavaher contributed to the article through discussions, implemented the proposed MRI pulse sequences, collected the phantom data, provided the code for phase unwrapping, and assisted in editing the manuscript. Dr. Sinkus helped to set up the MRE system at UBC, contributed to the article through discussions, and assisted in editing the manuscript. Dr. Salcudean provided guidance, support, and assisted in editing the manuscript.

- A version of Chapter 4 is to be submitted as:

  G. Nir, R. S. Sahebjavaher, J. Lobo, O. Mohareri, S. S. Mahdavi, and S. E. Salcudean, "Registration of Ultrasound and Magnetic Resonance Imaging for Image Guided Robot-Assisted Prostatectomy,"

  The author's contribution in this work was developing and implementing the registration algorithms, conducting numerical simulations, collecting the phantom data, assisting in collection of patient data, processing the data, evaluating the results, and writing the manuscript. Dr. Sahebjavaher collected the phantom and patient MRI and MRE data, contributed to the work through discussions, and assisted in editing the manuscript. Mr. Lobo and Mr. Mohareri collected the phantom and patient US and USE data, assisted in integration of the algorithm with the da Vinci system, contributed to the work through discussions, and assisted in editing the manuscript. Dr. S. S. Mahdavi provided the code and support for the semi-automatic segmentation algorithm. Dr. Salcudean provided guidance, support, and assisted in editing the manuscript. In addition, Ms. S. Rashid and Ms. A. Ruszkowski provided evaluation of the surface-to-surface registration algorithm.

- A version of Chapter 5 is to be submitted as:

  G. Nir, R. S. Sahebjavaher, M. Honarvar, and S. E. Salcudean, "Motion Compensation and Super-Resolution in Magnetic Resonance Elastography,"

  The author's contribution in this work was proposing, developing and implementing the motion compensation and super-resolution idea, conducting numerical simulations, collecting the phantom data, assisting in collection of patient data, processing the data, evaluating the results, and writing the manuscript. Dr. Sahebjavaher collected the phantom and patient data, contributed to the work through discussions, and assisted in editing the manuscript. Mr. Honarvar provided reconstruction of the elastograms for the motion compensated data, contributed to the work through discussions, and assisted in editing the manuscript. Dr. Salcudean provided guidance, support, and assisted in editing the manuscript.

Portions of the above papers, mainly introductory text, figures and literature review, also appear in Chapter 1.

Table of Contents

Abstract ii

Preface iii

Table of Contents vi

List of Tables x

List of Figures xi

List of Abbreviations xiii

Acknowledgements xv

Dedication xvi

1 Introduction 1
- 1.1 Background and Motivation 1
  - 1.1.1 Prostate Anatomy and Prostate Cancer Interventions 1
  - 1.1.2 Imaging of the Prostate 3
  - 1.1.3 Elastography of the Prostate 4
  - 1.1.4 Whole-Mount Histopathology of the Prostate 6
  - 1.1.5 Prostate Registration 7
- 1.2 Thesis Objectives 9
- 1.3 Thesis Outline 9

2 Registration of Whole-Mount Histology and Volumetric Imaging of the Prostate 11
- 2.1 Introduction 11
- 2.2 Problem Formulation 15
  - 2.2.1 Slice Transformation and Volume Re-Slicing 15

2.2.2 Multi-Slice to Volume Registration 16
2.3 Particle Filtering 17
2.3.1 Prediction Model 18
2.3.2 Observation Model 19
2.3.3 Initial State 19
2.3.4 Particle Filtering Algorithm 20
2.3.5 Similarity Metrics 24
2.4 Experiments 26
2.4.1 Synthetic Case 26
2.4.2 Clinical Data Acquisition 27
2.4.3 Parameter Selection and Implementation Details 30
2.4.4 Results 31
2.5 Discussion and Conclusion 34

3 Model-Based Registration of the Prostate Using Elastography 37
3.1 Introduction 37
3.2 Preliminaries 39
3.2.1 Elastic Registration 39
3.2.2 Region-Based Active Contours 40
3.2.3 Model-Based Alignment 42
3.3 Model-Based Registration Using Inhomogeneous Elasticity 43
3.3.1 Model-Based Force 43
3.3.2 Inhomogeneous Regularization 44
3.3.3 Energy Minimization 44
3.3.4 Synthetic Example 45
3.3.5 Clinical Example 47
3.4 Elastic Homogeneity Versus Inhomogeneity 48
3.5 Experiments 51
3.5.1 Data Acquisition 51
3.5.2 Implementation Details 53
3.5.3 Results 53
3.6 Discussion and Conclusion 57

4 Registration of Ultrasound and Magnetic Resonance Imaging for Image Guided Interventions 60
4.1 Introduction 60

4.2 Problem Formulation 62
4.3 Segmentation-Based Registration 63
    4.3.1 Semi-Automatic Prostate Segmentation in TRUS 63
    4.3.2 Registration Process 64
    4.3.3 Results 65
    4.3.4 Application in MR-Guided RALP 68
4.4 Elasticity-Based Registration 68
    4.4.1 Registration Process 69
4.5 Discussion and Conclusion 72

5 Motion Compensation and Super-Resolution in Magnetic Resonance Elastography 74
5.1 Introduction 74
5.2 Methods 75
    5.2.1 Motion Compensation Using Registration 75
    5.2.2 Super-Resolution in MRE 76
5.3 Results 78
    5.3.1 Phantom Experiment 78
    5.3.2 Patients' Data 80
5.4 Discussion and Conclusion 81

6 Optimization-Based Design of Motion Encoding in Magnetic Resonance Elastography 84
6.1 Introduction 84
6.2 Theory 87
    6.2.1 Parameterized Motion Encoding Gradients 87
    6.2.2 Parameterized Phase Accumulation 87
    6.2.3 Optimal Estimation of Wave Properties 89
    6.2.4 Optimal Design of Motion Encoding 90
    6.2.5 Unidirectional Designs 91
    6.2.6 Multidirectional RME Design 92
    6.2.7 Optimal Design with Varying Start Phases 94
    6.2.8 Optimal Design with Varying Phase Shifts 96
6.3 Methods 97
    6.3.1 Simulation of a Plane Wave 97
    6.3.2 Phantom Experiment 99

6.4 Results 101
    6.4.1 Simulation of a Plane Wave 101
    6.4.2 Phantom Experiment 101
6.5 Discussion and Conclusion 102

7 Conclusion 107
7.1 Contributions and Limitations 108
7.2 Future Work 112

Bibliography 114

Appendix

A Derivation of the Parameterized Phase Accumulation 131

List of Tables

2.1 Summary of the parameters. 28
2.2 Registration results 33

3.1 MRE results 52
3.2 Registration results 56

4.1 Segmentation-based registration results. 66

5.1 Super-resolution results on clinical data 82

6.1 Summary and description of the notations 86
6.2 Phantom results 102

List of Figures

1.1 Prostate anatomy with major anatomical landmarks 2
1.2 Imaging of the prostate 3
1.3 MRE of the prostate 5
1.4 TRUS-VE of the prostate 6
1.5 Thesis outline 10

2.1 Problem illustration 12
2.2 Random particles 17
2.3 Similarity metrics 22
2.4 Registration of synthetic data: illustration 25
2.5 Registration of synthetic data: sensitivity analysis 27
2.6 Registration results 32

3.1 Problem illustration 38
3.2 Registration of synthetic images 45
3.3 Registration of noisy synthetic images 46
3.4 Mean displacement error 47
3.5 Registration process 48
3.6 Inhomogeneity parameter 49
3.7 Difference maps 50
3.8 Inhomogeneity parameter performance 51
3.9 Inhomogeneous registration results 55
3.10 Inhomogeneous registration results 57

4.1 Problem illustration 62
4.2 Semi-automatic segmentation. 64
4.3 Segmentation-based registration 65
4.4 Proposed augmented visualization 67
4.5 Elasticity-based registration of a phantom 70

4.6 Elasticity-based registration of patient data 71

5.1 Motion compensation 77
5.2 Super-resolution of a phantom MRE 79
5.3 Phantom errors 80
5.4 Super-resolution of a patient's prostate MRE 81

6.1 Example of MEGs sequence 88
6.2 RME design 93
6.3 MD-RME design 95
6.4 Optimal design with varying start phases 96
6.5 Optimal design with varying phase shifts 98
6.6 Simulation results 99
6.7 Phantom data 100
6.8 Simulation errors 101
6.9 Phantom results 103
6.10 Phantom errors 104

7.1 Clinical flow 108

List of Abbreviations

2-D two-dimensional

3-D three-dimensional

CaP carcinoma of the prostate

DFT discrete Fourier transform

DRE digital rectal examination

EPI echo-planar imaging

FEM finite element method

FSE fast spin-echo

FOV field of view

i.i.d. identically and independently distributed

LFE local frequency estimation

MAP maximum *a posteriori*

MD-RME multidirectional reduced motion encoding

MEG motion encoding gradient

MI mutual information

MR magnetic resonance

MRE magnetic resonance elastography

MRI magnetic resonance imaging

MSE mean squared error

NCC normalized cross-correlation

PDE partial differential equation

pdf probability density function

PF particle filter

PSA prostate-specific antigen

RALP robot-assisted laparoscopic radical prostatectomy

RF radio-frequency

RME reduced motion encoding

SE spin-echo

SNR signal-to-noise ratio

STDV standard deviation

SSD sum of squared differences

T2w T2-weighted

TE echo time

TR pulse repetition time

TRE target registration error

TRUS transrectal ultrasound

US ultrasound

USE ultrasound elastography

VE vibro-elastography

Acknowledgements

I sincerely thank my supervisor, Professor Septimiu (Tim) E. Salcudean, for his support throughout the course of this work. His knowledge, experience, and constructive criticism, both on the professional and personal levels, are invaluable.

I thank my fellow members of the Robotics and Control Laboratory for their collaboration and friendship during these years at UBC.

I further thank my collaborators at Vancouver General Hospital, BC Cancer Agency, and the UBC MRI Research Centre for their time, help and fruitful discussions.

Last but not least, I thank my family for their love and support, with a special gratitude to Moran.

To Carmel –

the evergreen mountain in my life

Chapter 1

Introduction

1.1 Background and Motivation

1.1.1 Prostate Anatomy and Prostate Cancer Interventions

The prostate is a fibromuscular gland about the size and shape of a walnut that lies at a low level in the lesser pelvis, and is traversed by the urethra and ejaculatory ducts [48]. Being somewhat pyramidal, it presents a base superiorly, an apex inferiorly, and surfaces anteriorly, posteriorly and laterally. The prostate surrounds the prostatic urethra and is encompassed superiorly by the bladder neck, inferiorly by the urogenital diaphragm, anteriorly by the *symphysis pubis* and pubic arch, and posteriorly by the rectum wall (Figure 1.1). The glandular tissue may be subdivided into three distinct zones: peripheral (70% by volume), central (25% by volume), and transition (5% by volume).

With an estimated number of 233,000 new cases and 29,480 deaths in 2014, prostate cancer is the most commonly diagnosed cancer and second most common cause of cancer death among American men [6]. Prostate cancer, also known as carcinoma of the prostate (CaP), occurs mostly in the peripheral zone of the prostate, followed by the transition zone, then by the central zone. In its early stages, CaP has no symptoms and is usually suspected when a prostate-specific antigen (PSA) test has shown a significant increase and/or when a digital rectal examination (DRE) shows stiff nodules or an asymmetric gland. Diagnosis cannot be confirmed until a biopsy test is returned positive.

Clinical management of CaP is based on combination of the patient's physical condition (e.g., age, weight, other health issues), tumor staging, tumor grading, and PSA [114]. In the Gleason grading system, a grade is assigned by a pathologist to the most- and second-most dominant microscopic patterns of a tumor based on histopathology analysis. Each grade ranges from one to five, representing well- to poorly-differentiated carcinoma, respectively. The final Gleason score is the sum of the primary and secondary grades.

There are various treatment methods available to CaP patients. These include watchful waiting, hormone therapy, chemotherapy, external beam radiation therapy, low/high dose rate brachytherapy, and high-intensity focused ultrasound. Radical prostatectomy, i.e., the

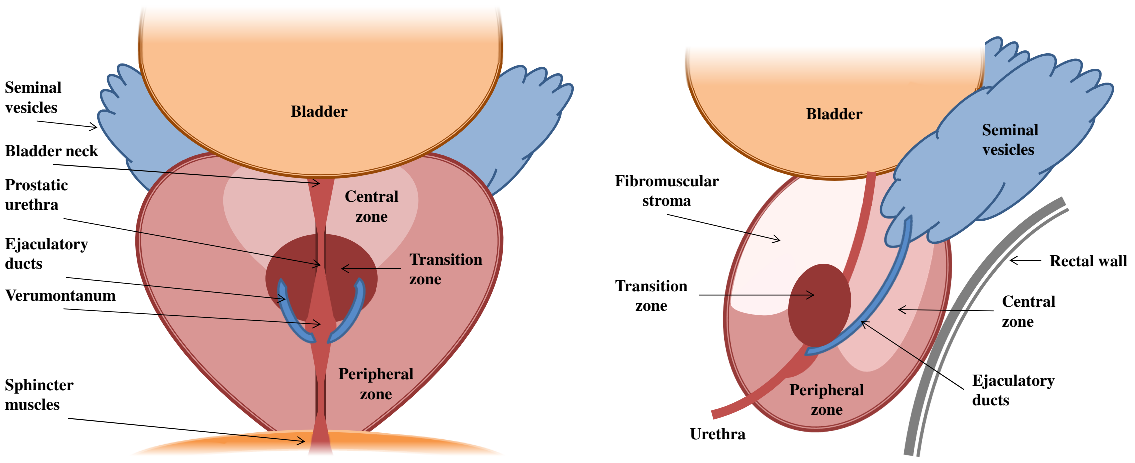
Seminal vesicles
Bladder neck
Prostatic urethra
Ejaculatory ducts
Verumontanum
Sphincter muscles
Bladder
Central zone
Transition zone
Peripheral zone
Bladder
Seminal vesicles
Fibromuscular stroma
Transition zone
Rectal wall
Central zone
Ejaculatory ducts
Peripheral zone
Urethra

(a) Coronal cross-section (b) Sagittal cross-section

Figure 1.1: Prostate anatomy with major anatomical landmarks.

surgical extirpation of the prostate, is viewed by many as the "gold standard" treatment for clinically localized CaP. The long term prognosis of patients who undergo prostatectomy has improved significantly over the past few decades. However, there remain significant rates of disease recurrence and complications. In addition to regular risks of a surgical procedure, common complications include incontinence and impotence. Therefore, the primary goals of prostatectomy are (i) cancer control, (ii) preservation of urinary continence, and (iii) preservation of erectile function.

The state-of-the-art radical prostatectomy technique is the minimally invasive robot-assisted laparoscopic radical prostatectomy (RALP), which involves a robotic surgery system (da Vinci Surgical System, Intuitive Surgical, Sunnyvale, CA). Compared with the open prostatectomy and standard laparoscopic prostatectomy techniques, RALP provides the surgeon with excellent three-dimensional (3-D) visualization of the surgical site and improved dexterity. Studies show comparable [3, 89, 115], or superior [99] outcomes of RALP compared with other prostatectomy techniques. The consensus [39] is that while RALP results in lower blood loss, hospitalization duration, and complication rates, it suffers from loss of haptic feedback, longer operating time, and cost [81].

The usage of the da Vinci System is rapidly increasing worldwide, with RALP performed in as many as four out of five radical prostatectomies procedures in the United States [119]. In addition to the advantages above, the RALP platform has been the subject of research and development projects to further improve performance and surgery outcomes. Such tools include real-time ultrasound (US) data [80, 94] that is displayed on the surgeon's console for image guidance and improved visualization of anatomy and cancer (Figure 4.4(a)).

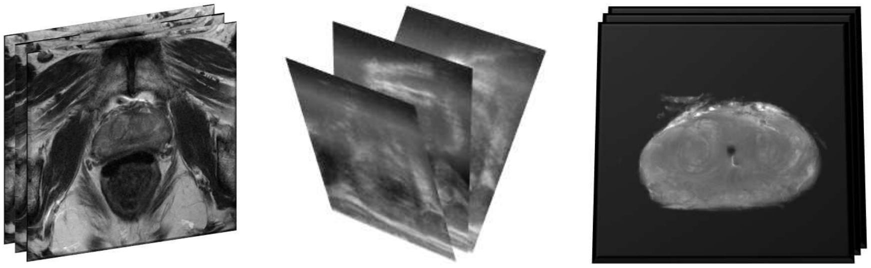

(a) *In vivo* T2w (b) *In vivo* B-mode (c) *Ex vivo* T2w

Figure 1.2: Imaging of the Prostate. Examples of modalities used in our data collection.

1.1.2 Imaging of the Prostate

Noninvasive detection and localization of CaP in medical imaging is an important, yet difficult task. Benefits range from diagnosis of cancer, to preoperative planning and intraoperative carrying out of its treatment. An accurate localization of CaP may lead to less conservative treatments that reduce possible side effects such as impotence and urinary incontinence.

The most common modalities used for imaging of the prostate and CaP are transrectal ultrasound (TRUS) B-mode images and magnetic resonance imaging (MRI) T2w images (Figure 1.2). The advantages of TRUS imaging are mainly that it is widely accessible, simple to operate, fast (real-time), non-ionizing, inexpensive and can be easily used intraoperatively. However, B-mode images present poor quality and are not accurate enough to reliably detect tumors and delineate the prostate [152].

On the other hand, high resolution T2w images (typically acquired with an endorectal coil) provide a very detailed view of the prostate and periprostatic anatomy. Multiparametric MRI presents the most accurate image based characterization of CaP (see [75] and references therein), and can be used for detection, localization and grading of CaP. Yet, magnetic resonance (MR) acquisition is time consuming, resource costly and, in many times, inaccessible, which makes it inapplicable for real-time guidance.[1]

It is therefore a common practice for health care practitioners to employ MR preoperatively for CaP detection and treatment planning, and to employ US intraoperatively for guidance. There are ongoing efforts to integrate preoperative MR data into US-guided procedures for better intraoperative localization of anatomy and cancer (see Chapter 4). Imaging of the postoperative specimens using MRI is also of interest, as these images can be used to further improve CaP characterization by correlating data with confirmed tumors.

---

[1] MR-guidance for prostate biopsy and treatment has been reported, e.g., in [153, 172], but is still cumbersome and not widely used.

1.1.3 Elastography of the Prostate

The characterization of mechanical properties of biological tissues is important in the detection and diagnosis of diseases such as CaP, in which affected tissues typically alter their viscoelastic properties. Manual palpation, e.g., DRE in case of CaP, provides a non-quantitative estimation of such properties that is limited to the surface of the body. Elastography, first introduced in [108], refers to noninvasive techniques for characterizing mechanical properties of tissues.

An elastography system typically comprises an actuator for delivering mechanical excitations to the tissue, an imaging hardware for capturing and computing the resulting displacements, and an algorithm for solving the inverse problem of extracting an elasticity image from the displacements. The elasticity image, also known as elastogram, usually corresponds to the elastic (Young's) modulus of the imaged tissues. Elastography has been shown to aid in CaP detection [118] and interventions [74].

Elastography volumes are typically acquired at the same session along with "regular" imaging with respect to the modality, i.e., US B-mode and MR T2w images. These images can be aligned with their corresponding elastograms using simple or no processing. In vibro-elastography (VE), the radio-frequency (RF) data collection to compute the elastogram, is usually followed by a B-mode scan of the same volume under the same conditions. In magnetic resonance elastography (MRE), the elastogram is computed from the phase component of the acquired signal, while its magnitude is available as low resolution T2w images.

Magnetic Resonance Elastography

Introduced in [100], MRE uses a sinusoidal mechanical excitation and a synchronized MR pulse sequence that encodes the tissue motion in the phase of T2w (akin to) images. The technique have been applied to study tissue changes associated with diseases of, e.g., the liver, breast, prostate, brain, and heart [46]. A detailed description of the acquisition process can be found, e.g., in [150].

In [135], an MRE system with an actively shielded electromagnetic transducer is proposed for *in vivo* prostate imaging (Figure 1.3(a)). Excitations are applied to the perineal region of the subject for efficient transmission of mechanical waves to the prostate. MRE elastograms have been shown to be promising in improving the visibility of the prostate gland. However, to speed up the acquisition process, so as to minimize inconvenience and movements of the patient, the images typically have low resolution. Also, the boundary of the prostate may be blurred and assimilated with the background.

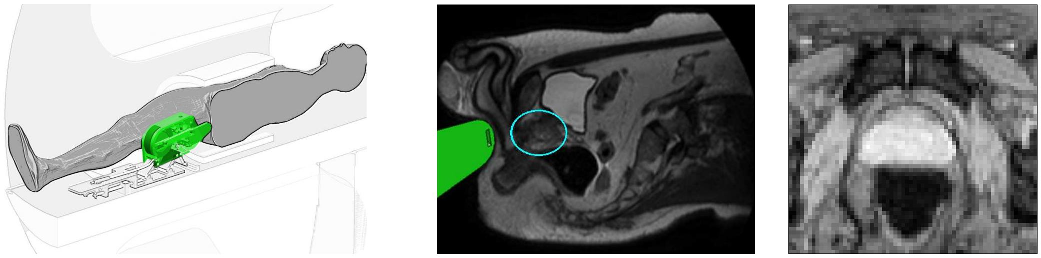

(a) Transperineal MRE setup ([135]) (b) Sagittal T2w (c) MRE magnitude

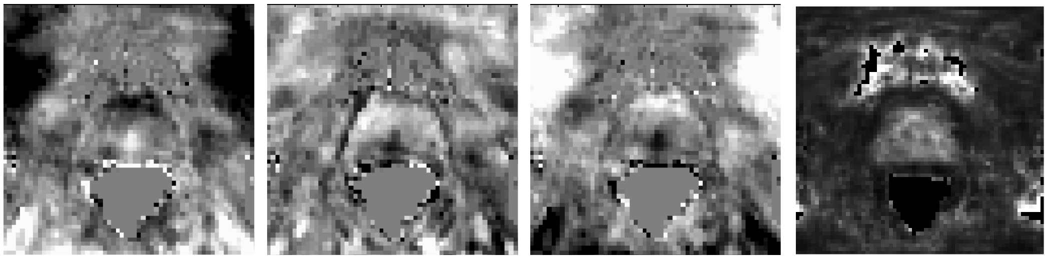

(d) MRE phase 3/8 (e) MRE phase 5/8 (f) MRE phase 7/8 (g) MRE elastogram

Figure 1.3: MRE of the prostate. (a) Illustration of the transperineal driver (green) positioning. (b) The prostate (cyan) overlaid on a sagittal scout image of the patient. (c) A slice of the magnitude image. (d)-(f) Three phases of displacements along the Y-axis, $\pi/2$ apart, depict wave propagation in the tissue. (g) The corresponding slice of the elastogram.

Ultrasound Elastography

In ultrasound elastography (USE), the resulting displacements of the vibrated tissue are recorded using time domain normalized cross-correlation (NCC) between sequences of high frame rate RF data obtained from US imaging. These techniques can be classified into static and dynamic elastography methods. In static elastography, an axial force is applied to the tissue, and the pre- and post-compressed sets of images are used to determine the motion along the direction of the applied force. Dynamic elastography consists of applying vibration to the tissue, during which RF frames are acquired continuously and elastograms are generated in real-time by estimating strain between sequential frames.

The authors in [139] present a TRUS-VE system, in which transfer function analysis of tissue motion over a frequency range of simultaneous vibrations is used to acquire 3-D elastograms of the prostate and periprostatic tissue (Figure 1.4(a)). Compared to B-mode images, with MR T2w as “gold standard,” the produced elastograms have shown, both qualitatively (visually) and quantitatively, to have superior object-background contrast, especially around the base and apex [143]. The authors concluded that the VE imaging

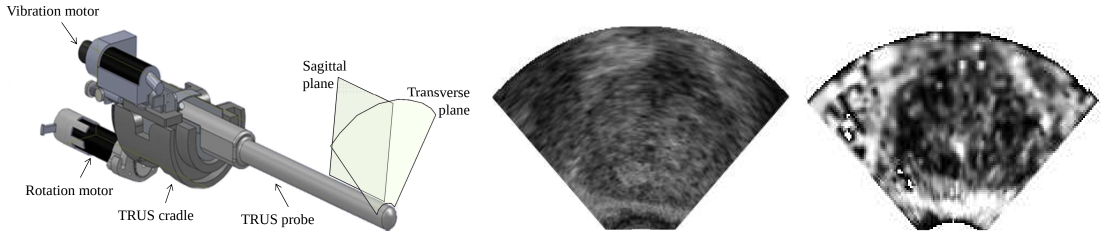

(a) TRUS-VE system ([139]) (b) TRUS B-mode (c) TRUS-VE

Figure 1.4: TRUS-VE of the prostate.

is a promising modality for prostate interventions. However, edge continuity of prostate boundaries in the elastogram was generally inferior to B-mode.

In [9], a USE method using free-hand US is proposed. The technique, referred to as absolute elastography, involves a specific excitation frequency of the tissue, and tracking its motion using the algorithms proposed in [9, 37]. Assuming linearity, the motion has the same temporal frequency, and the phase and amplitude of the displacement at each pixel can be estimated similar to MRE. The inverse problem is then solved, e.g., by local frequency estimation (LFE), to reconstruct the elastogram.

1.1.4 Whole-Mount Histopathology of the Prostate

Whole-mount histopathology refers to placing an entire organism or structure directly onto a microscope slide in order to study the manifestations of disease by a pathologist. When specimen size allows and longer processing time is available, whole-mount histopathology preserves the structural relationships between cells, and facilitates the comparison of the specimen to imaging data. In whole-mount histopathology of the prostate, analysis of complete transversal cross-sections, placed on histological slices, help in predicting the long term disease outcome of the CaP patients, and provide a ground truth to determine the ability of imaging to detect cancer.

The process required for pathologists to prepare scans of whole-mount histological slices in our study is summarized as follows (see also Figure 2.1). The specimen should first be fixed in 10% formalin solution for about 72 hours, followed by its transverse sectioning into 4 mm thick parallel sections using a single blade or a multi-bladed cutting device [32]. Each section is embedded in a paraffin block, followed by slicing a thin, 4 μm, layer from each block using a microtome. Each slice is then glided onto a glass slide, followed by its staining in hematoxylin and eosin (H&E). Finally, the stained slides are digitally scanned to generate a series of digital images that represent the different levels of the specimen.

1.1.5 Prostate Registration

Registration is the process of establishing a spatial correspondence between two or more image data sets. The images may be acquired at different times, from different perspectives or by different imaging techniques. In medical image processing, registration is a critical task for integration of information acquired from pre-, intra-, and postoperative imaging. In CaP diagnosis and treatment, registration can, for example, enable US-guided procedures to benefit from the accuracy of cancer detection and anatomical detail in MR.

In general, given a reference image and a (set of) template image, the registration problem is to find a geometric transformation or mapping, such that the transformed (deformed) template is close to the reference, in some sense. A detailed classification of the numerous registration methods in medical imaging is provided in [84]. The main classification criteria relevant to the algorithms discussed in this thesis are the dimensionality of the registration, the nature of transformation the registration is confined to, and the nature of the registration basis.

The spatial dimensionality we consider is registration of a set of two-dimensional (2-D) images to a 3-D volume (Chapter 2), and registration of a 3-D volume to a 3-D volume (Chapters 3-5). The nature of the spatial transformations we propose is rigid, i.e., translation and rotation, with an additional isotropic or anisotropic scaling (Chapters 2-4), and deformable (also known as curved or nonrigid) transformations (Chapters 3-5).

In terms of the registration basis, the focus is on intrinsic registration methods of intensity-based (Chapters 2, 4-5), model-based (Chapters 2-3), and segmentation-based (Chapters 2, 4) nature. Intensity-based methods utilize solely image intensities to compute the mapping. In model-based methods, a template model of the target structure is extracted (preoperatively, usually) and registered to the reference image. Segmentation-based methods register a segmented template into a segmented reference.

The registration problem is often formulated as an optimization of a similarity metric between the deformed template and the reference images, with respect to a set of parameters (parametric techniques), or to the mapping displacements directly (nonparametric techniques) [154]. In the former case, in order to correct for the problem's ill-posedness and produce more probable maps, the transformation is confined to a function space and the parameters to be optimized are the weights of the basis functions. In the latter case, a regularization metric is defined and combined with the similarity metric in order to smooth the displacements. Registration algorithms differ in the choice of the similarity metric, parameters or regularization metric, and in the numerical method for solving the optimization problem.

Common choices for the similarity measure are the sum of squared differences (SSD), and NCC. While simple and, in many cases, provide plausible results, these methods are sensitive to noise and require the reference and template to be of the same intensity scale. Therefore, these measures are not suitable for multi-modality registration. An extensively used similarity measure, that is applicable to multi-modality registration, is the (normalized) mutual information (MI) [26, 165].

Many parametric registration techniques employ geometric transformations derived from interpolation theory, such as polynomial or B-spline function spaces. In nonparametric techniques, a variety of metrics have been proposed to regularize the deformations of the template according to geometrical transformations derived from physical models. A popular physical regularizer, which we also employ in this thesis (Chapters 3-5), is the elastic potential of the displacements [11, 20]. Other physical metrics are based on diffusion [58], fluid [25] and curvature [41] models. Another metric, the earth mover's distance, preserves the "mass" associated with the images, and yields the optimal mass transport [52].

An extensive survey of deformable medical image registration methods is presented in [154]. A general framework for many of these techniques is presented in [92]. The framework is based on a variational formulation and the corresponding Euler-Lagrange equations that characterize a minimizer. Numerical schemes to solve the resulting partial differential equations (PDEs) can be formulated and discretized using the finite difference method. Other schemes employ the finite element method (FEM) [176].

Biomechanical models for registration are segmentation-based methods, in which the reference and/or template segmented models are associated with mechanical properties, e.g., elasticity, viscosity. The template model can then be deformed in a physical manner, in order for it to match the reference model, by applying forces. Typically, FEM is employed to numerically model the deformation.

In [38], a linear elastic biomechanical model is proposed for registration of MR brain images. The method was adapted in [16] for registration of the prostate. In [157], the authors propose a global surface difference to register linear elastic models extracted from prostate TRUS and MR images. A nonlinear elastic model that is driven by a distance field representation of the models, was used for fast registration of prostate data in [106].

Biomechanical models produce plausible and physical deformations. However, accuracy of the registration highly depends on accuracy of the segmentation to extract the models. An intensity-based registration of the prostate in TRUS, that does not require segmentation, was presented in [13] for biopsy tracking. The technique involves a generalized correlation ratio as a similarity metric, with elastic regularization and an inverse consistency constraint.

1.2 Thesis Objectives

The objectives of this thesis are as follows:

- Developing and validating methods for registration between histopathology slices and volumetric imaging of the prostate that allow both training and evaluation of CaP classifiers.

- Developing and validating methods for registration between preoperative MRI and intraoperative TRUS during RALP, in order to facilitate surgery and minimize side effects while avoiding positive margins.

- Incorporating elastography information into the registration framework, and investigating its effect on registration performance.

- Improving the quality and/or shortening acquisition time of MRE.

1.3 Thesis Outline

The overall goal of the research undertaken in this thesis is to develop algorithms for registration of the prostate among different modalities. The motivation for this research is to provide tools that allow for an automatic preoperative and intraoperative localization of CaP. In addition, the thesis studies the reciprocity between registration and elastography.

The diagram in Figure 1.5 depicts the general structure and flow of the thesis. We begin with a "pure" registration algorithm, proceed to incorporation of elastography in registration that can be applied to detection of CaP and its treatment, then we incorporate image registration to enhance MRE reconstruction, and end with a general scheme to improve MRE acquisition.

This chapter introduced the research topic, motivation for performing this research and the thesis objectives. The remainder of this thesis is organized as follows. In Chapter 2, we consider a multi-slice to volume registration method in which a stack of sparse, unaligned 2-D whole-mount histological slices is registered to a 3-D volumetric imaging of the prostate. A particle filtering framework is proposed in order to derive optimal registration parameters in a Bayesian approach. We demonstrate and evaluate our method on a diverse set of data that includes a synthetic volume, *ex vivo* and *in vivo* MRI, and *in vivo* US.

In Chapter 3, we propose a novel registration method that uses a patient-specific biomechanical model acquired using MRE to deform the *in vivo* volume and match it to the surface

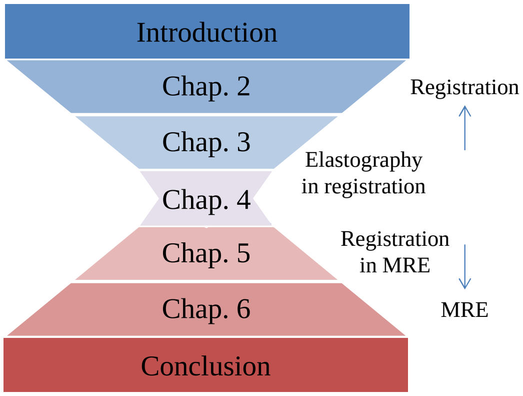

Figure 1.5: Thesis outline.

of the *ex vivo* specimen. The incorporation of elastography data into the registration framework allows the measured inhomogeneous elasticity to be assigned to the *in vivo* volume. The method is demonstrated and evaluated on simulation and clinical cases.

In Chapter 4, we propose a segmentation-based registration method between preoperative MRI and intraoperative TRUS. The resulting corresponding images may be displayed on the surgeon's console during RALP. Incorporation of elastography is proposed as an inter-modality to facilitate MRI-TRUS alignment, by elasticity-based registration of the corresponding MRE and USE.

In Chapter 5, we employ registration and image processing techniques to improve MRE reconstruction. Registration is used to compensate for patient's motion during acquisition, while super-resolution technique is used to enhance the resolution of the acquired images.

In Chapter 6, we present an optimization-based approach for encoding motion in MRE. Multidirectional sequences are derived by setting the problem in an experimental design framework. Such designs are implemented and evaluated on simulation and phantom data. Finally, in Chapter 7, we summarize the major contribution of this thesis and describe potential research directions in the future.

Chapter 2

Registration of Whole-Mount Histology and Volumetric Imaging of the Prostate

2.1 Introduction

In order to characterize cancer and to evaluate its localization in volumetric images, such as those obtained by an US or MR imaging, the images must be compared to the “gold standard” provided by a histopathological analysis of the excised tissue following biopsy or prostatectomy. Thus, registration of histology to the imaging is required so as to find their spatial correspondence.

The overall objective of the work described in this chapter is to develop and validate a method for automatic registration between 2-D digital scans of whole-mount histological slices and 3-D volumes of the prostate. Such multi-slice to volume registration is challenging due to the dissimilarity between the modalities’ intensity values, the similarity in geometry of different cross-sections of the volume, the sparsity of the histological slices and the inaccuracies that occur during their preparation.

Each step in the preparation process of whole-mount histopathology, as described in Section 1.1.4 above, introduces uncertainty to the geometric origin of the histological slices in the volumetric images. We distinguish between the different mechanisms for misalignments:

- In-plane misalignment – gliding the slice and scanning the slide are prone to 2-D rotation and translation of the histology image. These misalignments are statistically independent among slices, but distributed around the correct pose, since efforts are made to align the slices visually during preparation.

- Out-of-plane misalignment – sectioning and slicing are susceptible to 3-D rotation and translation of the specimen with respect to the imaging volume. These misalignments may be caused directly by errors in position and angulation of the blade during sectioning, and/or indirectly by elastic deformation of the specimen such as bending.

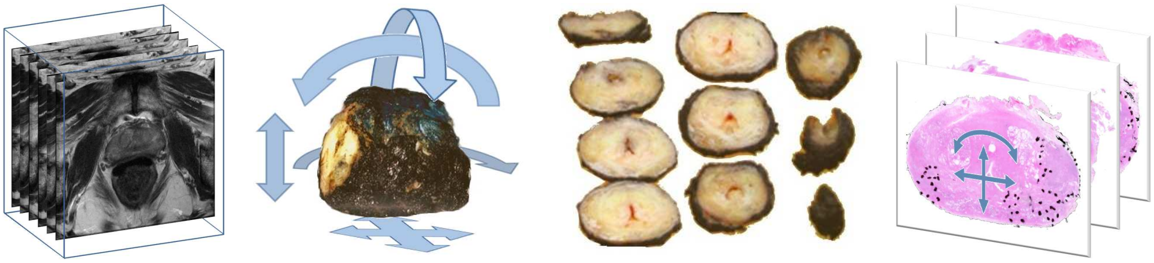

(a) MR volume (b) Prostate specimen (c) Prostate sections (d) Histological slices

Figure 2.1: Problem illustration. (a) Volumetric imaging of the prostate, such as an *in vivo* MR, is being acquired. (b) The excised fixed prostate is sectioned, during which out-of-plane misalignments occur. (c) Each 4 mm section is embedded in a paraffin block, from which a 4 μm thin layer is sliced. (d) Each slice is glided onto a slide, stained and scanned, during which in-plane misalignments occur. These scans should be then registered to the volumetric imaging.

While each slice may have a different pose, they are typically correlated, especially when using a multi-bladed device, as described later, that maintains orientation and spacing between the sections.

- Scaling – fixation of the specimen causes change in its volume. The scaling is anisotropic and typically manifested as shrinkage due to tissue dehydration [145]. In addition, implicit scaling can be caused by errors in measuring histology resolution, which is often done manually. Scaling is highly correlated among the slices.
- Residual deformation – the shape of the prostate may be deformed after imaging.

An algorithm for registration of histological slices to a volumetric image should take these mechanisms into account. Overall, excluding deformation, the number of degrees of freedom in registration of N histological slices to a volume is $9N$, where typically $N \sim 10$. In addition, the transformation space is constrained, e.g., such that slices do not intersect. Figure 2.1 illustrates the registration problem.

Previously, different apparatuses were proposed to minimize misalignment between histological slices. In [12], the authors have inserted needles into the specimen before sectioning to provide landmarks for correcting in-plane misalignment. In [32], a multi-bladed cutting device that constrains the specimen mechanically during sectioning allows its slicing into parallel cuts of fixed intervals, thus minimizing out-of-plane misalignment between slices. However, in both approaches, the sectioning axis might not coincide with the scanning axis of the imaging and further registration is needed.

The authors in [129] proposed a rotating platform for imaging a desired plane in *ex vivo* MR, and then cut the specimen in parallel to that plane. The works [167, 168] involve placement of fiducial markers into the *ex vivo* specimen, in order to guide its sectioning along the imaging plane with a magnetically tracked probe, while [45] employs such markers to fit affine transformations between histological slices and the specimen. These methods achieve good registration results, but require a special setup, and additional clinical time and approvals that may not be available in practice.

For registration of *in vivo* imaging, the authors in [148, 162] employ a 3-D printer to generate a patient-specific prostate mold, in which the fixed specimen is placed and cut in order to preserve its orientation. However, the postoperative specimen after fixation might not fit into the mold that is based on preoperative *in vivo* imaging. In [60], the authors propose an apparatus for insertion of three needles from apex to base at distinct angles into fresh prostate specimens. The resulting punctures serve as fiducial markers, based on which the slices are aligned to each other. This alignment method is intended to allow a 3-D registration to *in vivo* imaging. Although requiring a special setup, as well as invasive manipulation of the specimen, the authors report that their protocol is employed in a rapid and standardized manner, which does not compromise the histopathology information.

A 3-D deformable registration between histology and *ex vivo* MR of the prostate was proposed in [175]. The method involves extraction of landmarks on, and inside the surface of the gland. However, in order to acquire landmarks on the histological surface, the sectioning should be dense, which may not be feasible in practice. The authors in [24] propose to register segmented histology with segmented multi-parametric *in vivo* MR. A corresponding MR slice is chosen for each histological slice by an expert, followed by a 2-D to 2-D registration. Such manual search for corresponding slices may be a difficult and/or time consuming task for an expert.

In [111], a 3-D histological volume is reconstructed from aligned slices, and a 3-D to 3-D registration method is employed to match it to the imaging volume. However, as discussed in [24], a volume reconstruction from the sparsely sectioned histology is inaccurate and may lead to registration errors. Thus, the authors in [171] consider a more practical registration between multiple histology slices and an *in vivo* MR volume. They propose an iterative algorithm that consists of three modules: finding a subset of MR slices that corresponds to the histological slices, 2-D registration of each histological slice to its corresponding MR slice, and 3-D registration of the MR volume to the registered histological slices.

In summary, the approaches proposed in the literature typically require special hardware [32, 129], involve insertion of markers to the specimen [12, 45, 60, 167, 168], are 2-D in nature [24] or assume a dense sectioning for a 3-D registration [111], do not take into account all degrees of freedom and/or do not utilize their interdependence, are sensitive to segmentation errors, and/or are prone to local extrema [171]. While fusing several methods and running them multiple times with different initializations may allow for an accurate registration, it would result in a cumbersome and long process that might not be suitable in some scenarios.

Some works in the literature, e.g., [7, 43, 73, 82, 88, 93, 105, 117, 141], have applied filtering techniques to image registration. This approach allows derivation of an optimal estimation of the registration parameters in a Bayesian fashion to overcome issues such as susceptibility to initialization and local extrema. Specifically, particle filtering was employed for rigid/affine registration of points-to-surface [82] and two point clouds [43, 141] using a point-based metric, a model-to-slice registration using a region-based metric [105], an elastic/affine registration of two images using an intensity-based metric [7, 88], and optimization of a parameterized deformable registration field [73].

We propose a unified approach for registration of multiple slices to a volume in 3-D without intervening with the standard histopathological processing. The method employs particle filtering that allows derivation of an optimal estimation of the registration parameters in a Bayesian fashion to overcome issues such as susceptibility to initialization and local extrema. The framework allows incorporation of prior knowledge on admissible misalignments according to the misalignment mechanisms discussed above, and knowledge of the imaging noise or segmentation error.

A particle in our method represents a combination of the slices in various 3-D poses. Each such particle is assigned a likelihood based on the similarity of its slices to the volume, and a prior probability based on the admissibility of their pose misalignment. This allows to implicitly neglect non-admissible pose of slices, associated with lower probabilities, and diffuse the rest towards an optimal estimation of the true pose. This approach contends well with the multimodal nature of the optimization, and, as the number of particles increases, converges to the global optimum.

Our approach generalizes the method in [171], in the sense that the histological slices are not assumed to be parallel to each other, and the volumetric image does not need to be segmented if it contains sufficient intensity information. As in [171], we do not handle deformations of the histological slices to avoid over fitting the sparse data. However, the affine model we consider provides a first order approximation of the deformations, and a deformable registration algorithm may be employed as postprocessing to compensate for the residual deformation. We evaluate the method on a diverse set of data that includes a synthetic volume, *ex vivo* MR, *in vivo* MR, and *in vivo* US.

The remainder of this chapter is organized as follows. In Section 2.2, we formulate the multi-slice to volume registration problem. In Section 2.3, we model the problem in state-space, and present the particle filtering algorithm for registration. In Section 2.4, we provide details on implementation and the clinical experiments conducted to evaluate the proposed method, and summarize the results. Finally, we conclude in Section 2.5 with a summary and future research directions.

2.2 Problem Formulation

2.2.1 Slice Transformation and Volume Re-Slicing

Let $\bar{r} = (x, y, z)^T \in \mathbb{R}^3$ be the 3-D spatial coordinates vector. A rigid transformation of $\bar{r}$ can be parameterized by six pose parameters, namely, three translation values Δ_i along each axis $i = x, y, z$, and three rotation angles θ_i about each axis. In addition, anisotropic scaling is parameterized by three scaling factors ξ_i of each axis. We denote the pose vector as $\bar{s} = (\{\Delta_i\}, \{\theta_i\}, \{\xi_i\})^T$, $i = x, y, z$.

We represent the spatial transformation by a concatenation of matrices using homogeneous coordinates, such that the transformed coordinates vector $\tilde{\bar{r}} \in \mathbb{R}^3$ is written as

$$\begin{pmatrix} \tilde{\bar{r}} \\ 1 \end{pmatrix} = T(\bar{s}) \begin{pmatrix} \bar{r} \\ 1 \end{pmatrix},$$

where

$$\begin{aligned} T(\bar{s}) &= T_{\text{out-of-plane}}(\Delta_z, \xi_z, \theta_x, \theta_y) T_{\text{in-plane}}(\Delta_x, \Delta_y, \xi_x, \xi_y, \theta_z) \\ &= T_{\theta_y} T_{\theta_x} T_{\xi_z} T_{\Delta_z} T_{\theta_z} T_{\xi_y} T_{\xi_x} T_{\Delta_y} T_{\Delta_x}. \end{aligned} \tag{2.1}$$

The matrix $T \in \mathbb{R}^{4\times4}$ is the affine transformation matrix with respect to the pose vector. Explicit expressions of the matrices can be found, e.g., in [53]. The specific order of the matrix multiplication in (2.1) was set to distinguish between "in-plane" and "out-of-plane" transformations, such that the former will act prior to the latter, so as to model the misalignment mechanisms described in Section 2.1. This order also guarantees that slices sharing a same out-of-plane pose are parallel, even though their in-plane pose may vary. For notation purposes we will omit the "1" and simply write $\tilde{\bar{r}} = T(\bar{s})\bar{r}$.

Let $\{\bar{r}_0 = (x, y, z_0)^T : (x, y) \in \mathbb{R}^2\}$ define a planar region or slice on $z = z_0$. We may apply an affine transformation with respect to a pose $\bar{s}_0$ to each point on the slice, such that $\{\tilde{\bar{r}}_0 = T(\bar{s}_0)\bar{r}_0\}$ is the shifted, rotated and scaled slice.

Suppose we are given a volumetric image, $J : \mathbb{R}^3 \to \mathbb{R}$. In order to find the values of the image on the transformed slice, we can use Euler coordinates as the interpolation reference frame and write

$$\tilde{J}_0(x, y; \bar{s}_0) = J(T(\bar{s}_0)\bar{r}_0), \quad \forall (x, y) \in \mathbb{R}^2. \tag{2.2}$$

We refer to this operation as re-slicing of the volume J, and to $\tilde{J}_0$ as the re-sliced image.

2.2.2 Multi-Slice to Volume Registration

Assume we are given N scans of 2-D histological slices with the approximated spacing between consecutive pairs. In addition, assume that the region inside the specimen in each slice is segmented. We can represent this information as the set of triplets $\{I_n, H_n, z_n\}_{n=0}^{N-1}$, where $I_n \colon \mathbb{R}^2 \to \mathbb{R}$ is a grayscale image of the slice, $H_n \colon \mathbb{R}^2 \to \{0, 1\}$ is a binary image with values of "1" on the region inside the specimen, and $z_n \in \mathbb{R}$ is the position or "height" of the slice in 3-D space. Without loss of generality, we set $z_0 = 0$ and assign values for $\{z_n\}_{n=1}^{N-1}$ with respect to the given spacing.

Let J be a volumetric image of the same specimen the histology was processed from. We denote the 3-D pose vector of the nth slice as $\bar{s}_n$. The registration of histology to volumetric imaging problem is finding N poses $\bar{s}_{0:N-1} = \{\bar{s}_n\}_{n=0}^{N-1}$, such that the transformed segmented histological slices optimally match, in some sense, the corresponding re-sliced images of the volume. The admissible space of 3-D poses is constrained such that the transformed slices do not intersect.

In general, the multi-slice to volume registration can be formulated as the optimization problem

$$\min_{\substack{\bar{s}_{0:N-1} \\ \text{(admissible)}}} \sum_{n=0}^{N-1} \alpha_n D[I_n(\cdot), J(\cdot); H_n(\cdot), \bar{s}_n], \tag{2.3}$$

where $D[I_n(\cdot), J(\cdot); H_n(\cdot), \bar{s}_n]$ is a distance functional that measures (dis-)similarity between the slice I_n and the volumetric image J, with respect to the slice segmentation H_n and its pose $\bar{s}_n$. The weights $\{\alpha_n\}_{n=0}^{N-1}$ can be used to prioritize or neglect certain slices, as discussed in Section 2.4.3 below.

The formulation (2.3) supports any choice of metric for measuring similarity. We consider three types of metrics, as discussed in Section 2.3.5. Specifically, we employ an intensity-based metric for the *ex vivo* MR data sets, a region-based metric for the *in vivo* MR, and a point-based metric for US data sets (in which we assume that the volumetric image J is segmented as well).

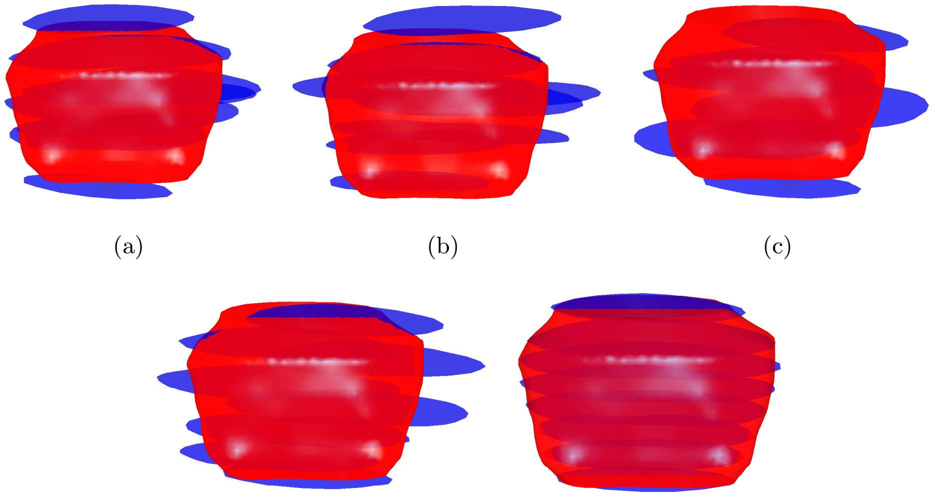

(a) (b) (c)

(d) (e)

Figure 2.2: Random particles. Each particle represents a combination of 3-D poses assigned to the histological slices (in blue). The surface of the prostate in the volumetric image is shown (in red) as reference. Some particles are more likely to be correct than others. Particle (e) corresponds to the MAP estimation.

2.3 Particle Filtering

Introduced in [47], particle filters (PFs) are sequential Monte Carlo methods based on point mass (or "particle") representations of probability density functions (pdfs). As the number of particles becomes larger, this representation becomes closer to the usual functional description of pdf, and the PF approaches the optimal Bayesian estimate. Unlike the traditional Kalman filter and its extensions, PFs are capable in handling nonlinear state-space models with non-Gaussian noise. The tradeoff is that PFs are computationally expensive, although, with the increase in computational power in recent years, PFs were successfully employed even in real-time applications.

In order to set the registration problem in a filtering framework, we represent it as a state-space model. We define the state vector as $\bar{S} = \bar{s}_{0:N-1}$, i.e., a column vector comprising the $9N$ pose and scaling parameters of all slices. In this formulation, a point in state-space, or a particle, represents a combination of slices in various 3-D poses. Figure 2.2 shows examples of different particles that were generated for one case.

2.3.1 Prediction Model

Since our problem is static, we assume a process in which the state $\bar{S}^{(k)}$ at a time step (a filtering iteration) $k \geq 1$, can be predicted from the previous state $\bar{S}^{(k-1)}$ simply by

$$\bar{S}^{(k)} = \bar{S}^{(k-1)} + \sqrt{\gamma^{k-1}} U^{(k)}, \tag{2.4}$$

where U is an identically and independently distributed (i.i.d.) system noise that reflects the uncertainty in the pose parameters, and $0 < \gamma \leq 1$ is a discount factor that reflects the decrease of this uncertainty with every time step.

In order to model the statistical dependency of the pose parameters among the slices, we define U to have a multivariate normal distribution with a specific form of covariance. We write $\bar{s}_{i,0:N-1}$ to denote a vector that comprises N values of the pose parameter $\cdot_i$ of all slices, e.g., $(\theta_{x,0}, \ldots, \theta_{x,N-1})^T$. We assume that $\bar{s}_{i,0:N-1}$ is normally distributed around a zero mean with the $N \times N$ covariance matrix

$$\Sigma_{\bar{s}_i}(\sigma_{\bar{s}_i}, \eta_{\bar{s}_i}) = \begin{pmatrix} \sigma^2_{\bar{s}_i} & \sigma^2_{\bar{s}_i} - \frac{\eta^2_{\bar{s}_i}}{2} & \cdots & \sigma^2_{\bar{s}_i} - \frac{\eta^2_{\bar{s}_i}}{2} \\ \sigma^2_{\bar{s}_i} - \frac{\eta^2_{\bar{s}_i}}{2} & \sigma^2_{\bar{s}_i} & \cdots & \vdots \\ \vdots & \vdots & \ddots & \vdots \\ \sigma^2_{\bar{s}_i} - \frac{\eta^2_{\bar{s}_i}}{2} & \cdots & \cdots & \sigma^2_{\bar{s}_i} \end{pmatrix},$$

where $\sigma^2_{\bar{s}_i}$ is the variance of the pose parameter, and $0 < \eta^2_{\bar{s}_i} \leq 3\sigma^2_{\bar{s}_i}$ is the variance of the difference of this parameter between each pair of slices, i.e., $\eta^2_{\bar{s}_i} = \mathrm{Var}(\bar{s}_{i,n_1} - \bar{s}_{i,n_2})$, $\forall n_1 \neq n_2$.

The smaller the value of $\eta^2_{\bar{s}_i}$ is, the more (positively) correlated the slices become, with $\eta^2_{\bar{s}_i} \to 0$ yielding the same parameter value for all the slices (as if the value was drawn from a univariate normal distribution with a variance $\sigma^2_{\bar{s}_i}$). Specifically, setting $\eta^2_{\theta_x}, \eta^2_{\theta_y} \to 0$ yields transformed slices that are parallel, and $\eta^2_{\Delta_z} \to 0$ yields equally spaced slices. Setting $\eta^2_{\bar{s}_i} = 2\sigma^2_{\bar{s}_i}$ yields a diagonal covariance matrix, thus an independent parameter for each slice (with a variance $\sigma^2_{\bar{s}_i}$).

According to the discussion on the misalignment mechanisms for each type of pose parameter in Section 2.1, low values of $\eta^2_{\bar{s}_i}$ (high correlation among slices) are typically assigned to the out-of-plane pose and scaling parameters, and a value of $\eta^2_{\bar{s}_i} = 2\sigma^2_{\bar{s}_i}$ (no correlation among slices) is assigned to the in-plane pose parameters.

The system noise is therefore defined as $U \sim \mathcal{N}(0, \Sigma_U)$, where Σ_U is a $9N \times 9N$ covariance matrix that comprises the nine covariance matrices $\Sigma_{\bar{s}_i}$, one for each pose parameter, in its diagonal. The system (prediction) model (2.4), with the modeled noise U, can be employed to formulate the prior pdf, i.e., the probability of the current state given the previous state vector, as

$$p(\bar{S}^{(k)}|\bar{S}^{(k-1)}) \propto \exp\left\{-\frac{1}{2}\left(\bar{S}^{(k)} - \bar{S}^{(k-1)}\right)^T \frac{1}{\gamma^{k-1}}\Sigma_U^{-1}\left(\bar{S}^{(k)} - \bar{S}^{(k-1)}\right)\right\}. \tag{2.5}$$

2.3.2 Observation Model

In a state-space model, at each time $k \geq 1$, a measurement (observation) becomes available and is related to the state vector via the observation model. In case the intensity- or region-based metrics are being used, we consider that observation to be the static volumetric image J with an additive i.i.d. measurement noise V that represents the intensity noise of the image. In the point-based metric, the points of the segmented surface are the observation, and the measurement noise represents the errors in segmentation and reconstruction of the surface. In both cases, the noise is modeled as $V \sim \mathcal{N}\left(0, \sigma_v^2\right)$, i.e., a zero mean Gaussian noise with a variance σ_v^2.

The relation between the observation and the state vector is a nonlinear, complex and unknown function. We can define the observation model implicitly by defining the likelihood pdf, i.e., the probability of the observation given the state vector, as

$$p(J|\bar{S}^{(k)}) \propto \exp\left\{-\sum_{n=0}^{N-1} \alpha_n D[I_n(\cdot), J(\cdot); H_n(\cdot), \bar{s}_n^{(k)}]/\sigma_v^2\right\}. \tag{2.6}$$

Note that if the state $\bar{S}^{(k)}$ provides a good alignment between the histological slices I_n and the volume J, the functional D takes small values which results in high likelihood. In turn, high likelihood states minimize the objective functional (2.3). Such interpretation of a metric or an energy functional as log-likelihood has been used, e.g., as in [21], for switching between variational and probabilistic formulation of optimization problems.

2.3.3 Initial State

In order to get an initial estimate of the state vector, we try to explicitly minimize the objective functional (2.3). Of course, due to the multimodal nature of the problem, the process is most likely to converge to a local minimum. Nevertheless, this local minimum typically provides an initialization to the particle filtering algorithm that allows a faster convergence to the global minimum.

Moreover, in order to simplify the minimization, we reduce the search space in this step by "locking" the pose parameters of all the slices, i.e. $\bar{s}_{n_1} = \bar{s}_{n_2},\ \forall n_1, n_2$. Thus, the slices in this step move together in 3-D as a "sparse" volume. This minimization process brings the slices into the coordinate system of the volume in order to correct for global misalignment. It may also be seen as analogous to the volume alignment step in [171], where the entire volume is transformed to maximize similarity with the histological slices on their pre-defined planes.

We minimize (2.3) with respect to the "locked" pose vector $\bar{s}$ until it converges, such that the difference between the pose parameters of two consecutive iterations is less than some threshold. Section 2.4.3 below provides additional details on the implementation and optimization methods. We then apply the pose vector $\bar{s}$ to all slices, and denote the resulting state vector as $\bar{\bar{S}}^{(0)}$. With no better estimate about the pose, we define the initial state pdf as a deterministic probability distribution about the resulting state. We denote this pdf as $p(\bar{S}^{(0)}) = \delta(\bar{S}^{(0)} - \bar{\bar{S}}^{(0)})$, where δ is the Dirac delta function.

2.3.4 Particle Filtering Algorithm

The filtering problem is to recursively construct the posterior pdf of the state given the observation, i.e., $p(\bar{S}^{(k)}|J)$. A PF algorithm produces at each time step k, a cloud of M states $\{\bar{S}^{m,(k)}\}_{m=1}^{M}$, known as particles, that provides a discrete weighted approximation of the posterior distribution.

Several particle filtering schemes have been proposed in the past, but can be shown to be derived from a generic algorithm [8]. For a comprehensive discussion on PFs, we refer the reader to [30, 31] and references therein. In this chapter we employ a sampling-importance-resampling filter. The algorithm, described below, is summarized as a pseudocode in Algorithm 2.1.

The algorithm starts with sampling M times from the initial state distribution $p(\bar{S}^{(0)})$, and then employing the Bayes' recursion at each time step. Assuming that one can sample from the posterior, an empirical estimate of this distribution is given by

$$p(\bar{S}^{(k)}|J) \approx \sum_{m=1}^{M} \omega^{m,(k)} \delta(\bar{S}^{(k)} - \bar{S}^{m,(k)}), \tag{2.7}$$

where $\omega^{m,(k)}$ is a weight associated with the mth particle, such that $\sum_{m=1}^{M} \omega^{m,(k)} = 1$. In general, it is difficult to sample from the posterior. One solution is to employ importance sampling, which consists of using a distribution known as *the proposal* that is related to the posterior but easier to generate samples from, and then normalizing the weights.

We follow an approach proposed in [125] for tracking. In this approach, predicted particles $\{\hat{\bar{S}}^{m,(k)}\}_{m=1}^{M}$ are first sampled from the prior distribution, and then propagated towards higher likelihood states based on observations via an update stage, which can be interpreted as an importance sampling of the particles $\{\bar{S}^{m,(k)}\}_{m=1}^{M}$. The weights are recursively updated by

$$\omega^{m,(k)} \propto \omega^{m,(k-1)}\, p(J|\bar{S}^{m,(k)})\, p(\bar{S}^{m,(k)}|\bar{S}^{m,(k-1)}). \tag{2.8}$$

After executing the alignment process in Section 2.3.3 above, we generate M particles according to $p(\bar{S}^{(0)})$, i.e., M state vectors that equal to the initial state. We set the particles' weights $\{\omega^{m,(0)}\}_{m=1}^{M}$ uniformly to $\frac{1}{M}$ and proceed to time step $k = 1$. Then, and at every new time step, we predict a state $\{\hat{\bar{S}}^{m,(k)}\}_{m=1}^{M}$ for each particle m, according to the system model (2.4).

The predicted state of each particle is propagated towards higher likelihood states, as defined by (2.6), based on the "observed" volume J. We do this by minimizing the objective functional for each particle, with its predicted state $\hat{\bar{S}}^{m,(k)}$ taken as the initial state. This update stage is denoted as

$$\bar{S}^{m,(k)} = F_{\min}^{L}(\hat{\bar{S}}^{m,(k)}), \tag{2.9}$$

where $F_{\min}^{L}$ stands for performing L iterations of the optimization process in order to minimize (2.3) with respect to the entire ("unlocked") state of the particle $\bar{s}_{0:N-1}^{m,(k)}$.

Only a fixed number of L iterations is performed in order to avoid overfitting the state of each particle to the observation. Large values of L lead to convergence of the slices to the volume, and thus express trust in the observations, while small values of L keep the slices close to their predicted state, and thus express high trust in the initial alignment and system model. Too large values of L would result in slices reaching unfeasible states that maximize their similarity to the volume, perhaps even violating the non-intersecting slices constraint, and causing degeneration of particle diversity. On the other hand, too small values would result in the particles staggering around the initial alignment state, keeping them in low likelihood states.

After all particles are updated, we assign an importance weight to each one, based on (2.8). To this end, we calculate the prior and likelihood for each particle $\bar{S}^{m,(k)}$ using (2.5) and (2.6), respectively. The posterior pdf of the state given past and current observations is then approximated by $p(\bar{S}^{(k)}|J) \approx \sum_{m=1}^{M} \omega^{m,(k)} \delta(\bar{S}^{(k)} - \bar{S}^{m,(k)})$. The posterior allows an optimal estimate of the state to be obtained, with respect to any criterion. In our experiments, we used the maximum *a posteriori* (MAP) state, which corresponds to the

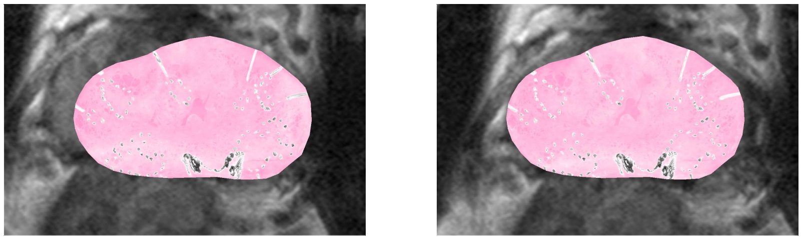

(a) intensity-, region-based: Initial (b) intensity-, region-based: Final

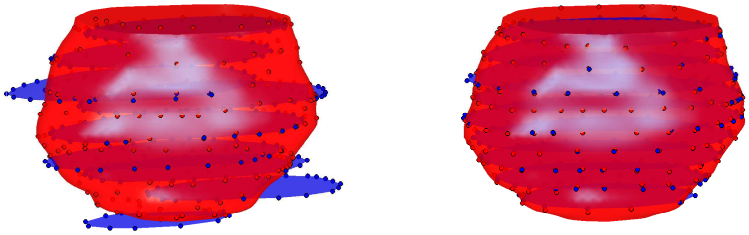

(c) point-based: Initial (d) point-based: Final

Figure 2.3: Minimization of the similarity metrics. (a)-(b) The segmented region of a histological slice is overlaid on the cross-section of the volumetric MR image on the re-slicing plane. In the intensity-based case, the re-slicing planes move in order to maximize the MI metric between the cross-sections of the image and the corresponding histological slices. In the region-based case, the re-slicing planes move in order to minimize the intensity variances of the image's cross-sections inside and outside the segmentation contour of the corresponding histological slices. (c)-(d) The segmented histological contours (filled in blue) are interwoven with the surface (in red) that was segmented from an US volume. The points represent the closest counterparts of the contour points on the surface. The minimization process moves each slice to minimize the distance between the pairs of closest points.

state of the highest weighted particle, i.e.,

$$\bar{S}^{\mathrm{MAP},(k)} = \bar{S}^{m^\star,(k)}, \quad \text{with} \quad m^\star = \arg\max_{1\leq m\leq M} \omega^{m,(k)}. \tag{2.10}$$

Finally, resampling is performed. We resample M times according to the approximated posterior distribution above, to have new particles $\{\bar{S}^{m,(k)}\}_{m=1}^{M}$ that replace the current ones. This step eliminates particles that have very low weights and concentrates on higher weighted particles. The importance weights for the resampled particles are reset to $\omega^{m,(k)} = \frac{1}{M}$ (thus, $\omega^{m,(k-1)}$ can be omitted from (2.8)). The particle filtering algorithm iterates until convergence of the MAP state.

Algorithm 2.1: Histological slices to volumetric image registration using particle filtering (see Table 2.1 for a list of parameters).

```
Input: $\{I_n\}_{n=0}^{N-1}$, $\{H_n\}_{n=0}^{N-1}$, $\{z_n\}_{n=0}^{N-1}$, $J$,
       $\{\sigma_i^2\}$, $\{\eta_i^2\}$, $\sigma_v^2$
       $M$, $L$, $\gamma$, $\alpha$, $p(\bar{S}^{(0)})$.
Output: $p(\bar{S}^{(k)}|J)$, $\bar{S}^{\mathrm{MAP},(k)}$ (at each time step $k$).
Initialization: generate $\{\bar{S}^{m,(0)}\}_{m=1}^{M}$ according to $p(\bar{S}^{(0)})$,
                set weights $\{\omega^{m,(0)}\}_{m=1}^{M}$ to $\frac{1}{M}$,
                $k = 1$.
  repeat
    for $m = 1$ to $M$ do
      obtain prediction:
        $\hat{\bar{S}}^{m,(k)} = \bar{S}^{m,(k-1)} + \sqrt{\gamma^{k-1}} U^{m,(k)}$.
      perform updates: $\bar{S}^{m,(k)} = F_{\min}^{L}(\hat{\bar{S}}^{m,(k)}, J)$.
      calculate prior: $p(\bar{S}^{m,(k)}|\bar{S}^{m,(k-1)})$ using (2.5).
      calculate likelihood: $p(J|\bar{S}^{m,(k)})$ using (2.6).
      set weight:
        $\omega^{m,(k)} \propto p(J|\bar{S}^{m,(k)}) p(\bar{S}^{m,(k)}|\bar{S}^{m,(k-1)})$.
    end for
    normalize weights such that: $\sum_{m=1}^{M} \omega^{m,(k)} = 1$.
    approximate posterior:
      $p(\bar{S}^{(k)}|J) = \sum_{m=1}^{M} \omega^{m,(k)} \delta(\bar{S}^{(k)} - \bar{S}^{m,(k)})$.
    resample $\{\bar{S}^{m,(k)}\}_{m=1}^{M}$ according to the posterior.
    reset weights $\{\omega^{m,(k)}\}_{m=1}^{M}$ to $\frac{1}{M}$.
    $k := k + 1$.
  until convergence.
```

2.3.5 Similarity Metrics

We consider three types of metrics according to the imaging modality of the volume. On the *ex vivo* MR data sets, for which intensity information has been shown to be useful in registration to histology [24, 171], we employ the intensity-based MI metric.

For the *in vivo* MR data sets, we found that the MI metric fails to match the histological slices to the volume on some cases, and we apply a region-based metric instead. Such metrics employ intensity statistics to describe the prostate region, and have been shown to be useful for automatic segmentation of the prostate in T2w MR [163].

For the US data sets, we found that the metrics above fail to measure similarity to histology. Therefore, we assume that the volumetric image J is segmented as well and use a point-based metric, namely, the closest point metric. An illustration of the minimization process of the two similarity metrics is shown in Figure 2.3.

Intensity-Based

We employ the inverse of the (normalized) MI [26, 165] between the histological slice I_n and the re-sliced image $\tilde{J}_n$ with respect to the pose $\bar{s}_n$. In this case, the distance functional in (2.3) is

$$D[I_n(\cdot), J(\cdot); H_n(\cdot), \bar{s}_n] = \frac{E[I_n(\cdot), \tilde{J}_n(\cdot; \bar{s}_n)]}{E[I_n(\cdot)] + E[\tilde{J}_n(\cdot; \bar{s}_n)]}, \tag{2.11}$$

where $E[I_n]$ and $E[\tilde{J}_n]$ are the intensity entropies of the 2-D slice I_n and re-sliced image $\tilde{J}_n$, respectively, while $E[I_n, \tilde{J}_n]$ is their joint entropy [122]. The entropies are calculated using the marginal and joint histograms of the region inside the segmented histological slice, and its corresponding region in the re-sliced volumetric image.

Region-Based

We employ the Chan-Vese metric [23] that is typically used as an active contours model for segmentation. The metric minimizes the intensity variances of the re-sliced image $\tilde{J}_n$ on the regions inside and outside the segmentation contour of the corresponding histological slice I_n. The metric is minimized with respect to the pose $\bar{s}_n$, and thus may be seen as fitting the re-sliced image to the contour of the histology, rather than evolving the contour to segment the image as was done in [163].

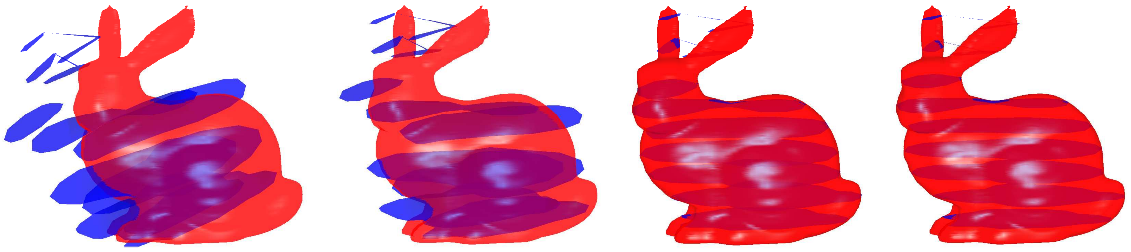

(a) Initial state (b) After initial alignment (c) Final MAP state (d) True state

Figure 2.4: Registration of synthetic data: illustration of the algorithm stages. The ground-truth, (d), is shown in comparison with the MAP state resulting from the proposed algorithm, (c).

In this case, the distance functional in (2.3) is

$$\begin{aligned} D[I_n(\cdot), J(\cdot); H_n(\cdot), \bar{s}_n] = &\int_{\mathbb{R}^2} (\tilde{J}_n(x,y;\bar{s}_n) - c_{in})^2 H_n(x,y)\, dxdy \\ &+ \int_{\mathbb{R}^2} (\tilde{J}_n(x,y;\bar{s}_n) - c_{out})^2 (1 - H_n(x,y))\, dxdy, \end{aligned} \tag{2.12}$$

where c_{in} and c_{out} are the mean intensities of the re-sliced image $\tilde{J}_n$ inside and outside the histological contour, respectively.

Point-Based

Here, we assume that the contour of each histological slice I_n is represented by Q_n points, $\{\bar{r}_q^{I_n}\}_{q=1}^{Q_n}$, and the surface in the segmented volumetric image J is represented by a cloud of P points, $\{\bar{r}_p^J\}_{p=1}^{P}$. We employ the SSD between pairs of closest points in the point clouds of the volume and in transformed histology slice $\tilde{\bar{r}}_q^{I_n} = T(\bar{s}_n)\bar{r}_q^{I_n}$ with respect to the pose $\bar{s}_n$. Thus, the distance functional in (2.3) is

$$D[I_n(\cdot), J(\cdot); H_n(\cdot), \bar{s}_n] = \frac{1}{Q}\sum_{q=1}^{Q} \|\tilde{\bar{r}}_q^{I_n} - \bar{r}_{p_q}^J\|^2, \tag{2.13}$$

where we employ the ℓ_2 norm $\|\cdot\|$ (Euclidean distance), and $\bar{r}_{p_q}^J$ is the point in J that is closest to $\tilde{\bar{r}}_q^{I_n}$ in I_n with respect to the norm.

2.4 Experiments

2.4.1 Synthetic Case

We have tested and evaluated the proposed multi-slice to surface registration algorithm on a synthetic data set for which we know the ground truth. Specifically, we used the 3-D point data set of the Stanford Bunny [155] as the segmented volumetric image, and generated nine slices of 256×256 pixels from cross-sections of the volume. Rather than transforming the surface, we applied random transformations to each of the slices by sampling an initial state from the prior distribution (2.5) around some mean state (different from the true state). We allowed both different in-plane poses among slices, in order to model the misalignment during slide scanning, and different out-of-plane poses that yield non-parallel slices (without violating the non-intersecting slices constraint) that implicitly model bending of the surface.

Figures 2.4(a)-2.4(c) show the registration process between the contours of the slices and the surface after employing the proposed algorithm for 10 time steps with 100 particles. Since the data is given as point cloud, we used the point-based metric described in Section 2.3.5 below. Figure 2.4(d) shows the true state of the slices for a qualitative evaluation of the results.

A quantitative evaluation of the results is provided in Figure 2.5. In Figure 2.5(a), the mean squared distance between contour points of the MAP state's slices and their counterparts on the surface (the objective metric), as well as their mean squared distance to the corresponding contour points of the ground truth state's slices, obtained by using 100 particles are plotted versus the number of filtering iterations. Indeed, the distances from the MAP to surface points, and from the MAP to ground truth points are minimized and converge to 1.67 ± 0.65 pixels ($0.7 \pm 0.3\%$) and 2.98 ± 1.16 ($1.1 \pm 0.4\%$) pixels, respectively

In order to evaluate the sensitivity of the results to the number of particles, we reran the experiment with five filtering iterations for different number of particles (the rest of the parameters were fixed). Figure 2.5(b) shows that indeed the trend is that the objective metric decreases as the number of particle increases. We note that comparison of the results achieved by using fewer particles (a single particle in particular), to those achieved by using many particles, can be regarded as a comparison of our stochastic approach to a deterministic algorithm such as [171]. Also, we note that with 150 particles and five filtering iterations, the obtained distances from MAP to surface points, and from MAP to ground truth points are 1.38 ± 0.86 pixels ($0.5 \pm 0.3\%$) and 2.59 ± 0.98 pixels ($1.0 \pm 0.4\%$), respectively, which are lower than those obtained for 100 particles and 10 filtering iterations. This is due to the quick convergence of the algorithm with respect to the filtering iterations, and the fact that more particles allow further "exploration" of the search space.

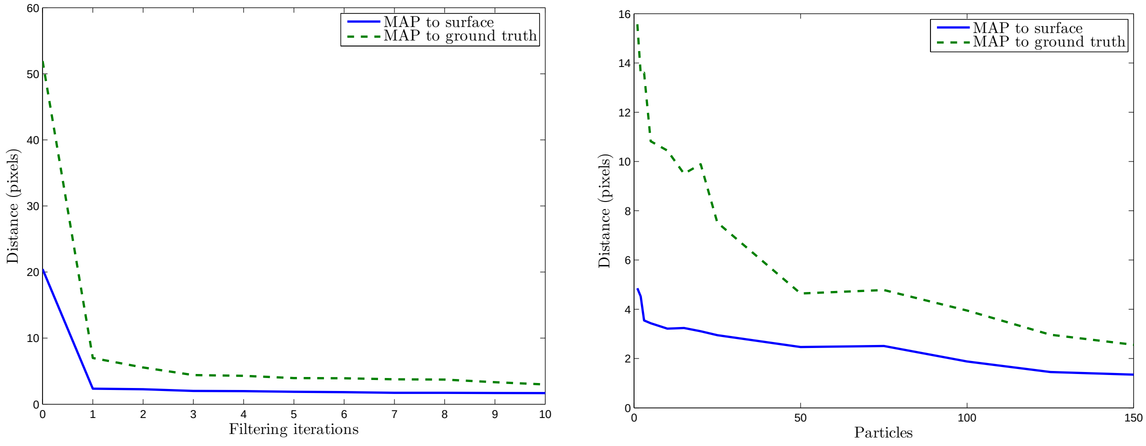

(a) (b)

Figure 2.5: Registration of synthetic data: sensitivity analysis. (a) sensitivity of the algorithm to the number of filtering iterations (with 100 particles). (b) sensitivity of the algorithm to the number of particles (with 5 filtering iterations). The mean squared distance between contour points of the MAP state and the surface/ground truth are used as performance indicators (see text).

2.4.2 Clinical Data Acquisition

After approval of the institutional ethics board and signed consents, ten patients (mean age 65, range 57–76 years old) who were scheduled for radical prostatectomy, underwent preoperative MR and intraoperative US. A postoperative MR was acquired for the prostate specimen as well. We have tested the proposed method in order to register the histology scans to the different imaging modalities of each case.

In Vivo MR

A T2w scan in a 3-Tesla system (Achieva 3.0T, Philips, The Netherlands) was performed. A standard 6-channel cardiac coil with acceleration factor (SENSE) 2 was used. A standard axial T2w fast spin-echo (FSE) sequence was acquired (echo time (TE)/pulse repetition time (TR) = 86/2500 ms, field of view (FOV) = $320 \times 320 \times 70$ mm^3, with 0.5 mm in-plane resolution and 2 mm slice thickness).

Notation	Description	Typical values	Remarks
K	Number of time steps (filtering iterations)	10	More steps allow convergence of the particles, but increase runtime; Increased with the degree of uncertainty.
M	Number of particles	250	More particles estimate the posterior better, but are computationally expensive; Increased with the number of slices N.
L	Number of update iterations	5 (intensity-based) 10 (region-based) 25 (point-based)	High number of iterations lead to (noisy) data overfitting; Low number of iterations lead to slow convergence.
α_n	Slice weighting	0.5 ($n = 0, N-1$), 1 (otherwise)	High values prioritize slices; Is used to neglect the base and apex.
γ	Pose discount factor	0.85	Low values reflect decrease of uncertainty (pose STDV) with every filtering iteration.
$\sigma_{\Delta_{x,y}}$	In-plane translation STDV	3 mm	In-plane misalignment occurs during sliding the slices and scanning the slides; Statistically independent among slices.
σ_{θ_z}	In-plane rotation STDV	3°	
$\eta_{\Delta_{x,y}}$	In-plane translation slice difference STDV	$\sqrt{2} \cdot \sigma_{\Delta_{x,y}}$	
η_{θ_z}	In-plane rotation slice difference STDV	$\sqrt{2} \cdot \sigma_{\theta_z}$	
σ_{Δ_z}	Out-of-plane translation STDV	1 mm (*ex vivo* MR) 3 mm (*in vivo* MR, US)	Out-of-plane misalignment occurs during sectioning of the specimen;
$\sigma_{\theta_{x,y}}$	Out-of-plane rotation STDV	1° (*ex vivo* MR) 3° (*in vivo* MR, US)	
η_{Δ_z}	Out-of-plane translation slice difference STDV	$0.1 \cdot \sigma_{\Delta_z}$	Highly dependent among slices when using a multi-bladed cutting device (equally spaced and parallel slices).
$\eta_{\theta_{x,y}}$	Out-of-plane rotation slice difference STDV	$0.1 \cdot \sigma_{\theta_{x,y}}$	
$\sigma_{\xi_{x,y,z}}$	Scaling STDV	0.1 (*ex vivo* MR) 0.3 (*in vivo* MR, US)	Occurs during excision and fixation of the specimen;
$\eta_{\xi_{x,y,z}}$	Scaling slice difference STDV	$0.01 \cdot \sigma_{\xi_{x,y,z}}$	Highly dependent among slices. Values are logarithmic.
σ_v	imaging noise STDV (intensity-, region-based) / surface error STDV (point-based metric)	3% dynamic range 1 mm	Affects the likelihood of states; High values favour the updated state, lower values favour the predicted state.

Table 2.1: Summary of the parameters.

In Vivo US

Intraoperatively, prior to the procedure, B-mode images were collected using an US machine (Sonix RP, Ultrasonix Medical, Richmond, BC, Canada) with a biplane transrectal probe (BPL9-5/55, 5–9 MHz) that was mounted on a motorized system [143], to collect a continuous sagittal sweep from -45° to 45° that spans a 3-D volume (FOV $= 84 \times 50 \times 56$ mm^3). The volume was then interpolated in order to produce conventional transverse images of the prostate (with 0.3 and 0.42 mm in-plane and axial resolution, respectively).

The prostate in the transverse volume was segmented by a radiologist on key slices (every $\sim 5 - 7$ slices in a volume of 128 slices), in which the prostate was visualized better. The radiologist also used the corresponding sagittal view for assistance, and relied on symmetry of the gland to guide its contouring. We have used Stradwin (Cambridge University, UK), [160], which employs [161] in order to interpolate the sparse contours on intermediate slices and generate a triangulated surface of the prostate. We set the surface resolution and smoothing strength of the algorithm to medium.

Ex Vivo MR

After fixation and right before sectioning, the postoperative prostate specimen was wrapped in a plastic bag, taped to a dedicated holder and scanned in a 7-Tesla system (Biospec, Bruker, Germany). A rapid acquisition with relaxation enhancement (RARE) pulse sequence was used to acquire axial T2w images (TE/TR $= 70/5000$ ms, FOV $= 70 \times 70 \times 42$ mm^3, with 0.2734 mm in-plane resolution and 2 mm slice thickness).

Whole-Mount Histology

The multi-bladed cutting device in [32] was used for whole-mount sectioning of the specimen in order to minimize orientation and spacing variance among the sections. Following the histology preparation process described in Section 2.1, cancerous regions were marked by a pathologist on the histological slides. A typical number of 8-10 slides were then digitally scanned using a commercial flatbed Scanner with 600 DPI that yields an in-plane resolution of about 0.17 mm. The prostate boundary was segmented manually on each of the histological slices. Although the segmentation was relatively fast ($<$ 1 min per slice) and straightforward due to the small number of slices and homogeneous background, the clear boundaries may also allow employment of a (semi-) automatic segmentation algorithm.

2.4.3 Parameter Selection and Implementation Details

We have tuned the registration parameters by first running the algorithm multiple times on a study data set from each modality, and then applying these values to the rest of the data sets of the same modality. A summary of the different parameters and their assigned values is presented in Table 2.1. Below we explain the reasoning behind some of the choices.

As a rule of thumb, the number of particles should be increased exponentially with the dimensionality of the state-space [30] ($9N$ in our case). However, as in [125] and [141], due to the importance sampling we employ, the actual growth in particles is less than exponential, and for a typical number of 10 slices, we found that $100 - 250$ particles are required. With no time limitation, we have chosen the upper value of that range to increase the chances of converging to the global minimum.

From our observations, we have also estimated typical values for the uncertainty in the pose parameters. We set the variance of each pose parameter using the fact that about 99.7% of the samples drawn from a normal distribution are within three standard deviations (STDVs) from the mean, which is initially taken as zero (before initial alignment). Since we have used a multi-bladed cutting device, we set low values to the variances of the out-of-plane pose difference among slices to reflect the high probability of equally spaced and parallel slices. Without prior knowledge about the in-plane pose, we set their difference variances to allow a statistical independence. We have also set the imaging noise to be relative to the dynamic range of the images, when the intensity- or region-based metrics were employed, and estimated the surface segmentation error for the point-based metric.

We note that, while keeping the same number of particles and assuming equally spaced and parallel slices, the algorithm is robust with respect to the choice of the pose variances, with similar results achieved for a range of STDVs in the order of a few mm or degrees. This is due to a fast convergence ($2 - 3$ filtering iterations) of the particles to a state-space region around the true state.

To minimize the metrics with respect to the state vector we employed the Nelder-Mead simplex method for the intensity-based metric, a gradient descent for the region-based metric, and the iterative closest point (ICP) algorithm [15] for the point-based metric. As described in Section 2.3.4, the number of iterations in the update stage (2.9) was chosen to be relatively low to avoid overfitting of the histological slices to the volumetric image. We note that, since the Nelder-Mead optimization process is not smooth, the algorithm is sensitive to the number of update iterations when employing the intensity-based metric, and this number should be kept low to avoid “drifting” of the state. Consequently, more particles and filtering iterations are usually required in comparison to the point-based metric.

We used a discount factor of $\gamma = 0.85$ to reflect the decrease in uncertainty with every time step. We also set the weights $\alpha_0 = \alpha_{N-1} = 0.5$ and $\alpha_n = 1,\ n = 1, \ldots, N-2$, in order to prioritize the mid-gland slices, for which, typically, prostate imaging is more reliable than for the top and bottom slices (base and apex). This is due to ambiguity in boundaries of the gland on extreme slices, where its apex and base blend into the pelvic floor and the bladder neck tissue, respectively, and thus we would like the algorithm to be less affected by them. When using a sufficient number of particles, the algorithm is robust with respect to the choice of values for both the discount factor and weights. However, employing these parameters may speed up the convergence of the algorithm, and in our experiments they were set by a trial-and-error process on example cases.

We have implemented our registration method and tested it under MATLAB on a 2.93 GHz Quad Core CPU machine with 8 GB of RAM. The average runtime per registration was 25 minutes for the point-based metric cases, 8 hours for the region-based metric cases, and 3 hours for the intensity-based metric cases.

2.4.4 Results

To evaluate the registration performance on the clinical data, we compare the registered histological slices with the corresponding re-sliced images of the volume. For each slice, we compare its histological segmentation with the corresponding cross-section of the prostate surface, as obtained from a manual segmentation of the volumetric image by a radiologist. We measure the area overlap of the regions inside the two segmentation contours, in the sense of Dice's coefficient, i.e., twice the size of the intersected area divided by the sum of the sizes of the areas.

In addition, for the MR cases, the radiologist has identified matching landmarks inside the prostate on both the histology and volumetric images after manually selecting corresponding slices. These landmarks include the urethra, nodules, scars (from previous biopsies), calcifications and other general distinguished anatomical features.

We measure the Euclidean distance between the registered landmarks on histology and their counterparts in the volume. These distances provide us a good approximation of the target registration error. Since, typically, the 3-D coordinates of the landmarks in the volume do not lie exactly on the registered slice, we show the projections of the landmarks on that plane (however, the error is calculated in 3-D).

Selected histological slices and their corresponding re-sliced volume images according to the registration results are shown in Figure 2.6 for each type of imaging. The quantitative results for each modality are also summarized in Table 2.2.

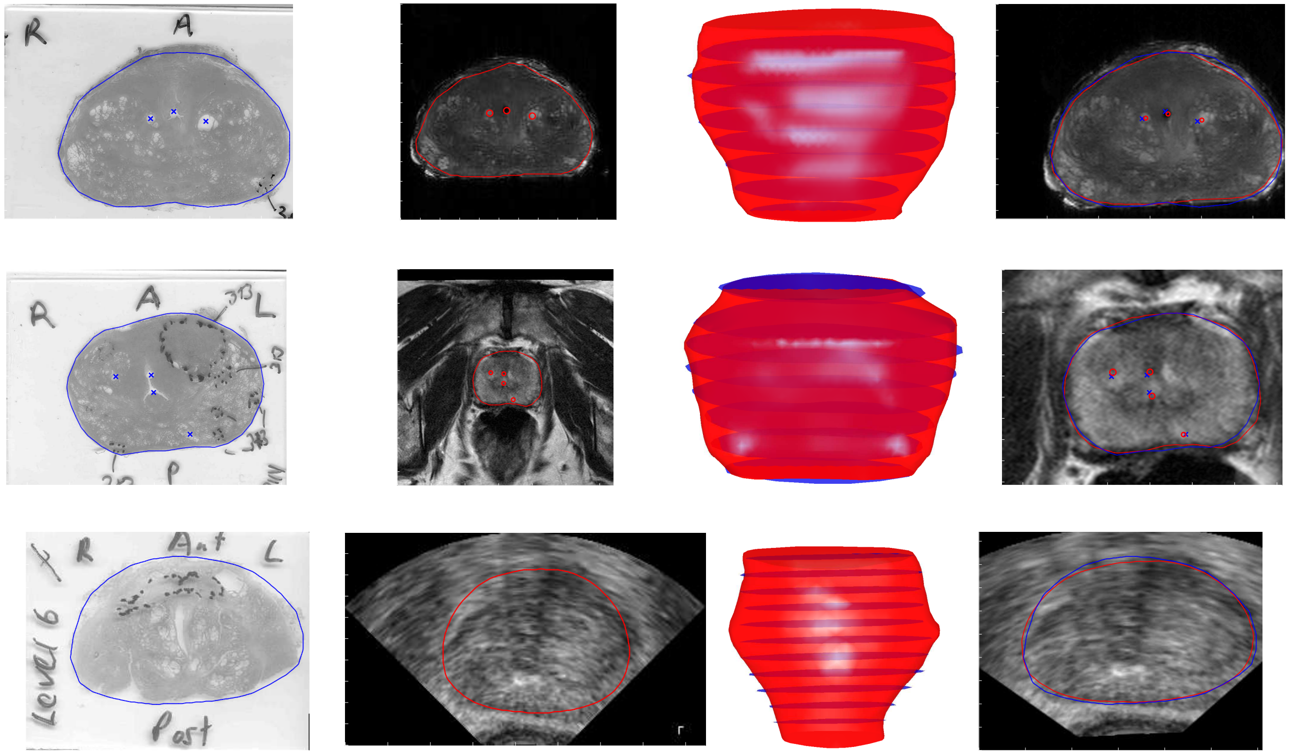

(a) Histological slice (b) Imaged slice (selected manually) (c) Registration results (d) Registered slice (automatic)

Figure 2.6: Registration results. Example slices from *ex vivo* MR (top row), *in vivo* MR (middle row) and *in vivo* US (bottom row) imaging. A mid-gland histological scan (left column), a manually selected corresponding volumetric slice (second left column), visualization of the registration results (second right column), and the corresponding registered volumetric slice. The segmentation (contour) and landmarks (markers) of the histology (blue) and volumetric imaging (red) are overlaid on the images.

	Histology to *ex vivo* MR			Histology to *in vivo* MR			Histology to *in vivo* US
	Area overlap (%)	Mean error (mm)	Min-max error (mm) [# of landmarks]	Area overlap (%)	Mean error (mm)	Min-max error (mm) [# of landmarks]	Area overlap (%)
Case 1	93.0 ± 6.5	1.8 ± 1.0	$0.8 - 5.0$ [11]	89.2 ± 5.7	3.4 ± 1.6	$0.9 - 5.6$ [11]	91.1 ± 4.1
Case 2	94.7 ± 1.4	1.5 ± 1.0	$0.5 - 3.5$ [9]	91.0 ± 4.1	2.9 ± 1.6	$0.3 - 5.3$ [9]	93.0 ± 2.7
Case 3	93.1 ± 2.2	1.4 ± 0.5	$0.4 - 2.5$ [14]	89.2 ± 6.4	3.2 ± 1.3	$0.7 - 5.2$ [14]	92.7 ± 1.2
Case 4	94.4 ± 3.2	1.6 ± 0.5	$0.2 - 2.6$ [13]	86.1 ± 7.1	4.3 ± 1.6	$1.0 - 7.1$ [13]	94.2 ± 2.1
Case 5	90.2 ± 4.1	1.4 ± 0.5	$0.6 - 2.2$ [19]	81.5 ± 6.3	4.1 ± 1.5	$1.5 - 6.7$ [19]	89.1 ± 4.9
Case 6	91.4 ± 5.0	1.6 ± 0.7	$0.5 - 3.0$ [14]	87.1 ± 8.0	3.3 ± 1.1	$1.1 - 4.9$ [14]	92.4 ± 1.8
Case 7	94.1 ± 1.3	1.4 ± 0.3	$0.8 - 1.9$ [10]	92.2 ± 5.3	2.8 ± 1.3	$0.8 - 4.6$ [10]	90.5 ± 2.9
Case 8	91.9 ± 5.5	1.6 ± 0.6	$0.6 - 2.6$ [12]	84.4 ± 10.3	3.9 ± 1.2	$1.8 - 5.4$ [12]	87.1 ± 8.4
Case 9	89.9 ± 23.8	1.7 ± 0.6	$1.0 - 2.7$ [12]	79.1 ± 8.9	6.1 ± 2.5	$2.0 - 9.4$ [12]	85.1 ± 14.1
Case 10	94.5 ± 1.8	4.4 ± 1.2	$2.5 - 6.5$ [20]	84.7 ± 12.6	3.9 ± 1.0	$1.8 - 5.3$ [20]	93.8 ± 0.9
Mean	92.0 ± 5.6	1.7 ± 1.2	$0.8 - 3.3$ [14]	86.9 ± 8.2	3.8 ± 1.5	$1.3 - 5.9$ [14]	90.1 ± 5.8

Table 2.2: Registration results. Quantitative summary.

2.5 Discussion and Conclusion

We presented a method for a multi-slice to volume registration in order to solve the challenging clinical problem of alignment between histological slices and volumetric imaging of the prostate. The proposed algorithm does not alter the clinical flow of histopathological processing, and can be employed to characterize CaP and evaluate its localization in volumetric images by allowing the mapping of lesions, which are marked by a pathologist on the histological slices, onto the volume.

The proposed algorithm has been evaluated on both synthetic and clinical data. The experiments on synthetic data, for which the ground truth of slices' pose with respect to the surface is known, showed a fast convergence of the algorithm and its ability to recover the pose while avoiding local optima. The registration of histological slices to *ex vivo* MR, *in vivo* MR, and *in vivo* US achieved relatively high area overlaps and registration errors below the diameter of typical lesions that are marked during histopathology analysis ($\sim 10 \pm 5$ mm [34]).

Lower error values were obtained in the *ex vivo* MR experiments. This is due to the fact that the *ex vivo* MR scan is performed after excision and fixation, and just before sectioning, and therefore captures the shape of the deformed specimen, between which the histological slices are more likely to have a rigid transformation. Surprisingly, the resulting area overlaps in the registered *in vivo* US cases are comparable to those in the *ex vivo* MR cases. We believe this is due to the high resolution of the US scans that allowed a good reconstruction of the imaged prostate's surface, to which the slices are directly registered using the point-based metric.

In most cases, the error ranges in Table 2.2 are below the clinical significance cancerous tumor threshold of 0.2 cm^3 in volume, as reported in [36], which translates to a spherical tumor of 7.2 mm in diameter. Thus, for the intended application of cancer characterization, such errors should allow feature extraction and training of classification algorithms, e.g., support vector machines [146] or random forests [19], with techniques to discard possible outliers caused by larger registration errors.

The employment of a particle filtering framework allows us to contend with the high dimensionality of the constrained search space, and with the multimodal nature of the optimization problem. The uncertainties in the alignment, imaging noise and surface error are modeled stochastically, which allows derivation of optimal registration parameters in a Bayesian approach.

Other methods that employ PFs for registration typically assume a system noise associated with a diagonal covariance matrix, i.e., such that the state parameters are statistically independent. Here, in addition to the novel application of the algorithm to a multi-slice to volume registration, we have incorporated a misalignment model into the PF framework through a parameterized structure of the covariance matrix. This covariance matrix allows the generation of slice poses that are correlated according to the misalignment mechanisms in histopathological processing.

The incorporation of intensity-, region- and point-based similarity metrics into the registration algorithm, in order to account for the different imaging modalities, demonstrates the generality and flexibility of the proposed method, with which any similarity metric can be employed. Specifically, we have employed the MI and Chan-Vese metrics on the *ex vivo* and *in vivo* MR data sets, respectively, based on their previously reported successful applications to these modalities (see Section 2.3.5). In case these metrics do not perform well due to corrupted or noisy data, the simple SSD between closest points that was employed on the US data sets can still be used as the metric for these modalities, at the expense of an added segmentation or other processing of the volumetric image.

The main limitation of the proposed method, which stems from its generality, is the relative high number of parameters. Tuning these parameters requires a preliminary study of the variances of the misalignment, and/or a trial-and-error process. However, as discussed in Section 2.4.3, we found the algorithm to be robust within a range of parameters' values, and in most scenarios they need to be set only once for processing data sets that were acquired under the same clinical settings.

Note that, due to its stochastic nature, running the algorithm on the same data set under the same parameters may still yield different results. However, in case the parameters are tuned properly, the variance among such results is not significant as they should all be around the global minimum. To ensure a convergence to a global minima, a high number of particles should be employed, which makes the algorithm computationally expensive. However, in a typical setting, the algorithm is running offline, after histopathology processing, and therefore registration time may be expendable.

Another drawback of the current implementation is that the rigid transformation with anisotropic scaling we assume is unable to fully capture distortion caused by tear, shear, fold, or stretch, as assumed in [60] (a small percentage of slices in our data, on which gland segmentation was approximated by the expert). A straightforward extension of our method is to consider a full affine transformation by adding three additional shear parameters, one per axis, with corresponding standard variations. However, in that case, additional particles and/or iteration are expected to be required for convergence.

The proposed framework can be also extended to accommodate a deformable registration step. Such a step can further improve the results by capturing any residual deformations, and is required, e.g., when using an endorectal coil for acquiring *in vivo* MR. Any deformable registration algorithm can be employed based on the data, e.g., an intensity-based algorithm such as free-form deformations [130], or a point-based algorithm such as landmark-based thin-plate splines [128]. We note that, due to the sparsity of slices, a 2-D registration should be applied between each histological slice and its corresponding registered slice on the volumetric image.

In case a 3-D deformation map between the specimen and *in vivo* imaging is required, a possible approach is to first register the histology to an *ex vivo* MR with minimal error using the proposed algorithm, and then compose the resulting transformation with a deformable mapping that was obtained from a 3-D elastic registration between the *ex vivo* MR and the *in vivo* MR, e.g., using the method described in Chapter 3. Future work may include the employment of such nonrigid registration algorithms, either as postprocessing, or as part of the particle filtering framework.

With the proposed similarity metrics, the approach is either susceptible to segmentation errors, or to lack of intensity features. Future work may improve the usage of the MI metric by employing a Parzen window approximation [165] to allow a smooth minimization of the intensity-based metric. This will increase the robustness of the algorithm to the choice of the number of update iterations when using the intensity-based metric.

Other future work includes investigation of more metrics that can describe the similarity between histological slices and volumetric imaging. Specifically, we are interested in employing a point-based metric between descriptors of intensity-based extracted features. Incorporated into our PF framework, such metric will allow avoiding segmentation, as when intensity-based metrics are used, while benefiting from the shorter runtime of a point-based metric. An automatic extraction of salient features can be based, e.g., on a scale invariant approach, as proposed in [175], or on the modality independent neighbourhood descriptor [55] that has recently gained popularity for multimodality registration of medical imaging, including the prostate [156]. Another research direction is to employ a linear combination of metrics as the similarity, and either train or manually tune their weights in order to provide a better shaping of the target functional according to the data.

Chapter 3

Model-Based Registration of the Prostate Using Elastography

3.1 Introduction

As discussed in Chapter 2, a typical sparse sectioning of histological slices does not allow a direct construction of a 3-D deformation map between the specimen and *in vivo* imaging. Recently, researchers have proposed the use of an *ex vivo* MRI of the prostate specimen [167, 168] as an intermediate modality between histopathology and *in vivo* MRI. Performed after excision and fixation, and just before sectioning, such *ex vivo* scan captures the shape of the deformed specimen, and can therefore be better aligned with the histological slices using only a rigid registration. Compared to the histological slices, the superior axial resolution of the *ex vivo* scan provides true 3-D modeling of the specimen that facilitates a nonrigid registration to the *in vivo* MRI.

Thus, the slice-to-volume registration of histological sections to *in vivo* MRI can be divided into two more tractable registrations of histopathology to *ex vivo* MRI, and *ex vivo* to *in vivo* MRI. The former registration can be solved with minimal error by approaches proposed, e.g., in [45] and [70], or by employing a multi-bladed cutting device [32] that mechanically constrains the prostate specimen during sectioning. For the latter registration, however, the authors in [167] propose only an interactive rigid registration between the *in vivo* and *ex vivo* volumes, which has been recognized to be a shortcoming [168].

It is the objective of the work described in this chapter to develop and validate a method for an automatic and accurate 3-D registration between *ex vivo* and *in vivo* MRI. Figure 3.1 illustrates the problem with typical images to be registered. We propose a novel deformable registration approach, in which the *ex vivo* MRI volume of the prostate is segmented and treated as a reference model, and the *in vivo* MRI volume is treated as a deformable template with an underlying patient-specific biomechanical model. First, a similarity transformation (translation, rotation and isotropic scaling) is employed to align the *ex vivo* and *in vivo* scans and correct for the change in volume. Following this initial alignment, an elastic registration is performed to match the template with the reference. Similar to [76], the

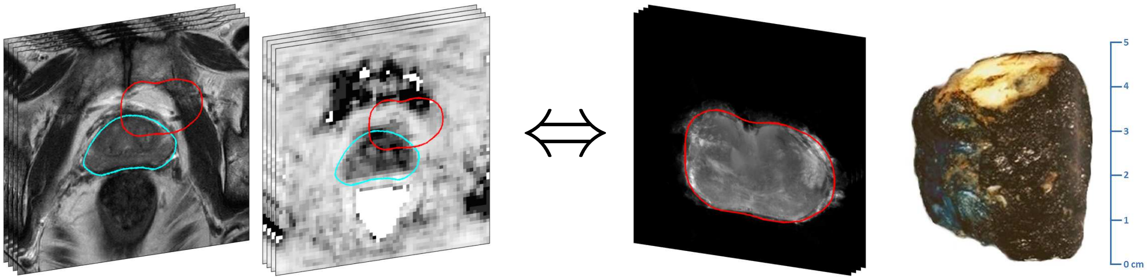

(a) *In vivo* T2w (b) MRE elastogram (c) *Ex vivo* T2w (d) Prostate specimen

Figure 3.1: Problem illustration. (a)-(b) The *in vivo* MRE scan provides measured elasticity for each imaged voxel. (c)-(d) A 3-D model of the postoperative specimen, acquired from *ex vivo* MRI, should be registered to the *in vivo* MRI. Cross-sections of the unregistered *ex vivo* model (red) and the unknown *in vivo* prostate surface (cyan) are overlaid on slices.

deformation is driven by a region-based energy as the distance measure, and the elastic potential as a regularizer. Unlike [76], we deform the image in order to fit the model, and use an *inhomogeneous* biomechanical model, acquired from MRE [100], in our regularization term.

While potentially faster because of the much coarser discretization of images, biomechanical models derived from the FEM, such as those employed in [16] and [5], require segmentation and meshing of the internal structure of the prostate and its surrounding anatomy. These steps are time consuming, often require user intervention and may generate errors that affect registration performance. Unlike FEM-based approaches, our method allows to solve the registration problem on a regular grid by using a variational approach and eliminates volume meshing. Such an approach was successfully employed in [13] for US image registration in prostate biopsy tracking.

The MRE technique that we use integrates relatively easily in a standard multi-parametric *in vivo* MRI session. It involves the transperineal application of single- or multiple-tone harmonic mechanical excitation that generates shear waves in the prostate. The waves are measured by encoding the resulting displacements in the phase component of a synchronized MRI pulse sequence. Images, known as elastograms, that depict tissue elasticity or stiffness are generated from the imaged tissue displacements. With MRE, each voxel in the *in vivo* MRI is associated with the measured elasticity of the corresponding voxel in the elastogram. Additional details about the technique are given in [134] and Section 3.5.1.

With few exceptions, e.g., [29, 64, 78], biomechanical models have been assigned arbitrary and typically constant elastic properties that are optimized to produce low registration errors. Even methods that do consider inhomogeneous elasticity for registration, express tissue inhomogeneity by setting values that are empirically found to work well. This is not always realistic and may result in inaccurate deformation maps.

In general, the current use of elastography in image processing is limited (see [140] for a review on applications in prostate imaging), and, in particular, the use of patient-specific elasticity maps for registration is new. We justify our approach by providing a novel quantitative analysis that shows the advantage in utilizing inhomogeneous elasticity for registration. We validate the method by presenting the results from synthetic and six patient data sets.

The remainder of this chapter is organized as follows. Section 3.2 describes the theory and basic ideas behind the proposed methods. Section 3.3 presents a method for registering the *ex vivo* model to an *in vivo* volume using elastography. In Section 3.4 we investigate the registration performance with respect to elastic inhomogeneity. In Section 3.5, we provide experimental results of the proposed registration method on clinical data. Finally, we conclude in Section 3.6 with a discussion and future research directions.

3.2 Preliminaries

3.2.1 Elastic Registration

We denote the 3-D spatial coordinate vector as $\bar{r} = (x, y, z)^T \in \mathbb{R}^3$. Let $I_R,\ I_T \colon \mathcal{D} \to \mathbb{R}$ denote the reference and template volumes, respectively, on a 3-D domain $\mathcal{D} \subseteq \mathbb{R}^3$. Also, let $\bar{u} = (u_x, u_y, u_z)^T \colon \mathcal{D} \to \mathbb{R}^3$ be a displacement field, such that the deformed template with respect to $\bar{u}$ is

$$\tilde{I}_T(\bar{r}; \bar{u}) = I_T(\bar{r} - \bar{u}(\bar{r})). \tag{3.1}$$

The elastic registration problem is finding an admissible displacement field $\bar{u}$, such that the deformed template $\tilde{I}_T$ is similar, in some sense, to the reference I_R. This problem is formulated as the minimization of the joint functional, or energy,

$$\mathcal{J}[\bar{u}; I_R, I_T] = \mathcal{F}[I_R, \tilde{I}_T(\cdot; \bar{u})] + \mathcal{S}[\bar{u}] \ , \tag{3.2}$$

where $\mathcal{F}$ represents a distance measure between the reference and the deformed template, and $\mathcal{S}$ is a metric that determines the smoothness or regularization of the displacements.

Common choices for a distance measure are SSD, NCC and (normalized) MI [165]. In [76], the authors proposed a region-based energy (see Section 3.2.2) as the distance measure for a combined segmentation and registration. Their method maps a contour, which is extracted from a segmented template image, onto the reference image to provide the segmentation of the reference and its spatial correspondence with the template.

A variety of metrics have been proposed to regularize the deformations based on physical models, e.g., diffusion [58], fluid [25] and curvature [41] models. The authors in [20] and [11] proposed the linear elastic potential of the displacements as a regularizer, namely

$$\mathcal{S}[\bar{u}] = \int_{\mathcal{D}} \left(\frac{\mu}{4} \sum_{j=1}^{3} \sum_{k=1}^{3} (\frac{\partial \bar{u}_j}{\partial \bar{r}_k} + \frac{\partial \bar{u}_k}{\partial \bar{r}_j})^2 + \frac{\lambda}{2} (\mathrm{div}\ \bar{u})^2 \right) d\bar{r} \ , \tag{3.3}$$

where, from continuum mechanics, λ and μ are the Lamé parameters that reflect the elastic properties (μ is also known as the shear modulus).

We follow the general framework presented in [92], and provide a variational formulation of the nonrigid registration problem and the corresponding Euler-Lagrange equations that characterize a minimizer. In the variational approach, in order to minimize the functional (3.2), the Gâteaux derivative is computed with respect to $\bar{u}$. This yields the Euler-Lagrange equation

$$\mathcal{A}[\bar{u}](\bar{r}) - f(\bar{r}, \bar{u}(\bar{r})) = 0 \ , \tag{3.4}$$

where $-f$, also known as the (external) force, corresponds to the derivative of $\mathcal{F}$, and $\mathcal{A}[\bar{u}]$, also known as the internal force, corresponds to the derivative of $\mathcal{S}$ and typically represents a partial differential operator. Thus, a minimizing displacement map should satisfy this equilibrium equation.

In the case of elastic potential as a regularizer, the Gâteaux derivative of (3.3) yields the Navier-Lamé operator

$$\mathcal{A}[\bar{u}](\bar{r}) = \mu \Delta \bar{u}(\bar{r}) + (\lambda + \mu) \nabla \mathrm{div}\ \bar{u}(\bar{r}) \ , \tag{3.5}$$

for which the Euler-Lagrange equation, (3.4), is a second-order nonlinear PDE, also known as the elastostatic or Navier-Cauchy equation.

3.2.2 Region-Based Active Contours

Active contour models [66] have been extensively employed for image segmentation. In these methods, an initial segmenting surface is evolved in order to minimize an energy functional. Edge-based (classical) active contours, [22, 67], drive the surface to lock onto local maxima of image gradient magnitude values that typically characterize edges. The evolution of the surface in this case depends strictly on nearby pixels, and is therefore local. Region-based active contours, [23, 174], rely on regional statistics, such as sample mean and variance within the image, for the evolution of the segmentation surface, and direct its movement toward boundaries that are not necessarily defined by clear edges. Region-based models are global and tend to be robust to noise, since they take into account intensities within entire regions, rather than intensities of individual pixels.

The level set method, [109, 147], is an effective technique for implicit representation of evolving surfaces, frequently employed to implement active contours algorithms, since it inherently allows for cusps, corners and automatic topological changes. In the level set method, a surface (or contour in 2-D) is embedded as the zero level set of a function Φ. We will use the convention that Φ takes negative values in the region inside the surface and positive values in the region outside. A common choice for a level set function is the signed distance function, of which the value $\Phi(\bar{r})$ at each point $\bar{r}$ equals the Euclidean (ℓ^2) distance to its nearest point on the surface, multiplied by 1 or -1 according to the side of the surface $\bar{r}$ lies in.

Formulating energy functionals and their variations in the level set method often requires usage of the Heaviside function and the Dirac delta function, defined respectively by

$$\mathcal{H}(z) = \begin{cases} 1, & z \geq 0; \\ 0, & z < 0, \end{cases} \qquad \text{and} \quad \delta(z) = \frac{d}{dz}\mathcal{H}(z).$$

In practice, regularized (smoothed) versions of $\mathcal{H}$ and δ are used, as suggested in [23], in order for the minimization process to be less local, thus increasing the chances of reaching a global minimizer, independent of the initial surface.

A popular region-based active contour model for image segmentation was proposed by Chan and Vese in [23]. In its level set formulation, the Chan-Vese algorithm minimizes the following energy functional with respect to the level set function Φ that embeds the segmenting surface,

$$\begin{aligned} \mathcal{F}_{CV}[\Phi; I_T] = &\int_{\mathcal{D}} (I_T - c_-)^2\, \mathcal{H}(-\Phi)\, d\bar{r} \\ &+ \int_{\mathcal{D}} (I_T - c_+)^2\, \mathcal{H}(\Phi)\, d\bar{r}\ , \end{aligned} \tag{3.6}$$

where c_- and c_+ are the mean intensities of the image to be segmented, I_T, in the regions inside and outside the segmenting surface (i.e., the zero level set of Φ), respectively, given by

$$c_{\mp}[\Phi; I_T] = \frac{\int_{\mathcal{D}} I_T \mathcal{H}(\mp\Phi)\, d\bar{r}}{\int_{\mathcal{D}} \mathcal{H}(\mp\Phi)\, d\bar{r}}\ . \tag{3.7}$$

The minimization of (3.6) can be understood as partitioning the image into two homogeneous regions, by minimizing the variances of the intensities on the regions inside and outside the segmenting surface.

3.2.3 Model-Based Alignment

A nonrigid registration typically follows a rigid registration that corrects for the misalignment and change of coordinate systems between the two images. In this work we employ a model-based alignment based on an algorithm that was originally used in [163] for a shape-based segmentation.

Let Φ_R be a level set function that embeds the surface of a reference model, which was extracted by a segmentation of the reference image I_R. A similarity transformation in 3-D is defined by seven pose parameters: three translation values along each axis, three rotation angles about the axes, and one isotropic scale factor. Using a linear transformation of the spatial coordinates, the transformed model may be written as

$$\tilde{\Phi}_R(\bar{r}; \Delta, \theta, \sigma) = \Phi_R(\sigma^{-1}\Theta^{-1}(\bar{r} - \Delta)), \tag{3.8}$$

where Δ and θ are vectors that contain the translation and rotation parameters, respectively, σ is the scale, and Θ is the rotation matrix, which is determined by θ.

The authors in [163] propose to segment medical images by optimally fitting a model onto the image. They extract the principal modes of a training set that comprises different shapes of the target object, and obtain a parametric shape model by tuning the shape parameters, namely the coefficients in a linear combination of the principal modes. Their method minimizes region-based energy functionals in a level set formulation, among them the Chan-Vese energy in (3.6), with respect to the pose and shape parameters.

We consider a single element training set, in which the shape is the surface of the reference model. Since the minimization in this case is performed only with respect to the similarity pose parameters, the method is degenerated into alignment of the model. The function to be minimized is therefore

$$F_{CV}(\Delta, \theta, \sigma) = \mathcal{F}_{CV}[\tilde{\Phi}_R(\cdot; \Delta, \theta, \sigma); I_T]. \tag{3.9}$$

The alignment algorithm employs gradient descent to minimize (3.9) by computing its derivatives with respect to the pose parameters. We refer the interested reader to [163] for details.

3.3 Model-Based Registration Using Inhomogeneous Elasticity

In our framework, high quality *ex vivo* images with a homogeneous background (as seen in Figure 3.1(c)) allow a 3-D model of the prostate to be constructed easily by using either manual, semi- or fully automatic segmentation. In contrast, the *in vivo* images contain surrounding anatomy and tissue, with which the prostate blends. Thus, in our model-based registration, we take the *ex vivo* model as the reference, and the *in vivo* image as the template.

3.3.1 Model-Based Force

Motivated by the adequacy of region-based energies to delineate the prostate in MRI, as demonstrated in [163], we follow a model-based registration approach that incorporates a region-based energy as the distance measure between the template image and the reference model. Specifically, we propose a distance measure which is based on the Chan-Vese energy in (3.6),

$$\mathcal{F}[\bar{u}] = \frac{1}{2}\mathcal{F}_{CV}[\Phi_R; \tilde{I}_T(\cdot;\bar{u})], \tag{3.10}$$

where, as in Section 3.2.3, Φ_R is a level set function that embeds the surface of the reference model. Note that in this formulation, the "segmenting" surface Φ_R is constant and the minimization is with respect to the displacement field.

Thus, in contrast to active contours segmentation methods and the registration approach in [76], here the image is deformed in order to fit the model, rather than the model surface to fit the image. This formulation allows for the inhomogeneous elasticity of the voxels in the template to regularize its deformations, as explained below.

By computing the Gâteaux derivative of (3.10), we have that the force associated with this energy is

$$\begin{aligned} f_{CV}(\bar{r}, \bar{u}(\bar{r})) = &- \left[\left(I_T(\bar{r} - \bar{u}(\bar{r})) - \tilde{c}_-\right) \mathcal{H}(-\Phi_R) \right. \\ &\left. + \left(I_T(\bar{r} - \bar{u}(\bar{r})) - \tilde{c}_+\right) \mathcal{H}(\Phi_R) \right] \nabla I_T(\bar{r} - \bar{u}(\bar{r})) \,, \end{aligned} \tag{3.11}$$

where, analogous to the discussion in Section 3.2.2, $\tilde{c}_-$ and $\tilde{c}_+$ are the mean intensities of the deformed template image in the regions inside and outside the reference model.

Being derived mathematically, the magnitude of the forces acting on the template could be arbitrarily high and may force unrealistic deformation to bring it into the reference. However, using a scaling factor, we can normalize the forces such that their maximum magnitude inside the model is in the order of 0.1 N, which is physically plausible and within the same order of magnitude as the gravitational force on the prostate [157].

3.3.2 Inhomogeneous Regularization

As discussed in Section 3.1, in most elastic registration algorithms, the Lamé parameters λ and μ are constant and chosen arbitrary. In elastography, we obtain measurements of the Young's modulus that is associated with each voxel of the template, $E_T \colon \mathcal{D} \to \mathbb{R}$. The corresponding Lamé parameters in this case are the functions given by

$$\lambda_T = \frac{E_T \cdot \nu}{(1+\nu)(1-2\nu)} \quad \text{and} \quad \mu_T = \frac{E_T}{2(1+\nu)} \ , \tag{3.12}$$

with an (almost) incompressible Poisson ratio $\nu = 0.499$.

Thus, we modify (3.5) to contend with the inhomogeneous Lamé parameters,

$$\begin{aligned} \mathcal{A}_T[\bar{u}](\bar{r}) = {} & \mu_T(\bar{r} - \bar{u}(\bar{r}))\Delta \bar{u}(\bar{r}) \\ & + (\lambda_T(\bar{r} - \bar{u}(\bar{r})) + \mu_T(\bar{r} - \bar{u}(\bar{r})))\nabla \mathrm{div}\ \bar{u}(\bar{r}) \ . \end{aligned} \tag{3.13}$$

Note that λ_T and μ_T are deformed according to the template so as to "follow" its voxels. Also note that (3.13) is only a piecewise constant approximation of the problem. The non-approximated operator, derived by taking the Gâteaux derivative of (3.3) with inhomogeneous Lamé parameters (see, e.g., [29] and [64]), contains terms with gradients of the Lamé functions. Due to the noisy nature of elastography, numerical calculation of these gradients is unreliable and the minimization is unstable. However, the approximation is justified by a typical "slow" spatial variation of the true elasticity (another option is to employ a low-pass filtered elastogram and use the non-approximated operator).

3.3.3 Energy Minimization

In order to solve the PDE (3.4) for the displacements $\bar{u}$, with $\mathcal{A} = \mathcal{A}_T$ and $f = f_{CV}$, we follow a fixed-point iteration scheme [92], in which an initial (e.g., zero) displacement $\bar{u}^{(0)}$ is assumed. We then solve

$$\mathcal{A}_T[\bar{u}^{(k)}](\bar{r}) = f_{CV}(\bar{r}, \bar{u}^{(k-1)}(\bar{r})), \quad k = 1, 2, \ldots, \tag{3.14}$$

for $\bar{u}^{(k)}$, until convergence. Since the elastic model relates to small (infinitesimal) deformations, we chain the resulting displacements at each iteration, as if the deformed template at each iteration is to be registered to the reference.

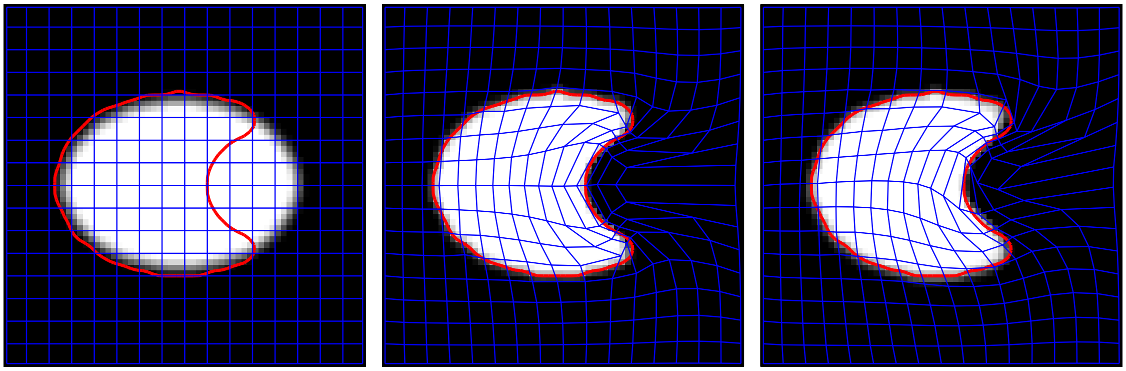

(a) Initial (b) Final (homogeneous) (c) Final (inhomogeneous)

Figure 3.2: Registration of synthetic images. The reference contour (red) is overlaid on (a) the initial binary template, and (b)-(c) the warped template after registration using homogeneous/inhomogeneous elasticity. The grid (blue) illustrates the displacements.

On a discrete grid, the technique is to first discretize $\mathcal{A}_T$ and f_{CV} using finite differences. Next, we generate a sparse convolution matrix A_T that corresponds to the operator $\mathcal{A}_T$ after discretization, such that (3.14) reads

$$A_T \underline{u}^{(k)} = \underline{f}_{CV}^{(k-1)} \; , \tag{3.15}$$

where $\underline{f}_{CV}$ and $\underline{u}$ are column vectors that contain samples of the forces and (unknown) displacements on the discrete grid, respectively. The samples are ordered lexicographically by stacking the voxels of each component on top of one other to form one large column. Zero boundary conditions are assumed to compute the convolution matrix.

3.3.4 Synthetic Example

The proposed method is illustrated on a synthetic example in 2-D. Here, two binary images are being registered. The template is an ellipse with intensity values of “1” assigned to its inside and “0” outside. The reference is a similar but dented ellipse, of which the contour is used as the model.

In Figure 3.2(a), the reference contour is overlaid on the initial template image. First, homogeneous elasticity was assigned to the template. Figure 3.2(b) shows the final warped template (after 50 iterations). Notice the symmetry of the warped grid around the horizontal axis. In the second example, the bottom half of the template was assigned three times stiffer elasticity values. Figure 3.2(c) shows the final warped template in this case. As expected, the displacements are larger in the top half of the image.

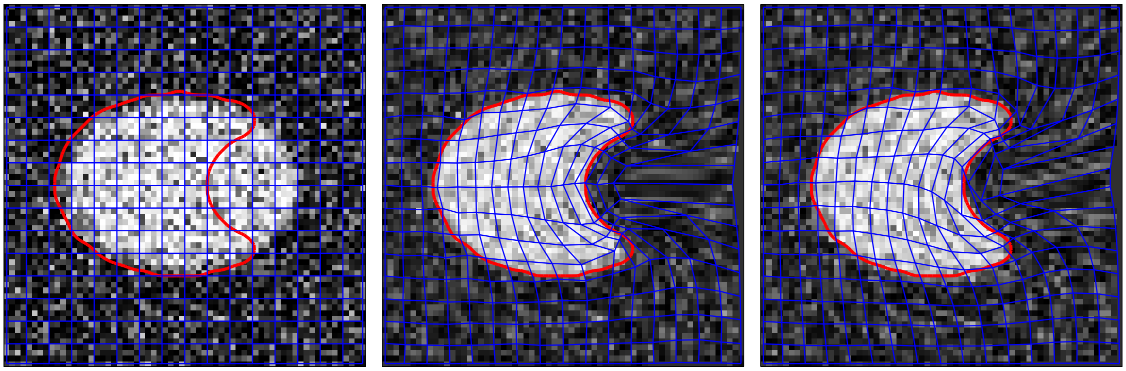

(a) Initial (b) Final (homogeneous) (c) Final (inhomogeneous)

Figure 3.3: Registration of noisy synthetic images. The reference contour (red) is overlaid on (a) the initial binary template with a Gaussian noise of 0.25 STDV, and (b)-(c) the warped template after registration using homogeneous/inhomogeneous elasticity. The grid (blue) illustrates the displacements.

Due to the employed region-based force, which takes into account region statistics rather than specific pixel values, the method is robust to noise. In Figure 3.3 we see the same registration examples as before, but with a zero mean Gaussian noise added to the binary template image. The corresponding results (after 100 iterations) are shown in Figures 3.3(a)-(c). Indeed, the results are very similar to the noiseless experiments (a slight grid asymmetry can be noticed in Figure 3.3(b)).

In order to quantify the robustness to noise, we repeat the experiments for a Gaussian noise with different values of STDV. We evaluate both robustness to intensity variations, by adding the noise to the template, and robustness to elasticity variations, by adding the noise to the elasticity map. The resulting pixels' displacement map for each noisy registration is compared to the noiseless registration map. Figure 3.4 plots the mean Euclidean norm (over all pixels) of the difference between the displacement maps against the corresponding STDV values of the noise.

The intensity noise and elasticity noise affect the results to a small extent (less than one pixel of error on average), up to STDV values of 0.1 (10% of noiseless intensity and elasticity). We see that intensity noise causes a constant error in the displacement. This is mostly due to small displacement errors in the background, and not due to errors in the large displacements around the object. The elasticity noise however, causes a logarithmic increase of the error. This is due to violation of the "slow" varying assumption in the approximation of the Navier-Cauchy equation, (3.13).

For STDVs above 0.1, the error caused by intensity noise increases, while elasticity

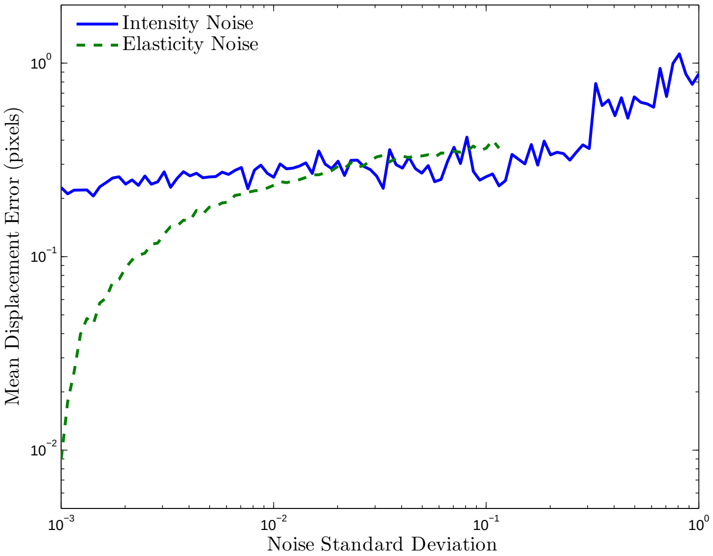

Figure 3.4: Robustness to noise. The error is the mean Euclidean distance between the displacement maps resulting from noiseless and noisy registration of synthetic images, as seen in Figures 3.2 and 3.3. The STDV of the noise represents the (inverse) SNR with respect to the ellipse (intensity and elasticity values of “1”).

noise yields convolution matrices A_T that are singular (to working precision), due to pixels with (almost) zero elasticity, causing the algorithm to fail. We also found a logarithmic relationship between the noise and the required number of iterations for convergence.

3.3.5 Clinical Example

Here, we describe the utilization of the proposed method for registration between an *ex vivo* model and the *in vivo* MRI volume and demonstrate the process on clinical data. As a preprocessing step, we translate the *ex vivo* model to match its center with the center of the *in vivo* volume. Next, we employ the model-based approach described in Section 3.2.3 for fine alignment with respect to translations, scaling and rotations. Finally, we compute the residual nonrigid map between the aligned model and the image using the proposed model-based registration with inhomogeneous elasticity.

The registration process is illustrated in Figure 3.5. Note that in Figure 3.5(c), the template image is warped to fit the prostate inside the reference model. The inverse map is then applied to the rigidly aligned model in order to produce the registered *ex vivo* model on the coordinate system of the *in vivo* image, as seen in Figure 3.5(d).

We note that in [163], the authors transformed the T2w images by applying the gradient

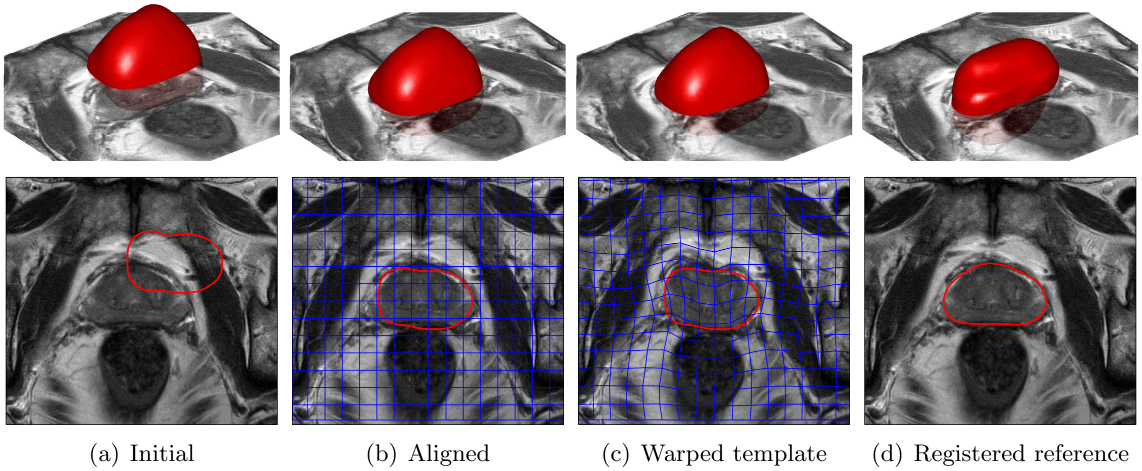
(a) Initial (b) Aligned (c) Warped template (d) Registered reference

Figure 3.5: Registration process. (a) The initial *ex vivo* reference model (red) is overlaid on a slice of the *in vivo* T2w template image. (b) Translated, rotated and scaled model after using the model-based alignment. (c) Warped template after using the proposed model-based elastic registration. (d) Registered model after applying the inverse map. A 3-D view (top row) of the model, and a 2-D cross-section (bottom row) are shown.

operator in order to increase intensity homogeneity inside the prostate and accentuate its boundaries for their region-based segmentation to work. In our case, we found the registration to perform better on the MRE magnitude images (see Section 3.5.1), and superimposed the results on the T2w images.

3.4 Elastic Homogeneity Versus Inhomogeneity

In this section we provide analysis to show that inhomogeneous elasticity improves the registration performance. In order to do so, we degenerate the MRE measured elastogram, E_T, by employing the k-means clustering algorithm [33] with different values of k's.

The feature space to be clustered comprises the elasticity value, with the addition of the spatial coordinates $\bar{r}$, in order to create geometrically connected clusters. The "points" to be clustered are therefore the feature vectors generated for each voxel. A clustered elastogram $E_{T,k}$ is created by applying the elasticity value of the centroid to each voxel in the corresponding cluster.

The extreme case of $k = 1$ yields a homogeneous elastogram, $E_{T,1} = const$, in which the intensity is the mean elasticity value. The other extreme, which we denote by $k \to \infty$, yields the original inhomogeneous elastogram, $E_{T,\infty} = E_T$. We therefore refer to k as the inhomogeneity parameter.

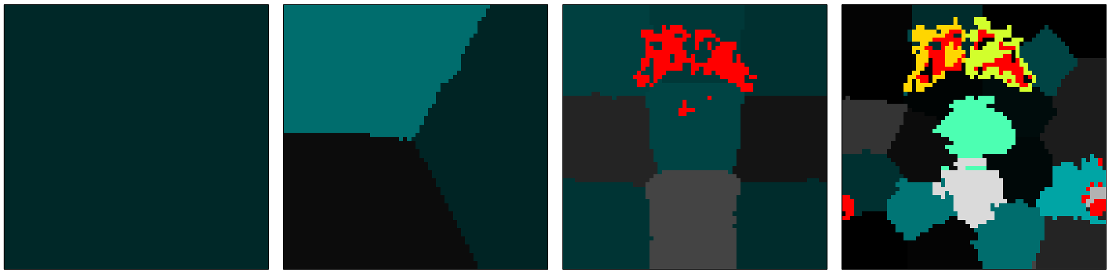

(a) $E_{T,1}$ (homogeneous) (b) $E_{T,3}$ (c) $E_{T,10}$ (d) $E_{T,50}$

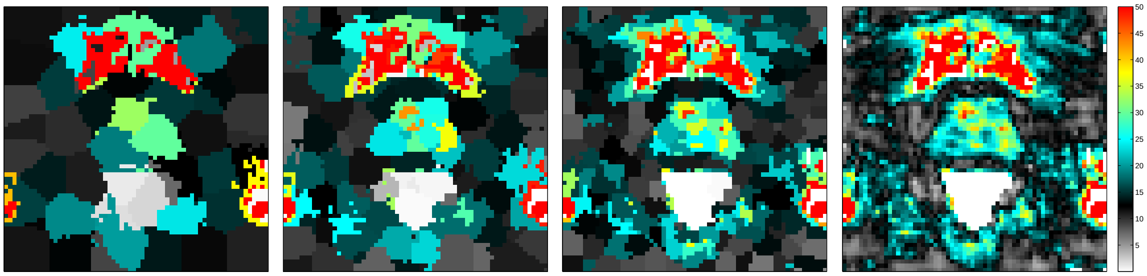

(e) $E_{T,100}$ (f) $E_{T,250}$ (g) $E_{T,1000}$ (h) $E_{T,\infty}$ (total inhomogeneous)

Figure 3.6: Elastograms for different values of the inhomogeneity parameter. Intensity scale is in kPa.

In fact, any value $k \geq N$, where N is the total number of voxels, and, in practice, due to repetitions in the quantized data, even lower k's, yield the same clustering as $k \to \infty$. Figure 3.6 depicts a mid-gland slice of the elastograms, which correspond to the example case in Figure 3.5, for selected values of the inhomogeneity parameter in the range between homogeneity and total inhomogeneity.

We repeatedly perform the registration described in Section 3.3.5 for different values of the inhomogeneity parameter, with respect to the resulting clustered elastogram. We run each registration until convergence to the same energy value that we have achieved in the original experiment. Therefore, the resulting warped templates look similar to each other and to the result in Figure 3.5(c). However, as expected, the displacements that map each of the templates are different.

Figure 3.7 shows the Euclidean norms of the displacement difference between the resulting maps that correspond to the inhomogeneity parameter values shown before. Specifically, Figure 3.7(h) shows the difference between the total inhomogeneous and homogeneous registration maps on the mid-gland slice, and we may notice a difference of ~ 3.5 mm inside the prostate region.

The performance is evaluated for each registration through the volume overlap, in the

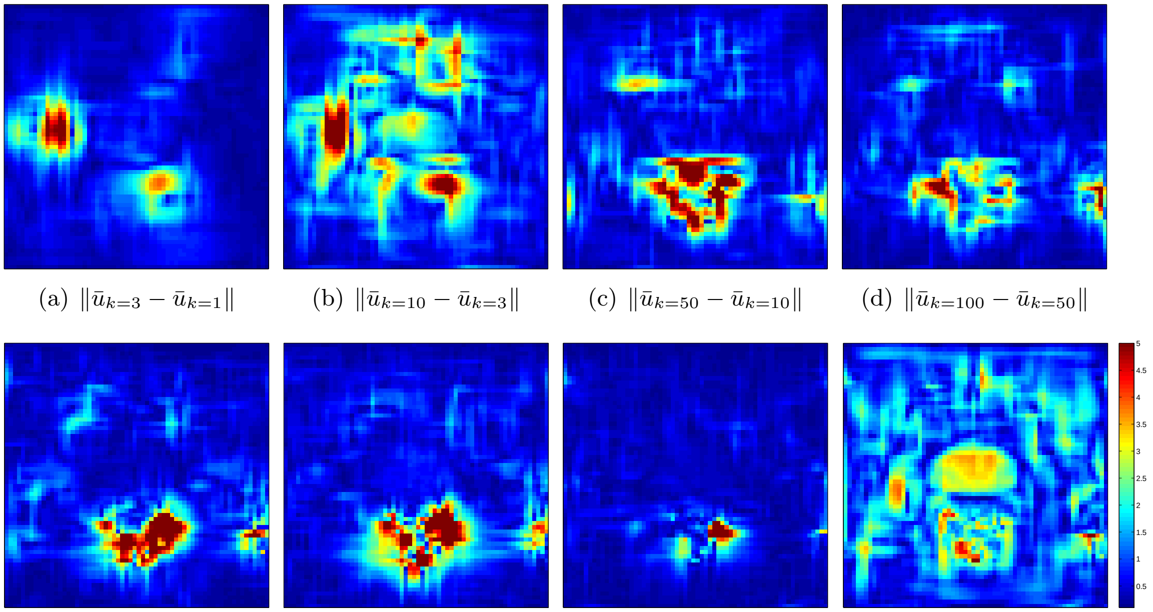

(a) $\|\bar{u}_{k=3} - \bar{u}_{k=1}\|$ (b) $\|\bar{u}_{k=10} - \bar{u}_{k=3}\|$ (c) $\|\bar{u}_{k=50} - \bar{u}_{k=10}\|$ (d) $\|\bar{u}_{k=100} - \bar{u}_{k=50}\|$

(e) $\|\bar{u}_{k=250} - \bar{u}_{k=100}\|$ (f) $\|\bar{u}_{k=1000} - \bar{u}_{k=250}\|$ (g) $\|\bar{u}_{k\to\infty} - \bar{u}_{k=1000}\|$ (h) $\|\bar{u}_{k\to\infty} - \bar{u}_{k=1}\|$

Figure 3.7: Euclidean distance of the displacement maps resulting from registrations using different values of the inhomogeneity parameter. Intensity scale is in mm.

sense of Dice's coefficient (3.16), between the registered *ex vivo* model and a manually segmented *in vivo* model, and through the distance between manually selected landmarks on the two modalities (see Section 3.5.3). Figure 3.8 shows these measures for different values of the inhomogeneity parameter.

Indeed, we identify the general trends that the volume overlap and the landmark error are, respectively, in direct and inverse proportion with the inhomogeneity parameter. We therefore conclude that performance improves when an inhomogeneous model is used. We note, however, that for two cases, the maximum volume overlap and minimum error were attained at $k = 250$ and $k = 500$ rather than $k \to \infty$. The reason for that is the noisy nature of the inhomogeneous elastogram that violates the "slow" varying assumption, as discussed in Section 3.3.4.

Thus, setting a value for k that is too small leads to elastic homogeneity, while setting its value too high may lead to inaccurate regularization. In our experiments we take $k = 250$, since for greater values, when applicable, the improvement is not significant.

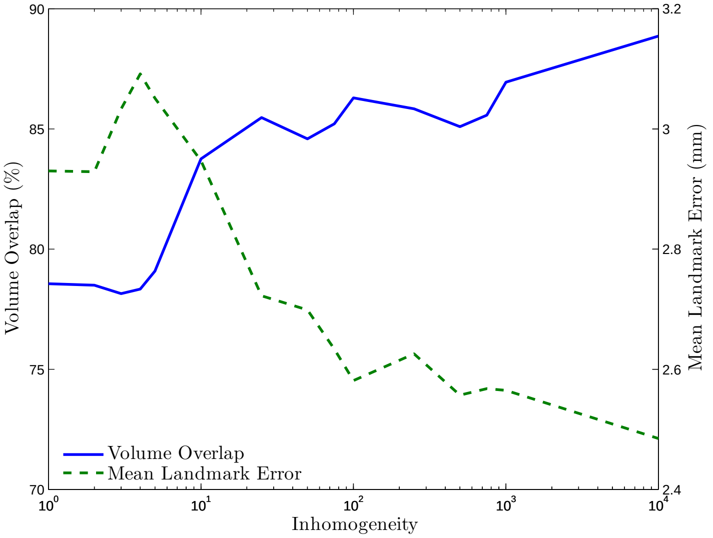

Figure 3.8: Registration performance for different values of the inhomogeneity parameter.

3.5 Experiments

In this section we describe the acquisition of the data sets that were used in our study. We provide details on the imaging protocol, as well as on the implementation of the registration algorithm, its execution time and evaluation. Finally, we summarize the results of the registration experiments.

3.5.1 Data Acquisition

In Vivo Scan

After approval of the institutional ethics board and signed consents, six patients (mean age 65, range 59–76 years old) who were scheduled for radical prostatectomy, underwent a preoperative *in vivo* T2w scan followed by MRE scan in a 3-Tesla system (Achieva 3.0T, Philips, The Netherlands). A standard 6-channel cardiac coil with acceleration factor (SENSE) of 2 was used.

First, a sagittal scout image was acquired to ensure that the transperineal MRE driver is properly positioned at the beginning of the examination, as illustrated in Figure 1.3(a). Then, a standard axial T2w FSE sequence was acquired (TE/TR = 86/2500 ms, FOV $= 320 \times 320 \times 70$ mm^3, with 0.5 mm in-plane resolution and 2 mm slice thickness).

Next, a transperineal prostate MRE scan was acquired using a gradient echo sequence named eXpresso [136]. Eight phases were encoded with a mechanical excitation of 70 Hz

	Min–max inside	Mean inside	Min–max outside	Mean outside
Case 1	4.8 – 50.3	19.5 ± 9.8	1.6 – 75.3	13.1 ± 6.0
Case 2	3.0 – 36.6	17.7 ± 5.3	1.4 – 79.6	11.1 ± 5.2
Case 3	2.0 – 38.0	13.7 ± 6.8	1.0 – 36.4	8.5 ± 4.5
Case 4	1.6 – 26.0	11.6 ± 3.6	1.3 – 53.1	9.7 ± 5.3
Case 5	6.6 – 37.0	21.0 ± 6.7	1.9 – 79.2	15.8 ± 9.0
Case 6	10.3 – 50.8	24.0 ± 6.5	2.8 – 54.5	15.0 ± 8.2

Table 3.1: MRE results. Quantitative summary of elasticity inside and outside the prostate. Values are in kPa.

applied to the perineum of the patient [134]. Wave images were acquired on a $128 \times 128 \times 24$ matrix with 2 mm isotropic voxel size. Figure 1.3(d)-(f) shows an example slice of these wave images. The entire MRE scan lasted about 8 min for a 3-D displacement field acquisition. Each slice was cropped to accommodate 64×64 pixels around the prostate region for computational efficiency, and then processed offline to generate an elastogram similarly to the approach described in [150].

The quantitative elasticity values that were obtained are summarized in Table 3.1. The range and mean elasticity were computed over the regions inside and outside (excluding the pubic bone) of the prostate boundary (manually chosen by an expert for the registration evaluation). The results demonstrate the inhomogeneity in elasticity and the fact that, in general, the prostate is stiffer (higher values) than its surrounding tissue. For other reported elasticity values of the prostate, see [134] and references therein.

In addition to the elastogram, an image was generated from the magnitude component of the MRE signal. This image, referred to as the magnitude image, is intrinsically aligned with the elastogram and provides complementary intensity information. An example slice of the magnitude image in Figure 1.3(c) shows the intensity homogeneity inside the prostate, which is ideal for a region-based algorithm to be employed on. The scanning geometry, as given in the scanner output, determines the alignment of both the elastogram and the magnitude image with the T2w volume.

Ex Vivo Scan

The postoperative *ex vivo* prostate specimen was fixed in 10% buffered formalin, typically for 72 hours. It was then wrapped in a plastic bag, taped to a dedicated holder and scanned in a 7-Tesla system (Biospec, Bruker, Germany).

A rapid acquisition with relaxation enhancement (RARE) pulse sequence was used to acquire axial T2w images (TE/TR = 70/5000 ms, FOV = 70 × 70 × 42 mm^3, with 0.2734 mm in-plane resolution and 2 mm slice thickness).

To extract the *ex vivo* model, the images were semi-automatically segmented by employing the region-based active contours algorithm described in Section 3.2.2, with manual corrections by a radiologist that were required mainly due to artifacts caused by imaging of the wrapping bag around the specimen. We have then used Stradwin (Cambridge University, U.K.) [160], which employs [161], in order to generate a surface from the segmented *ex vivo* slices. We set the surface resolution and smoothing strength to "medium."

3.5.2 Implementation Details

We have implemented our registration method and tested it under MATLAB on a 2.93 GHz Quad Core CPU machine with 8 GB of RAM. It typically takes 100 iterations of rigid registration, and additional 100 iterations of nonrigid registration to reach convergence of the energy. The bottleneck of the algorithm is solving (3.15) for the displacement values. It involves finding $3 \times N$ unknowns in each iteration, where N is the total number of voxels. This is usually a large number and makes the algorithm computationally expensive.

In general, the inhomogeneity of the Lamé parameters yields sparse, but non-symmetric and non-periodic convolution matrices A_T, which do not allow numerical schemes to take advantage of their structure, e.g., as in [40] where the authors employ the fast Fourier transform (FFT) for fast inversion. Thus, an approximate solution of the problem is found by employing the biconjugate gradient method [123] for a fixed number of iterations, while keeping execution times within reason. We found 50 iterations to provide plausible results, which resulted in a total execution time of about 12 min for registering $64 \times 64 \times 24$ volumes on an un-optimized code.

3.5.3 Results

To evaluate the registration performance, we compare the final registered *ex vivo* model to an *in vivo* prostate model that was segmented manually by an expert on the T2w slices. As a general performance indicator, we measure VO, the volume overlap between the registered and manual 3-D models in the sense of Dice's coefficient, i.e., twice the size of the intersected volume divided by the sum of the sizes of the volumes. In the level set method, this can be formulated as

$$VO = \frac{2\int_{\mathcal{D}} \mathcal{H}(-\tilde{\Phi}_R)\mathcal{H}(-\Phi_T)\,d\bar{r}}{\int_{\mathcal{D}} \Big(\mathcal{H}(-\tilde{\Phi}_R) + \mathcal{H}(-\Phi_T)\Big)\,d\bar{r}}, \tag{3.16}$$

where $\tilde{\Phi}_R$ and Φ_T are the level set functions embedding the registered (warped) model and the manual model, respectively. Similarly, in order to evaluate the performance at different regions of the prostate, we measure AO, which is the area overlap between cross-sections of the registered and manual models on slices from the base, mid-gland, and apex regions of the gland.

In addition, the expert has identified matching landmarks inside the prostate region on both the *ex vivo* and *in vivo* images. We measure the Euclidean distance between the registered *ex vivo* landmarks and their *in vivo* counterparts. Since our goal is to register (unknown) cancerous regions inside the prostate, these distances between landmarks provide us a good approximation of the target registration error (TRE).

Finally, in order to evaluate the improvement that was achieved by employing MRE, we repeated the experiments for all cases after assigning the voxels a homogeneous elasticity value that is equal to the mean elasticity value inside the prostate (the elastogram region inside the expert's manual segmentation). Note that this experiment is different than the simulation with $k = 1$ in Section 3.4, where the mean elasticity of the entire field of view was used, and is expected to perform better since the elasticity inside the prostate is more relevant. We compare these homogeneous registration results to the inhomogeneous registration results.

Figure 3.9 visualizes the inhomogeneous registration results. In Figure 3.9(a), the surfaces of the registered and manual models of each case are shown in 3-D, together with the registered and manual landmarks. Figures 3.9(b)-(d) show cross-sections of the registered and manual models overlaid on selected slices from the base, mid-gland and apex regions of the prostate, respectively. Quantitative and statistical summaries of the registration results are presented in Table 3.2 and Figure 3.10, respectively.

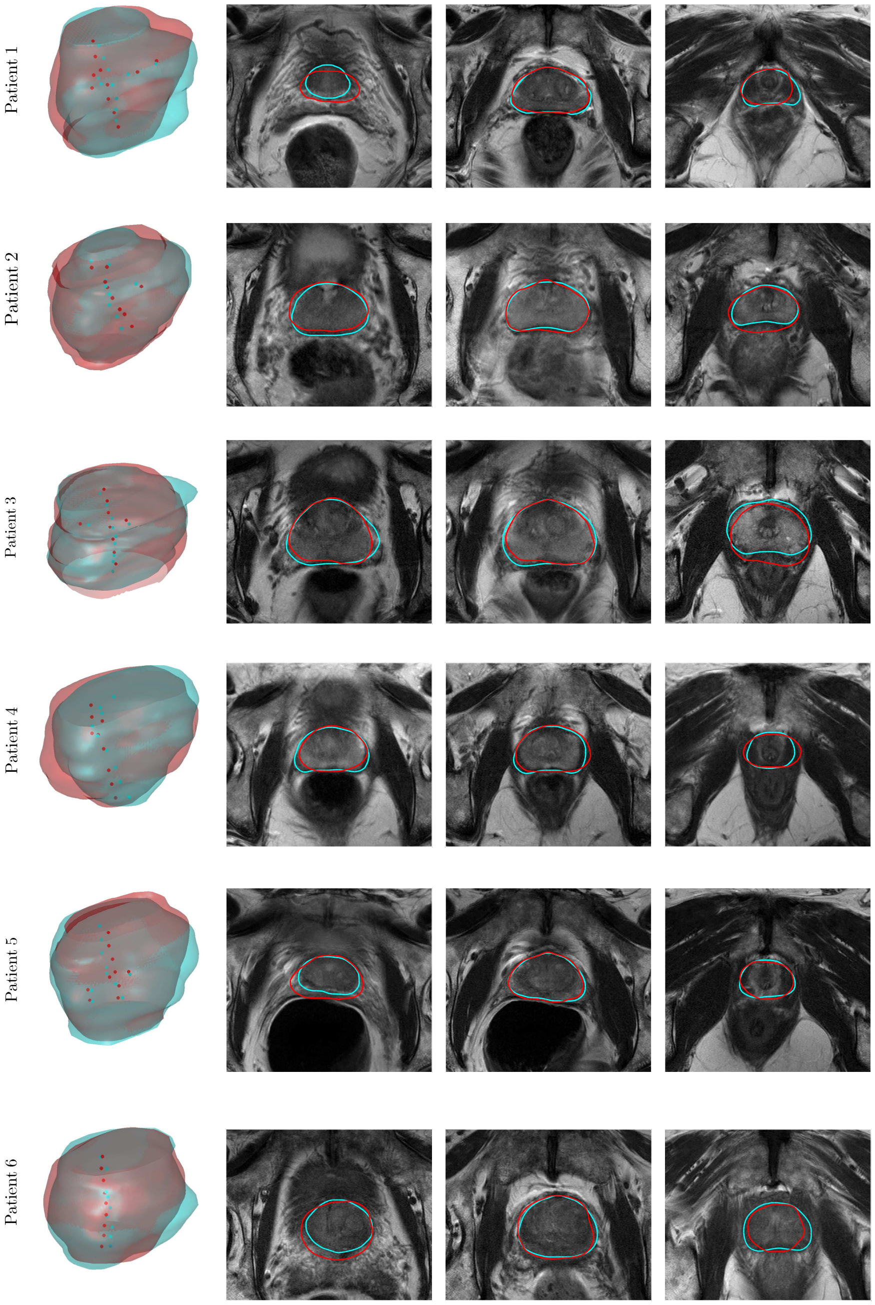
Patient 1
Patient 2
Patient 3
Patient 4
Patient 5
Patient 6

(a) 3-D (b) Base (c) Mid-gland (d) Apex

Figure 3.9: Inhomogeneous registration results. The registered *ex vivo* reference model (red) and a manually segmented model (cyan) of the *in vivo* T2w template image. Spheres in column (a) represent registered and manually marked landmarks. Columns (b)-(d) show cross-sections of the models overlaid on selected T2w slices from the base, mid-gland and apex regions of the prostate.

	Inhomogeneous Elasticity					Homogeneous Elasticity	
	Base AO (%)	Mid-gland AO (%)	Apex AO (%)	VO (%)	Error (mm)	VO (%)	Error (mm)
Case 1	77.7 ± 4.5	91.0 ± 2.3	88.3 ± 0.8	87.5	2.5 ± 0.8	85.3	3.1 ± 1.1
Case 2	76.6 ± 10.9	92.4 ± 2.6	78.1 ± 7.8	85.9	1.5 ± 0.6	84.0	2.8 ± 0.7
Case 3	90.3 ± 0.6	92.1 ± 3.0	78.9 ± 2.4	87.3	3.2 ± 1.0	82.9	3.1 ± 0.8
Case 4	83.5 ± 6.0	83.5 ± 4.7	76.0 ± 2.9	81.6	4.3 ± 2.5	76.9	5.2 ± 3.6
Case 5	90.0 ± 4.9	93.5 ± 2.5	89.9 ± 1.0	88.1	2.3 ± 1.3	84.1	2.5 ± 1.2
Case 6	85.7 ± 2.3	91.2 ± 2.4	79.4 ± 9.3	86.9	4.1 ± 1.4	82.9	5.5 ± 2.3
Mean	83.4 ± 7.7	90.8 ± 4.0	81.8 ± 7.1	86.2 ± 2.4	3.1 ± 1.4	82.7 ± 3.0	3.72 ± 1.9

Table 3.2: Registration results. Quantitative summary.

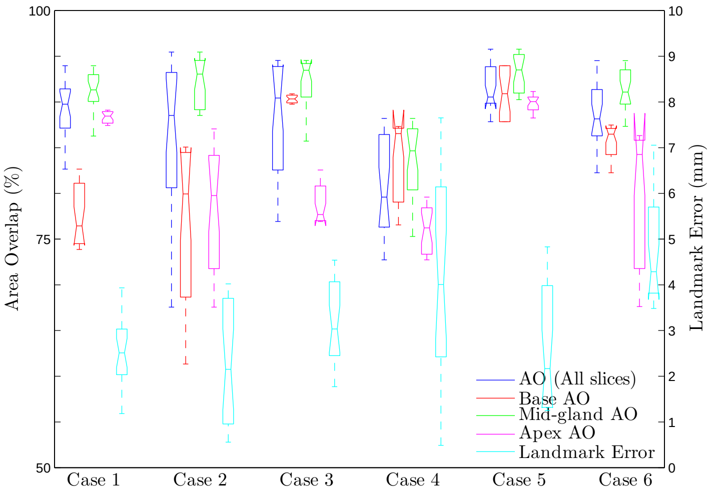

Figure 3.10: Inhomogeneous registration results. Statistical summary of the resulting area overlap (AO) among slices, and the landmark error.

3.6 Discussion and Conclusion

We have presented a method for an automatic model-based registration of *ex vivo* and *in vivo* prostate MRI. The method can be fused with established methods that consider registration of *ex vivo* MRI and histological sections, in order to recover the spatial correspondence between histopathology and the *in vivo* scan. Since histopathology of the prostate provides the ground truth cancerous and noncancerous regions, a correct mapping of these regions onto an MRI volume allows characterization of CaP on co-registered multi-parametric MRI, and may provide training and validation sets for a classifier that produces cancer probability maps on preoperative images. Typical training sets may include 10-20 cases, and validation sets may include 50-100 cases. Focusing on regions with high probability of cancer could impact treatments such as brachytherapy and radical prostatectomy, and reduce possible side effects such as impotence and urinary incontinence.

The proposed method aligns a model of the prostate, constructed from the *ex vivo* MRI, onto the *in vivo* volume, and then warps the *in vivo* volume so as to fit the aligned model. A variational approach has been used to derive the registration algorithm using a region-based active contour model in a level set formulation. The method was first demonstrated on synthetic images to evaluate its robustness to noise in the data, and was further tested and evaluated on six clinical cases by comparing the registered *ex vivo* model to manual segmentations of the *in vivo* volume, and by computing the distances between registered landmarks on the two modalities.

Our approach employs an MRE scan that allows measurement and assignment of elastic properties of the tissue to corresponding voxels in the image. In turn, this provides an implicit modeling of the prostate and its surrounding anatomical structures that allows warping the *in vivo* volumetric image onto the *ex vivo* model in a physical manner. Moreover, we found the MRE magnitude image to be an excellent candidate for the region-based approach due to its intensity homogeneity within the prostate.

While the most valuable information is pertaining to the prostate itself, utilizing the elasticity of both the prostate and its surrounding tissue is more likely to result in a mapping that portrays the actual displacement of the voxels within the prostate. This is attributable to the fact that most deformation occurs *in vivo* (*ex vivo* deformation is typically manifested as shrinkage and corrected by scaling), and is therefore governed by the *in vivo* elasticity and interaction of the prostate with its surrounding anatomy. Indeed, we have showed that this approach yields improved registration as opposed to applying a constant elasticity value to the volume, and that, in general, the performance improves with the inhomogeneity of elasticity inside and outside of the prostate. To the best of our knowledge, no such study has been conducted thus far. We note that an *ex vivo* measurement of the elasticity, although might be technically simpler, reflects the much stiffer elasticity of the post-fixation specimen which is irrelevant to the deformation.

In addition, our approach does not require segmentation and meshing of the *in vivo* anatomy, as opposed to explicit FEM-based modeling approaches. Although, as discussed above, the designated application of classification requires a limited number of cases, segmentation and meshing can still consume a significant amount of time. On the other hand, MRE is fast and easily integrated into the *in vivo* MRI protocol. Even in case that FEM is to be employed instead of our approach, MRE could benefit the chosen algorithm by providing the model with patient-specific elasticity.

The performance of the registration, and the significance of its improvement using MRE, should be evaluated with respect to the designated application. The mean registration error that was achieved during the experiments is within the tumor diameter that MRI is reported to detect and characterize CaP [71], and within the size of most clinically significant lesions that are marked during histopathology analysis ($\sim 10 \pm 5$ mm [34]). Thus, in our case, the method is suitable for mapping of these tumors on the *in vivo* MRI. However, the registration might not be accurate enough to characterize early stage tumors that are considered in, e.g., training a classifier for an image guided biopsy application. Since MRE depends on fairly complex modulus reconstruction, we expect the registration results to improve with the developments in our reconstruction methods.

As other registration techniques, the proposed algorithm performs better on the mid-gland region of the prostate. This finding is due to the ambiguity in contouring the prostate around the base and apex on the *ex vivo* and *in vivo* images, that impacts the fidelity of both the model and evaluation in these regions. In future work, we may utilize the intensity similarity between *in vivo* and *ex vivo* T2w MRI to derive forces from intensity-based distance measures, e.g., MI. This may eliminate the required segmentation of the *ex vivo* volume, and improve speed and accuracy.

A disadvantage of the proposed approach is that the *ex vivo* MRI scan is time consuming, expensive and not accessible. However, as discussed above, the proposed method should be employed on a limited number of cases for the designated application. Moreover, as discussed in Section 3.1, methods that propose direct registration between *in vivo* MRI to histopathology require either dense sectioning of histological slices [111], or manual selection of corresponding slices [24]. Another direct approach, proposed in [148] and [162], generates a patient-specific mold, based on the (non-deformed) *in vivo* prostate, to preserve sectioning orientation. Thus, current direct registration methods can be just as time consuming as the *ex vivo* scan, while being more user-dependent and error-prone.

We note, however, that since the *ex vivo* scan in our approach is used only to acquire a model of the specimen, a direct registration to histopathology is still possible using our method by using a 3-D model reconstruction based on the histological slices, provided that their sectioning is dense enough. In addition, other *ex vivo* imaging modalities, which are more accessible than MRI, can be employed. In fact, an US generated *ex vivo* model may be combined with methods such as [158] to register the *ex vivo* scan to histology following our method. Thus, our framework is general and can be fitted into different workflows.

The current implementation does not allow real-time performance, which is not a requirement in the case of cancer characterization. The execution times are in the order of minutes, so multiple registrations can be processed on the background in a typical clinical scenario to provide a reasonable throughput. Another current limitation is the assumption of small deformations. Although the residual deformations are small after a similarity transformation, we may still consider nonlinear elasticity for future work in order to contend with large deformations of the prostate, e.g., in case of employing a transrectal coil during image acquisition.

Chapter 4

Registration of Ultrasound and Magnetic Resonance Imaging for Image Guided Interventions

4.1 Introduction

Intraoperative TRUS imaging has been shown to be valuable during CaP interventions such as RALP [80], but is of poor quality and not reliable for detecting cancer. The ability of multi-parametric MRI to generate the most accurate characterization of CaP [75], has led to the development of methods for MRI-guided treatment, mainly biopsy and brachytherapy [159]. Indeed, a systematic literature review in [97] suggests that MRI-guided biopsy detects clinically significant CaP using fewer samples compared to a standard biopsy that employs TRUS alone.

While direct MRI-guided methods have been reported, e.g., in [153], for prostate biopsy and brachytherapy, intraoperative MRI is still cumbersome, time consuming, resource costly and not widely used. Cognitive fusion, in which the clinician estimates the lesion's location on the intraoperative TRUS based on a preoperative MRI, varies greatly with expertise. A more feasible approach to allow integration of MRI data in the operating room involves registration of the preoperative MRI to the intraoperative TRUS, and visualization of the corresponding images to assist the clinician during treatment. Previously, such an approach was successfully demonstrated, e.g., in [51, 86, 91, 120, 149, 164], for prostate biopsy, and in [28, 126] for prostate brachytherapy.

Due to the difference in intensity information, contrast, and anatomical visualization presented by the two modalities, techniques for registration of MRI and TRUS typically involve preprocessing of the images. In [101, 157] both modalities are segmented and the surfaces are registered using deformable registration for targeted prostate biopsy. In [90], corresponding 2-D MRI and TRUS images are manually selected, segmented, and then registered by minimizing the Bhattacharyya distance between their shape representations, with thin-plate splines as regularization. In [59, 87], a patient-specific biomechanical model is generated from segmented T2w images, and a model-to-image deformable registration is performed based on features extracted from 3-D TRUS images. In [156], features are extracted by employing [55], and the distance between modality independent neighbourhood descriptors (MIND) is minimized with a smoothness regularization.

In this chapter, we propose to introduce MRI information during RALP. To this end, in the first part of this chapter, we propose a segmentation-based registration method that incorporates a semi-automatic prostate segmentation algorithm, developed in our lab, to segment a TRUS volume, acquired from an intraoperative sweep of the probe. A preoperative segmented MRI is then registered to the segmented intraoperative TRUS. The method can be incorporated with a tracking algorithm, developed in our lab as well, that allows the TRUS probe, that is mounted on a motorized system [143], to track the robot's tooltip. Corresponding TRUS and MRI planes that follow the tooltip may then be visualized in real-time on the surgeon console.

In the second part of this chapter, we propose to employ elastography for intensity-based registration of MRI and US. Elastograms have been shown to be promising in improving the visibility of the prostate gland [143]. The produced images typically have superior prostate-to-background contrast compared to T2-weighted images, especially at the base and apex. This is due to the fact that prostate tissue is generally stiffer than the surrounding tissue.

The challenges in employing elastography for image processing of the prostate are their low resolution (typically of MRE volumes) and poor signal-to-noise ratio. Also, the boundary of the prostate may be blurred and assimilated with the background at some regions. Nevertheless, previously in [83], the authors showed that fusion of region information from TRUS-VE images and edge information from B-mode images improved the performance of an active shape model for prostate segmentation. In [102], MRE is employed for prostate segmentation by using the elastogram and corresponding magnitude image for driving a region- and edge-based active contours, respectively. In Chapter 3, we described the utilization of elastography as a regularizer for prostate registration.

In our data collection, both MRE and USE images are acquired and should ideally represent the same tissue elasticity in the scanned anatomy. We investigate the use of the elasticity values in a similarity metric to drive the registration. Since the elastography volumes are inherently registered with their corresponding T2w and B-mode volumes, MRE-USE registration may serve as an inter-modality to facilitate such multimodality registration.

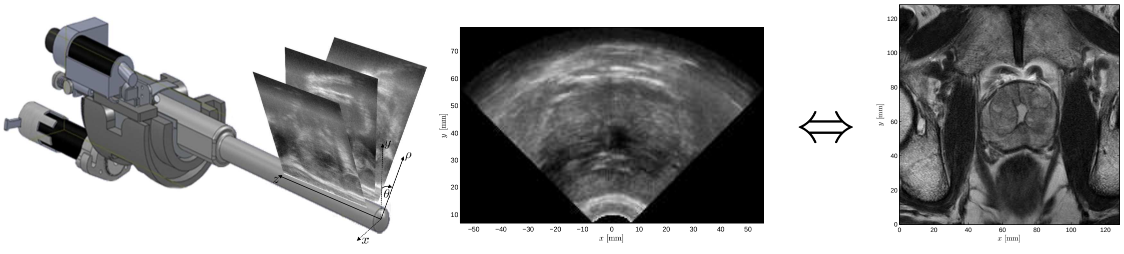

(a) $I_{\mathrm{US,SAG}}$ (b) $I_{\mathrm{US,TRV}}$ (c) $I_{\mathrm{MR,TRV}}$

Figure 4.1: Problem illustration. (a) Intraoperative sagittal B-mode images acquired by a sweep of the TRUS probe span a sector in cylindrical coordinates. (b) A transverse B-mode image after conversion to cartesian spatial coordinates. (c) A preoperative transverse T2w MR slice.

4.2 Problem Formulation

Suppose we are given $I_{\mathrm{US,SAG}}(\rho, \theta, z)$, the intraoperative B-mode volume spanned by sagittal images that are acquired by a sweep of a TRUS probe. The cylindrical coordinate vector is denoted by $(\rho, \theta, z)^T$, with $\rho \in [\rho_0, \rho_1]$ as the radial distance from the center of the probe (ρ_0 is the probe's radius), $\theta \in [\theta_0, \theta_1]$ as the probe's angle, and $z \in [0, z_1]$ as the axial coordinate on the sensor. We can then use the following conversion to obtain the corresponding transverse TRUS volume

$$I_{\mathrm{US,TRV}}(\bar{r}) = I_{\mathrm{US,SAG}}(x^2 + y^2, \arctan 2(y, x) - \frac{\pi}{2}, z), \tag{4.1}$$

where $\bar{r} = (x, y, z)^T \in \mathbb{R}^3$ denotes the 3-D cartesian spatial coordinate vector, with its origin at the probe's center. Figure 4.1 illustrates the TRUS B-mode volumes.

Suppose we are also given $I_{\mathrm{MR,TRV}}(\bar{r})$, the preoperative T2w MR volume in cartesian coordinates. We are interested in a displacement field $\bar{u} = (u_x, u_y, u_z)^T$, such that the deformed transverse MR volume,

$$\tilde{I}_{\mathrm{MR,TRV}}(\bar{r}; \bar{u}) = I_{\mathrm{MR,TRV}}(\bar{r} - \bar{u}(\bar{r})), \tag{4.2}$$

is similar, in some sense, to the transverse TRUS, volume $I_{\mathrm{US,TRV}}$. Similar to Chapter 3, the registration problem is formulated as the minimization of the energy,

$$\mathcal{J}[\bar{u}; I_{\mathrm{US,TRV}}, I_{\mathrm{MR,TRV}}] = \mathcal{F}[I_{\mathrm{US,TRV}}, \tilde{I}_{\mathrm{MR,TRV}}(\cdot; \bar{u})] + \mathcal{S}[\bar{u}] \;, \tag{4.3}$$

where $\mathcal{F}$ and $\mathcal{S}$ are the similarity metric and regularization functionals, respectively.

We can then use the following conversion to obtain the corresponding registered sagittal MR volume

$$\tilde{I}_{\text{MR,SAG}}(\rho, \theta, z) = \tilde{I}_{\text{MR,TRV}}(-\rho \sin(\theta), \rho \cos(\theta), z), \tag{4.4}$$

in order to visualize the TRUS and MR volumes together.

4.3 Segmentation-Based Registration

Typically, as part of a volume study, the prostate gland on each transverse slice in the preoperative T2w MR volume is segmented manually by an expert before surgery. In addition, we employ a real-time semi-automatic algorithm for 3-D segmentation of the prostate on the intraoperative TRUS B-mode. The algorithm, described in details in [142], has been routinely employed during brachytherapy, and found to be a fast, consistent and accurate tool for the delineation of the prostate gland in TRUS images. Below, we provide a short summary of the method.

4.3.1 Semi-Automatic Prostate Segmentation in TRUS

The user interaction part of the algorithm is required for initialization and comprising two steps. In the first step, the user selects two points that correspond to the base and apex of the prostate on a sagittal image. This selection of base and apex set the center as mid-gland plane, on which the prostate is the largest and most visible.

The second step is to select seven key geometrical points on a transverse image from the mid-gland. These points consist of the center of the TRUS probe, four points on the prostate's boundary – the lowest posterior lateral, extreme right, mid-posterior, mid-anterior, and two points that intersect the boundary with perpendicular lines that connects the extreme right point with the lowest posterior lateral and mid-anterior points. These steps of the algorithm and the resulting segmentation contour on the mid-gland image are depicted in Figure 4.2.

After user initialization, the 3-D segmentation is performed automatically. The algorithm un-warps the mid-gland image to reduce the deformation caused by the probe, then uses a tapered ellipse, fitted to the selected points, to guide an edge detector algorithm, [1] that evolves the contour edge on each 2-D transverse image using an interacting multiple model estimator. The images are then un-tapered, and the contour estimations are corrected to allow for a tapered ellipsoid fitting for smoothness and continuity of the contours. Finally, the contours are tapered and warped to match the original images.

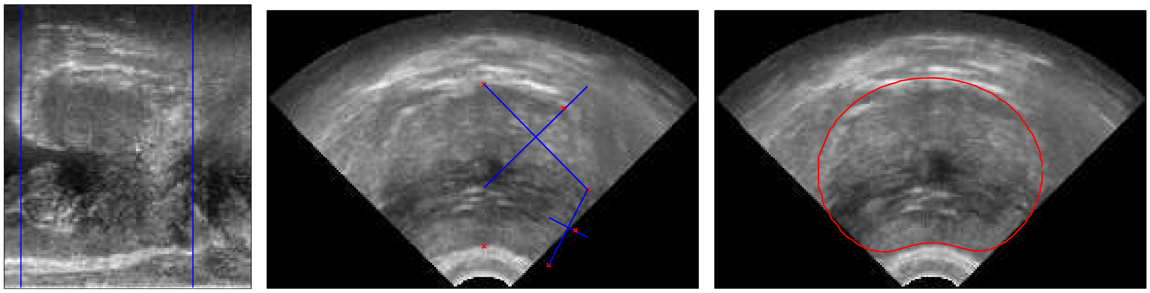
(a) Base-apex selection (b) Mid-gland points selection (c) Segmented slice

Figure 4.2: Semi-automatic segmentation. (a) The user selects the base and the apex on a sagittal image. (b) The user selects the center of the probe, and six boundary points on the transverse mid-gland image. (c) The resulting segmentation contour.

4.3.2 Registration Process

Based on the segmented surfaces of the prostate in the TRUS and MR volumes, we construct the binary volumes $H_{\mathrm{US,TRV}}$ and $H_{\mathrm{MR,TRV}}$, respectively, each with values of "1" on the region inside the prostate, and "0" outside. We may then register the two binary volumes and apply the resulting displacement map back to the MR volume $I_{\mathrm{MR,TRV}}$.

First, the two binary volumes are rigidly aligned (and scaled) using the principal axes transformation [4]. This is a fast, one-step registration that was found to provide a good initial alignment for the followed deformable registration. To this end, the binary volumes are treated as pdfs, and the corresponding "centers of mass", $\bar{m}_{\mathrm{US}}, \bar{m}_{\mathrm{MR}} \in \mathbb{R}^3$, and covariances $M_{\mathrm{US}}, M_{\mathrm{MR}} \in \mathbb{R}^{3\times3}$, are calculated as

$$\begin{aligned}\bar{m}_i &= \frac{\int \bar{r} H_{i,TRV}\, d\bar{r}}{\int H_{i,TRV}\, d\bar{r}}\\ M_i &= \frac{\int (\bar{r}-\bar{m}_i)(\bar{r}-\bar{m}_i)^T H_{i,TRV}\, d\bar{r}}{\int H_{i,TRV}\, d\bar{r}} = U_i \Sigma_i^2 U_i^T, \quad i = \mathrm{US}, \mathrm{MR}\end{aligned} \tag{4.5}$$

where $U_{\mathrm{US}}, \Sigma_{\mathrm{US}}$ and $U_{\mathrm{MR}}, \Sigma_{\mathrm{MR}} \in \mathbb{R}^{3\times3}$ are the eigendecomposition of the corresponding covariance matrices such that U_i is comprising the eigenvectors in its columns, and Σ_i containing the eigenvalues in its diagonal.

The aligned MR binary volume can be then computed using a linear coordinate transformation,

$$H^{\mathrm{rigid}}_{\mathrm{MR,TRV}}(\bar{r}) = H_{\mathrm{MR,TRV}}(A\bar{r}+b), \tag{4.6}$$

with $b = \bar{m}_{\mathrm{MR}} - A\bar{m}_{\mathrm{US}}$, and $A = U_{\mathrm{MR}}\Sigma_{\mathrm{MR}}\Sigma_{\mathrm{US}}^{-1}U_{\mathrm{US}}^T$.

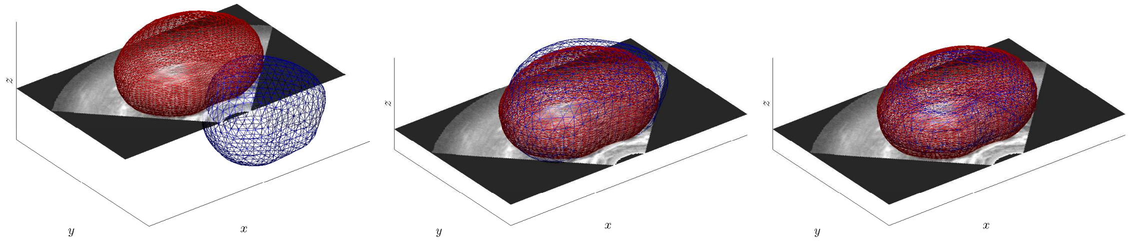

(a) Initial (b) Rigidly aligned (c) Registered

Figure 4.3: Segmentation-based registration. The surface of the segmented prostate on the TRUS (red) and MR (blue) volumes at different stages of the registration process.

Next, we apply (4.3) to the binary volumes, and minimize $\mathcal{J}[\bar{u}; H_{\text{US,TRV}}, H^{\text{rigid}}_{\text{MR,TRV}}]$. We take

$$\mathcal{F}[\bar{u}] = \int \left(H^{\text{rigid}}_{\text{MR,TRV}}(\bar{r} - \bar{u}(\bar{r})) - H_{\text{US,TRV}}(\bar{r}) \right)^2 d\bar{r} \; ,$$

$$\mathcal{S}[\bar{u}] = \int \left(\frac{\mu}{4} \sum_{j=1}^{3} \sum_{k=1}^{3} (\frac{\partial \bar{u}_j}{\partial \bar{r}_k} + \frac{\partial \bar{u}_k}{\partial \bar{r}_j})^2 + \frac{\lambda}{2} (\text{div } \bar{u})^2 \right) d\bar{r} \; , \tag{4.7}$$

i.e., the SSD metric, and an homogenous elastic regularizer (the Lamé parameters λ and μ are constant and set arbitrarily with an almost incompressible Poisson ratio $\nu = 0.499$). Similar to Chapter 3, we minimize (4.7) in a variational approach by computation of the corresponding Euler-Lagrange equation and its discretization (see also [92]). The proposed registration process is illustrated in Figure 4.3

4.3.3 Results

The proposed method was tested on six data sets of patients who were scheduled for radical prostatectomy and underwent preoperative MR and intraoperative US. The MR volumes were acquired by a 3-Tesla system (Achieva 3.0T, Philips, The Netherlands) using a standard 6-channel cardiac coil with acceleration factor (SENSE) 2. A standard axial T2w FSE sequence was acquired (TE/TR = 86/2500 ms, FOV = $320 \times 320 \times 70$ mm^3, with 0.5 mm in-plane resolution and 2 mm slice thickness).

The B-mode images were collected using an US machine (Sonix RP, Ultrasonix Medical, Richmond, BC, Canada) with a biplane transrectal probe (BPL9-5/55, 5–9 MHz, with radius $\rho_0 = 10$ mm) mounted on a motorized cradle [143]. A continuous sweep of sagittal

	Rigid registration		FEM method ([157])		Proposed method	
	VO (%)	Mean error (mm)	VO (%)	Mean error (mm)	VO (%)	Mean error (mm)
Case 1	85.8	1.39	95.7	1.19	97.3	1.57
Case 2	70.1	3.03	95.0	1.52	98.0	2.06
Case 3	75.1	1.67	94.6	0.87	97.6	1.11
Case 4	76.6	2.64	95.6	1.06	97.9	1.77
Case 5	72.9	2.73	94.3	1.41	98.0	1.10
Case 6	80.6	1.24	95.6	0.93	97.1	1.07
Mean	76.8 ± 5.1	2.11 ± 0.77	95.1 ± 0.5	1.16 ± 0.26	97.7 ± 0.3	1.44 ± 0.42

Table 4.1: Segmentation-based registration results.

images was acquired (radial distance $\rho_1 = 79$ mm, angular range $\theta_{0,1} = \pm\frac{\pi}{4}$, with 0.5 mm radial and axial resolution, and 0.2° angular resolution).

Both of the MR and TRUS transverse volumes were segmented using Stradwin (Cambridge University, UK), [160], and the surfaces of the prostate were generated with medium resolution and smoothing strength settings. The urethra on both modalities was segmented manually for evaluation as well. In order to maintain consistent processing times, we ran the deformable registration algorithm a fixed number of 30 iterations that takes about 184 sec, and was found to converge sufficiently. Including the times, as reported in [142], for manual selection of initialization points (32 ± 14 sec) and segmentation (14 ± 1 sec), the total runtime of the entire segmentation-based registration process is about 4 min.

We evaluated the registration performance using the volume overlap, in the sense of Dice's coefficient (3.16), between the MR and the TRUS volumes after rigid and deformable registration. The mean distance between splines on both modalities that were fitted through the center points of the urethra was also measured for the rigid and deformable registered volumes. In addition, our proposed variational approach was compared using the same evaluation metrics to a surface-based FEM registration approach proposed in [157]. The quantitative results are summarized in Table 4.1.

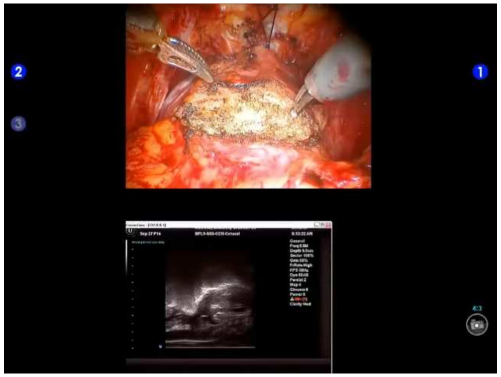

(a) Current console display

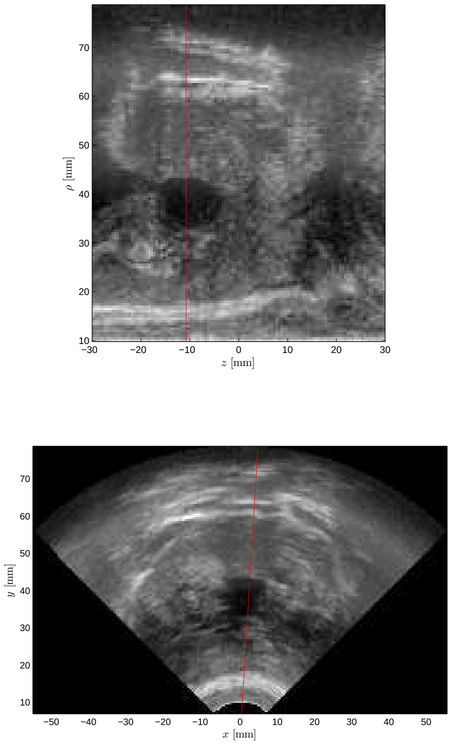
ρ [mm]
z [mm]
y [mm]
x [mm]
70
60
50
40
30
20
10
−30
−20
−10
0
10
20
30
−50
−40
−30
−20
−10
0
10
20
30
40
50

(b) B-mode

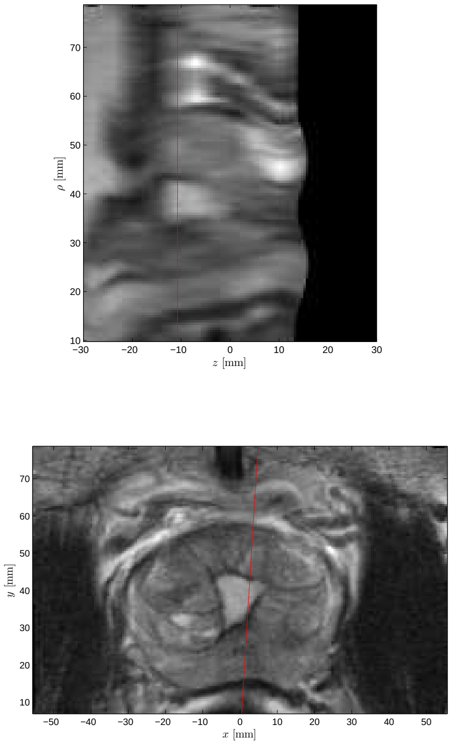
ρ [mm]
z [mm]
y [mm]
x [mm]
70
60
50
40
30
20
10
−30
−20
−10
0
10
20
30
−50
−40
−30
−20
−10
0
10
20
30
40
50

(c) T2w

Figure 4.4: Proposed augmented visualization. (a) The current surgeon's console display augmented with intraoperative TRUS using TilePro, as proposed in [94]. (b) Intraoperative sagittal (top) and transverse (bottom) TRUS. (c) The proposed additional data of the registered sagittal (top) and transverse (bottom) MR. The line (red) represents the real-time probe's sagittal angle and axial position to facilitate navigation and orientation.

4.3.4 Application in MR-Guided RALP

As discussed in Section 4.1 above, the purpose of the proposed registration is to allow intraoperative MR-guidance during CaP interventions. Specifically, we intend to employ the registration during RALP and augment the display of the surgeon's console with relevant preoperative MR data.

In [94], the authors introduced a system of an intraoperative motorized TRUS that is calibrated to the da Vinci system and tracks the robot's tooltip. This allows the surgeon to control the TRUS imaging plane automatically by moving the surgical instrument, and to watch the corresponding image of the prostate and periprostatic anatomy from the surgeon's console in real-time during RALP. The system has been tested clinically and was found useful in certain stages of the surgery, e.g., in defining the prostate-bladder interface during posterior and anterior bladder neck dissection, and identifying the prostate boundary at the apex.

The tracking method involves a rigid registration between the da Vinci surgical manipulators coordinates and the motor of the TRUS probe manipulator. This registration, described in [2], is performed as initialization and requires localization of the surgical tooltips in the 3-D TRUS. The da Vinci application programming interface (API) is then used to provide the locations of the tool tips in the da Vinci kinematic frame, and to update these locations in real-time.

The registered TRUS images are streamed to the surgeon's console and displayed below the standard camera view of the surgical site using the TilePro feature of the robot. We propose to employ the segmentation-based MR-TRUS registration above, and to display, in addition to the sagittal B-mode, the corresponding registered T2w image, and the transverse counterparts of both the B-mode and T2w. Figure 4.4 illustrates the current, and our proposed augmented visualization.

We note, however, that while the sagittal TRUS image can be streamed and displayed in real-time, the rest of the images are frozen and only valid with respect to the time of the initial sweep of the probe, when the data was acquired. In case time and clinical conditions allow, additional sweeps followed by the proposed registration process may be acquired in order to update the images.

4.4 Elasticity-Based Registration

As discussed in Chapter 3, utilizing elasticity information can facilitate registration and improve its accuracy. Indeed, one approach to utilize the acquired elastography information for TRUS-MR registration is to employ the proposed model-based algorithm from Chapter 3, with the segmented intraoperative TRUS volume as the reference model, and MRE magnitude and elastogram volumes as the template and its regularizer. Alternatively, one may employ this algorithm with the segmented MRI as the reference model, and the TRUS B-mode and USE volumes as the template. However, this intensity-driven and regularized approach may require more iterations with smaller step sizes, which will yield longer running times that may not be suitable for intraoperative deployment of the algorithm.

Another approach to employ elastography is to use [143] and [102] to segment the USE and MRE volumes, and employ the proposed segmentation-based method above for TRUS-MR registration. However, this approach too requires preprocessing steps that may generate errors. In this section, we are taking a different approach and investigate the utilization of the "pure" elastography data, of both modalities, as an inter-modality to allow intensity-based registration of the corresponding MR and US volumes.

4.4.1 Registration Process

Suppose that we have $E_{\mathrm{US,SAG}}(\rho, \theta, z)$, the sagittal intraoperative USE volume. Using the conversion in (4.1), we obtain the transverse USE volume, $E_{\mathrm{US,TRV}}(\bar{r})$. In addition, we are given $E_{\mathrm{MR,TRV}}$, the transverse MRE volume, and assume that the center of the rectum (that corresponds to the TRUS probe in USE) is found, either manually or automatically. The volume can be then converted to the sagittal $E_{\mathrm{MR,SAG}}$ volume using (4.4) with respect to that center.

The USE method is based on estimation of displacements along the radial direction on the sagittal plane, on which the data is in its native resolution. As shown in Figure 4.6, the elastograms are blurred and noisy. Thus, we limit the transformation model to translation and rotation about the z-axis, and formulate the problem in sagittal coordinates as

$$\min_{\delta\theta, \delta z} \mathcal{F}[E_{\mathrm{US,SAG}}, E_{\mathrm{MR,SAG}}(\rho, \theta + \delta\theta, z + \delta z)], \tag{4.8}$$

where $\mathcal{F}$ is the distance metric between the two volumes.

Ideally, the elastograms of both MRE and USE represent the same tissue elasticity, and therefore an SSD or NCC metric would be a proper choice. However, as can be seen by a typical joint histogram of two registered elastograms in Figure 4.6(c), there is a nonlinear and non-injective relationship between them. Therefore, we chose to minimize the inverse of the (normalized) MI as the metric $\mathcal{F}$.

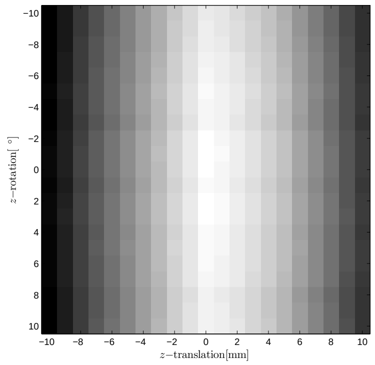

(a) MI metric

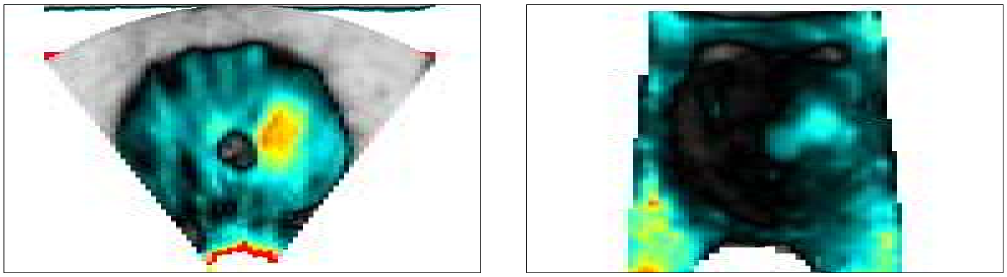

(b) USE

(c) Registered MRE

Figure 4.5: Elasticity-based registration of a phantom. (a) The MI similarity map with respect to axial translation and rotation. The maximum value is at (0,0), where the volumes are registered. (b)-(c) Cross-sections of the registered volumes. Intensity scale of the elastograms is 0-50 kPa.

Phantom Experiment

We first study registration of a prostate elastography phantom (Model 066, CIRS, VA, USA). The USE system, described in [79], includes an US machine (BK Medical, Herlev, Denmark) with a biplane transrectal transducer (Endocavity 8848, 4–12 MHz) mounted on a motorized cradle, similar to Section 4.3.3. The algorithm in [10] was implemented to provide real-time absolute elastography using a transperineal voice coil as the shaker (with 75 Hz excitation). We also used the transperineal MRE system with similar scanning parameters and processing to the description in Section 3.5.1.

Here, we study the use of the MI metric as a similarity measure. The MRE and USE volumes were registered manually, based on the prostate and inner inclusions. Then, axial translations and rotations were applied, with the MRE volume as the template, and the MI value was recorded for each pose. In Figure 4.5(a), the resulting MI similarity map is depicted with respect to the axial translation and rotation parameters. As desired, the

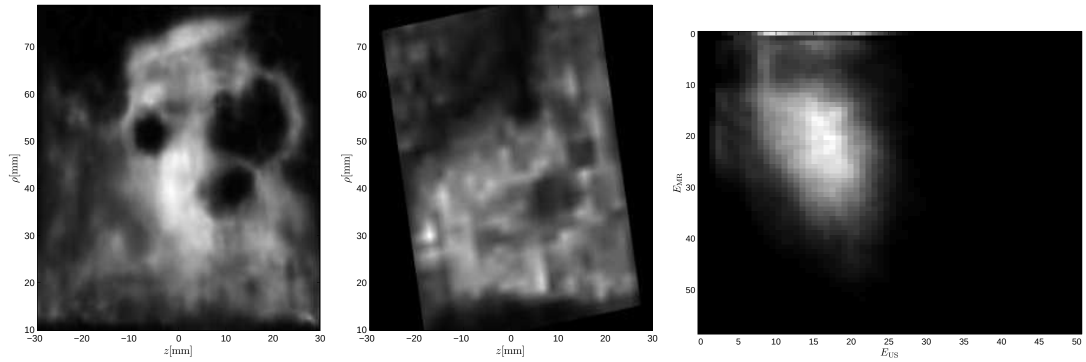

(a) USE (b) Registered MRE (c) Joint histogram

Figure 4.6: Elasticity-based registration of patient data. (a) A sagittal slice of the USE reference. (b) A sagittal slice of the registered MRE template. (c) The joint histogram of the registered volumes.

global maximum value is at (0,0), where the volumes are registered. However, we note that there are many local maxima as well, and that the function changes slowly with respect to rotations. Thus, a gradient descent based algorithm fails to optimize the metric, and we employ search-based methods, e.g., the Nelder-Mead simplex method.

Patient Data

The registration was performed offline on four patient's data sets that comprise both preoperative MRE and intraoperative USE. First, the volumes were smoothed using $3 \times 3 \times 3$ median filtering. Due to off-axis rotation of the two volumes, the center of the rectum in the MRE volume was selected on both the base and apex of the transverse magnitude image, and the sagittal volume was rotated accordingly. Then, the Nelder-Mead simplex method was used to minimize the inverse of the normalized MI between the volumes, with respect to axial rotation and translation.

Illustration of the resulting registration of one data set is presented in Figure 4.6. On the selected sagittal slice, we see that there are matching landmarks on both volumes. However, some landmarks significantly differ on the two modalities. To evaluate the registration, the resulting transformation was applied to the binary volume of the segmented MR, and was then compared to the rigid registered volume that was obtained using the principal axes transformation, as described above in Section 4.3.2. In two of the cases, depending on the initial pose, we noticed a convergence to local minima. Still, the resulting mean volume overlap of $81.2\% \pm 6.4\%$ is relatively high.

4.5 Discussion and Conclusion

In this chapter we presented methods for registration of intraoperative TRUS and preoperative MRI. With MRI correctly registered, multi-parametric imaging and cancer probability maps can be displayed on the surgeon's console to augment visualization of the prostate, periprostatic anatomy, and CaP for facilitating orientation, planning and navigation during RALP.

We proposed a segmentation-based approach that incorporates an existing semi-automatic segmentation of the prostate in the B-mode volume, and then deforms the segmented T2w volume to match the two surfaces. The registration performance was found to be plausible, with comparable values to other TRUS-MR registration methods. Specifically, in terms of volume overlap, the proposed method was found to be slightly superior to a similar method that uses FEM. The registration errors for the proposed method, based on the urethra, were slightly inferior to the FEM method. However, since the urethra can be significantly deformed within the prostate, especially in the presence of a Foley catheter, as is the case during intraoperative TRUS imaging, it is not necessarily a good anatomical landmark.

In order to evaluate the registration alone, i.e., differentiate its errors from the segmentation errors, we used the manual segmentations of the TRUS in our experiments rather than the resulting semi-automatic segmentations. Thus, to evaluate the expected intraoperative errors, one should aggregate the reported segmentation error reported in [142]. Similarly, for using the tooltip tracking system, the errors in calibration and during tracking should be considered. Further evaluation of the algorithm may employ histopathology images, registered to both MR and TRUS by using, e.g., the algorithm in Chapter 2, as an inter-modality for comparing the MR volumes before and after registration to TRUS.

In addition, compared with the FEM method, the proposed method does not require meshing, and its runtime is predictable (constant, for a fixed number of iterations) and significantly shorter (3 min as opposed to 7–9 min). Including the setting up the equipment, the initial sweep of the probe, segmentation, registration and calibration to the robot, we expect the entire process to consume 12-15 minutes of operating room time prior to surgery. From our past experience during RALP in [94, 98], this is a feasible time frame at the beginning of the procedure, with which clinicians are comfortable.

We note, however, that even with the most accurate imaging and registration, relying solely on preoperative information to define a surgical plane is not recommended, due to high risk of positive margins CaP. Therefore, the proposed MR-TRUS registration is more suitable for surgical planning, at the beginning of the procedure. A clinical study that employs the proposed system is to be conducted in order to determine its role in achieving surgery goals and improving outcomes. The proposed registration can also be employed offline for learning 2-D TRUS features that correspond to findings in MR, which may then assist clinicians in real-time guidance using TRUS.

In the second part of this chapter, we investigated intensity-based registration of MRE and USE. Such registration can be used for aligning the corresponding T2w and B-mode volumes without preprocessing such as segmentation. We found that the discrepancy between the elasticity values in the two elastograms does not allow employment of unimodal similarity measures. Nevertheless, by employing a proper metric, e.g., MI, the intensities of the elastograms may allow a rigid alignment.

The difference in elasticity values of the two volumes may stem from the noisy characteristics of the elastograms, different acquisition methodologies, different spatial sampling that may introduce aliasing of different higher frequency components, difference in displacement estimation (full 3-D in MRE, and radial in USE, errors caused by the pressure of the TRUS probe, and a slightly different excitation frequency (70 Hz in MRE and 75 Hz in USE).

Other future work in elasticity-based registration may include extraction of intensity invariant features that are stable and unique to the elastograms, thus reducing the problem to point-based registration. These features can be stiff inclusions that are clearly visible on both modalities, or edges that can be used as surface landmarks. Another approach is to utilize the MRI and MRE volumes in order to simulate images that are closer to US or USE, similar to the approach in [169], where US images were simulated from computed tomography volume to facilitate multi-modality registration. Also, improving data acquisition, e.g., by increasing MRE resolution, may allow for a better registration. However, such improvements may not be feasible in practice, either preoperatively or intraoperatively, due to a longer scanning time. In the following chapters we take different approaches for improving MRE, without prolonging acquisition time.

Chapter 5

Motion Compensation and Super-Resolution in Magnetic Resonance Elastography

5.1 Introduction

In conventional MRE, each spatial component of the 3-D displacements is encoded separately by applying motion encoding gradients (MEGs) along the corresponding direction. The wave is sampled at different stages during its cycle by varying the phase shifts between the mechanical excitation and the MEGs in each acquisition. Although the Nyquist rate requires only two samples per direction to estimate the amplitude and phase of the displacements at each voxel [104, 166], typically more samples are acquired to improve signal-to-noise ratio (SNR). A temporal discrete Fourier transform (DFT) is then performed to extract the displacements' amplitude and phase from the fundamental frequency component of the samples.

Due to the oversampling of the wave, an MRE scan with a typical field of view is a lengthy process that may cause inconvenience to the patient, and increases the possibility of both voluntary and involuntary movements. As in MRI, patient's movements in MRE introduce motion artifacts such as ghosting in the reconstructed images. Furthermore, in MRE, such motion corrupts displacement estimation, which in turn degenerates elastogram reconstruction. Thus, there is a tradeoff in acquiring more samples to improve SNR, or fewer samples to reduce patient's movements. For a clinical usage of MRE, a compromise is to allow reasonable scanning times by acquiring four or eight samples of lower spatial resolution images.

Previously, several approaches were considered to suppress patient's movement during MRI scans. These range from physical constraints such as a belt wrapped around the patient in free-breathing abdominal MRI [62], through specialized filling of k-space [121], to image processing techniques [170].

In this work, we utilize the redundancy of images acquired in MRE, and apply image registration to compensate for patient's motion during the scan. We also employ a super-resolution technique to enhance the resolution of the acquired images to allow for a better estimation of tissue displacements.

In the MRE acquisition process, the phase component of the complex imaging signal, also known as the phase image or volume, encodes the displacement, while its magnitude component is still available as a low-resolution T2w image, also known as the magnitude image or volume, that provides similar intensity information and features as high-resolution one [102]. Since the corresponding phase images are derived from the same signal as the magnitude images, each such pair of phase-magnitude images is inherently registered. Ideally, all the magnitude images, acquired in different directions and wave samples, are identical. In practice, however, the magnitude images vary due to noise and patient's movements. Thus, motion among different acquisitions of phase images can be compensated by registering the corresponding magnitude images.

In case of multiple images of the same scene or object, super-resolution methods can be used to increase the native size of images [113]. Rather than basic interpolation methods, which introduce artifacts such as blur and contrast loss, super-resolution techniques efficiently improve resolution by incorporating information from the different images. Super-resolution methods have been applied to medical imaging to enhance the acquired data and increase diagnosis [49].

In MRE, the DFT processing of the oversampled phase images coincides with a linear least-squares estimation of the displacements [104]. Here, we consider pairs of phase images that represent the same displacement's phase and amplitude (up to a sign flip and noise), and should complement each other in other in terms of intensity information after motion compensation. In addition, due to the mechanical nature of MRE sequence, although actual data acquisitions are at rest, small displacements of the scanned object occur on a sub-voxel scale, and the images may contain different information. Thus, we propose to employ a super-resolution method to utilize this complementary property and increase the resolution of the acquired data.

5.2 Methods

5.2.1 Motion Compensation Using Registration

Let $I^{(i,k)}$, $\Phi^{(i,k)} \colon \mathbb{R}^3 \to \mathbb{R}$ denote the kth acquisition of the magnitude and phase volumes, respectively, in direction $i \in \{x, y, z\}$ on the 3-D domain $\mathcal{D} \subseteq \mathbb{R}^3$. We consider a conventional MRE sequence that comprises K acquisitions in each direction, with phase shifts of the MEGs that are evenly distributed over $[0, 2\pi)$.

As discussed above, we compensate for patient's motion by registering the magnitude volumes. Without loss of generality, we consider $I^{(x,1)}$ as the reference volume, and register each template volume $I^{(i,k)}$ by minimizing the following energy functional

$$\begin{aligned} \mathcal{J}[\bar{u}^{(i,k)}; I^{(i,k)}, I^{(x,1)}] = & \int_{\mathcal{D}} \left(I^{(i,k)}(\bar{r} - \bar{u}^{(i,k)}) - I^{(x,1)}(\bar{r}) \right)^2 d\bar{r} \, + \\ & \int_{\mathcal{D}} \left(\frac{\mu}{4} \sum_{j=1}^{3} \sum_{l=1}^{3} \left(\frac{\partial \bar{u}_j^{(i,k)}}{\partial \bar{r}_l} + \frac{\partial \bar{u}_l^{(i,k)}}{\partial \bar{r}_j}\right)^2 + \frac{\lambda}{2} (\mathrm{div} \ \bar{u})^2 \right) d\bar{r} \ , \\ & \forall \ i \in \{x, y, z\}, \ k \in \{1, \dots, K\}, \end{aligned} \tag{5.1}$$

where $\bar{r} = (x, y, z)^T$ is the spatial coordinate vector, and λ and μ are the Lamé parameters that reflect the elastic properties (μ is also known as the shear modulus). The minimization of the functional is with respect to the deformation field, $\bar{u}^{(i,k)} = (u_x^{(i,k)}, u_y^{(i,k)}, u_z^{(i,k)})^T : \mathcal{D} \to \mathbb{R}^3$, which maps $\tilde{I}^{(i,k)} = I^{(i,k)}(\bar{r} - \bar{u}^{(i,k)})$ to $I^{(x,1)}$.

The first component of the functional (5.1) is a similarity measure between the template and reference volumes, while the second component is a regularizer of the deformation map. Since the template and reference are both magnitude volumes of the same intensity range, we employ SSD as an intramodality similarity measure. Due to the elastic nature of the deformation, the regularizer was chosen as the linear elastic potential.

The minimization of (5.1) is performed in a variational approach. The algorithm is implemented on a fixed grid using finite differences, similar to the description provided in [92]. The registration of one template volume to the reference is demonstrated in Figure 5.1.

5.2.2 Super-Resolution in MRE

As discussed in Section 5.1, the phase and magnitude images are inherently registered. Thus, we apply the resulting deformation map of each magnitude image to the corresponding phase image, $\tilde{\Phi}^{(i,k)} = \Phi^{(i,k)}(\bar{r} - \bar{u}^{(i,k)})$, to compensate for motion in the phase images. Considering a conventional MRE sequence of K phase shifts evenly distributed over $[0, 2\pi)$ in each direction, the phase images $\tilde{\Phi}^{(i,k)}$ and $-\tilde{\Phi}^{(i,k+\frac{K}{2})}$ should be similar and differ on a sub-voxel scale, since they sample a certain phase and anti-phase of the displacement wave.

As in most super-resolution approaches, we attempt to recover a high-resolution image of double the size in each axis of the native resolution volume. We employ an iterative back-projection super-resolution method, first introduced in [61], with a steepest-descent

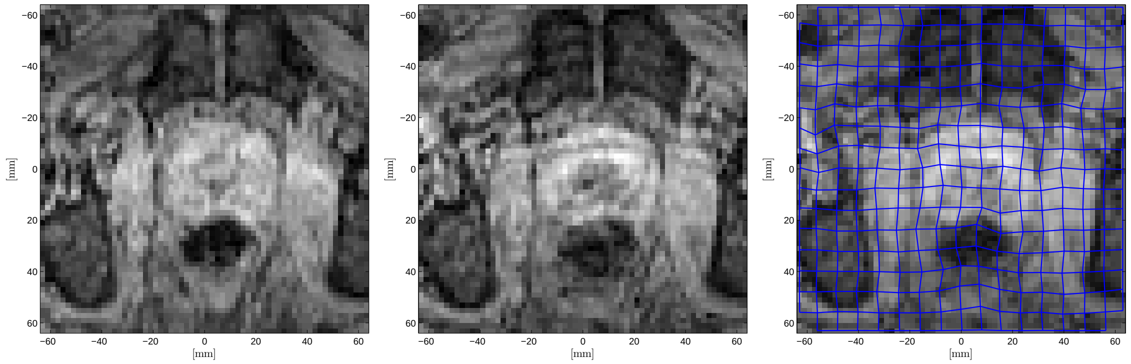

(a) $I^{(x,1)}$ (the reference) (b) $I^{(z,8)}$ (a template) (c) $\tilde{I}^{(z,8)}$ (registered temp.)

Figure 5.1: Motion compensation using registration. Cross-section of the MRE magnitude volumes from the mid-gland region of a patient's prostate scan. The blue grid represents the sampled deformation field.

choice of the back-projection kernel [35].

The iterative algorithm, adapted to the context of phase images in MRE, starts with an initial guess of the super-resolution image, $\hat{\Phi}^{(i,k),0}$, which in our case is taken as the mean phase image $\frac{1}{2}(\tilde{\Phi}^{(i,k)} - \tilde{\Phi}^{(i,k+\frac{K}{2})})$, interpolated on a high-resolution volume. Then, in each iteration $j = 1, 2, \ldots$, the high-resolution volume is updated by

$$\hat{\Phi}^{(i,k),j+1} = \hat{\Phi}^{(i,k),j} + A_{BP}\left(\tilde{\Phi}^{(i,k)} - \tilde{\Phi}^{(i,k+\frac{K}{2})} - 2A_{BP}^{T}\hat{\Phi}^{(i,k),j}\right),$$
$$\forall\ i \in \{x, y, z\},\ k \in \{1, \ldots, \frac{K}{2}\}, \tag{5.2}$$

where the back-projection "tall" matrix A_{BP} comprises translation, blurring and downsampling of the high-resolution image. Note that the 3-D volumes are rearranged as column vectors in (5.2), and similarly, the resulting long column vector is rearranged back into the super-resolution volume.

In each iteration, the algorithm minimizes the SSD between the two native resolution phase images and the translated, blurred and downsampled estimation of the current super-resolution volume. Note that since the images are motion compensated, zero translations are chosen. Also, without prior information on the scanner, a $3 \times 3 \times 3$ kernel of a Gaussian blurring is used. A temporal DFT is then performed on the super-resolution phase images $\hat{\Phi}^{(i,k)}$, $k = 1, \ldots, \frac{K}{2}$ to extract the super-resolution displacements' amplitude and phase from the fundamental frequency component of the samples, followed by reconstruction of the super-resolution elastogram.

5.3 Results

5.3.1 Phantom Experiment

We have acquired an MRE scan of an elasticity phantom (Model 049, CIRS, VA, USA) using a custom-made shielded electromagnetic transducer synchronized to the 3-Tesla scanner (Achieva 3.0T, Philips, The Netherlands). We employed a spin-echo (SE)-echo-planar imaging (EPI) pulse sequence with a TE/TR of 30/1600 ms. A 200 Hz vibration was applied to the rectangular shaped phantom. As seen in Figure 5.2(e), the phantom contains spherical inclusions of different radii and stiffness values relative to the background material that mimic different tissue types. The entire phantom was scanned in a field of view of $128 \times 128 \times 20$ grid, with an isotropic $2 \times 2 \times 2\text{mm}^3$ resolution. We have oversampled the scan of each acquisition with eight phase shifts of the MEGs ranging evenly over $[0, 2\pi)$ relative to the mechanical excitation. The scanning time was 364s per acquisition.

A $80 \times 60 \times 20$ region of interest on the acquired axial phase accumulation images was selected, compensated and phase unwrapped. Since the phantom is static, the motion compensation algorithm was not used. We applied the super-resolution algorithm described in Section 5.2.2 to double the resolution of the phase images. In addition, for comparison, a high-resolution phase images was computed using bilinear interpolation of the native resolution phase image. The native and high-resolution elastograms were reconstructed from the corresponding displacement maps using a LFE technique [85].

The elastograms are illustrated in Figure 5.2 for qualitative comparison. A corresponding mid-gland T2w image with an in-plane resolution of $0.732 \times 0.732\text{mm}^2$ is also presented to reveal the geometry of the phantom's inclusions. Further quantitative evaluation, presented in Figure 5.3, was performed by comparing the elastograms to the factory reported elasticity values of the inclusions. The root-mean-square errors between the factory values, and the native resolution and the super-resolution elasticity values were 6.57 ± 5.55 kPa and 4.73 ± 4.34 kPa, respectively.

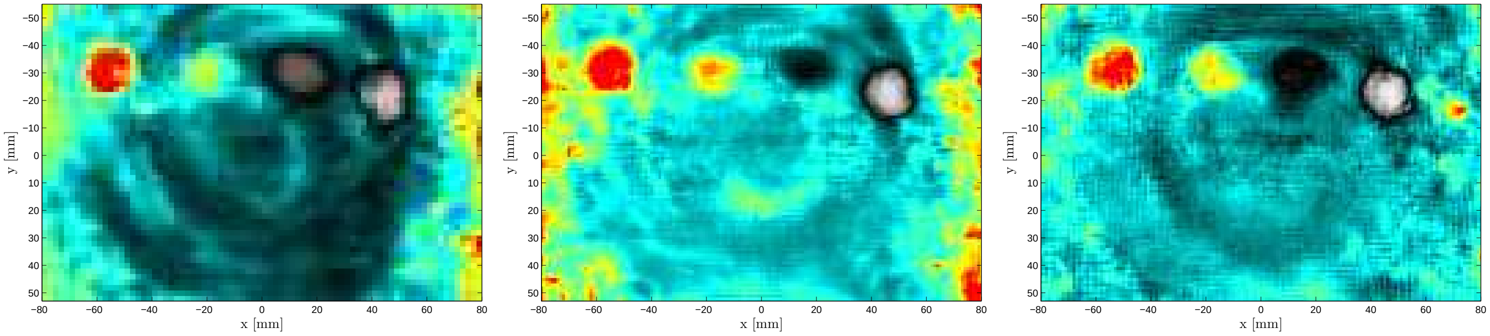
y [mm]
x [mm]
−50
−40
−30
−20
−10
0
10
20
30
40
50
−80
−60
−40
−20
0
20
40
60
80

(a) Native resolution (b) Bilinear interpolation (c) Super-resolution

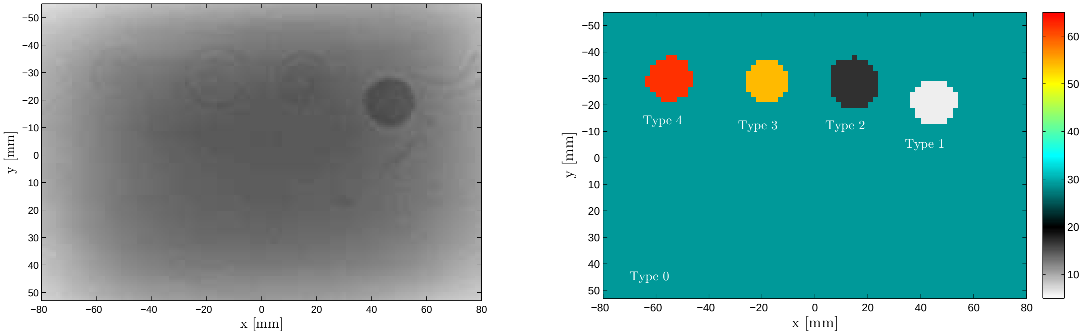
y [mm]
x [mm]
−50
−40
−30
−20
−10
0
10
20
30
40
50
−80
−60
−40
−20
0
20
40
60
80
Type 4
Type 3
Type 2
Type 1
Type 0
60
50
40
30
20
10

(d) T2-weighted (e) True elastogram (in kPa)

Figure 5.2: Super-resolution of a phantom MRE. (a)-(c) Corresponding cross-sections of the reconstructed elastograms. Intensity scale is in kPa and same as in (e). (d) The T2w image. (e) The factory reported elasticity values of tissue types.

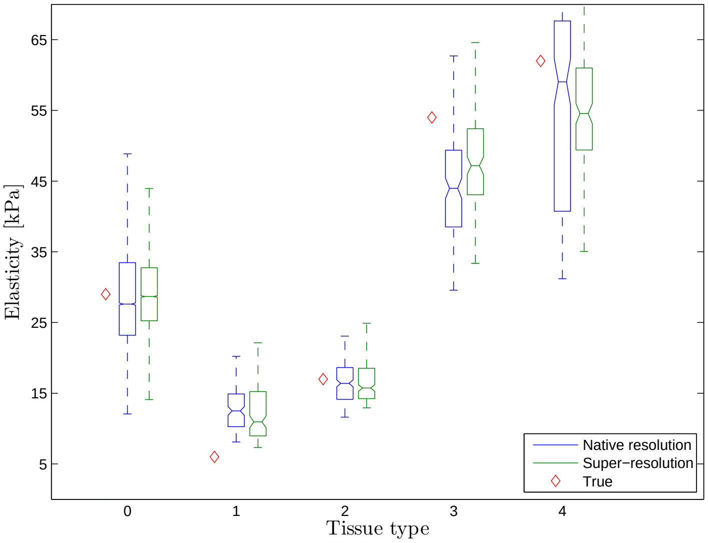

Figure 5.3: Phantom elasticity errors. The errors between the native and super-resolution elastograms in comparison with the true elasticity on each tissue type.

5.3.2 Patients' Data

The patients' data was acquired as part of a project for evaluating CaP detection using MRE. After approval of the institutional ethics board and signed consents, twelve patients (mean age 65, range 59–76 years old) who were scheduled for radical prostatectomy, underwent a preoperative scan in a 3-Tesla MRI scanner (Achieva 3.0T, Philips, The Netherlands) with a standard 6-channel cardiac coil with acceleration factor (SENSE) of 2.

A standard axial T2w FSE sequence was acquired (TE/TR = 86/2500 ms, FOV = $320 \times 320 \times 70$ mm^3, with 0.5 mm in-plane resolution and 2 mm slice thickness). Next, a prostate MRE scan was acquired using a transperineal shielded electromagnetic transducer [135], and a gradient echo sequence named eXpresso [136]. Eight phases were encoded with a mechanical excitation of 70 Hz applied to the perineum of the patient. Wave images were acquired on a $128 \times 128 \times 24$ matrix with 2 mm isotropic voxel size. The MRE scan lasted 8 min for a 3-D displacement field acquisition. Each slice was cropped to accommodate 64×64 pixels around the prostate region for computational efficiency.

We applied the motion compensation algorithm proposed in Section 5.2.1 to the MRE magnitude images. We note that in the MRE pulse sequence we used, the different acquisitions in each direction are multiplexed, and therefore, in the motion compensation algorithm, we have registered the mean volumes over all acquisitions for each direction, rather than each individual acquisition.

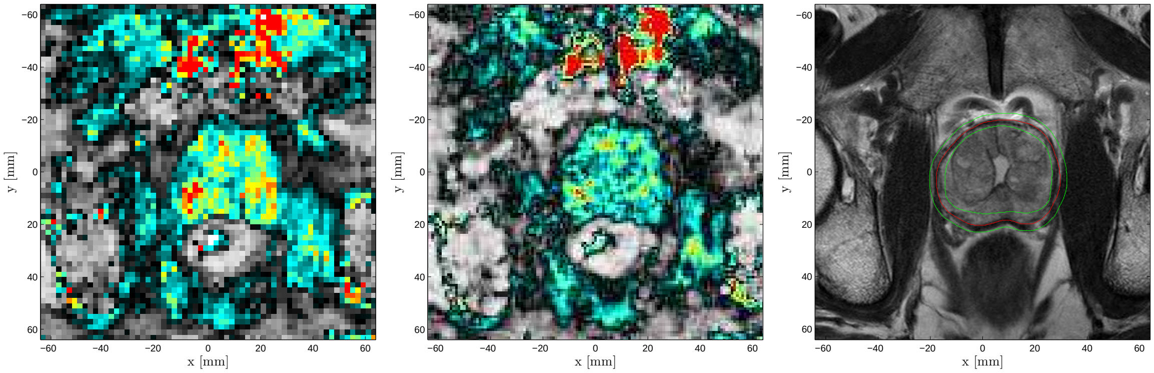

(a) Native resolution (b) Super-resolution (c) T2-weighted

Figure 5.4: Super-resolution of a patient's prostate MRE. Cross-section of the elastograms and T2w image. Manual segmentation (red) of the prostate, and the inside and outside bands that were used for contrast evaluation. Intensity scale of the elastograms is 0-30 kPa.

We then employed the proposed super-resolution technique on the patients' data. Qualitative results on a mid-gland slice of one case are presented in Figure 5.4. We may notice that on the super-resolution image, the prostate is more separable from its surrounding tissue than on the native resolution image. In order to quantify the results, we utilize the corresponding segmented T2w volume. For evaluation of the gland contrast and edge strength in the elastograms, we measure the contrast-to-noise ratio [17, 143] and the mean gradient on the surface, i.e.,

$$\begin{aligned} \text{CNR} =& 2(c_{in} - c_{out})^2/(\sigma_{in}^2 + \sigma_{out}^2) \\ \text{MeanEdge} =& \oint_{\Gamma} \|\nabla E\| \, d\bar{r} \Big/ \oint_{\Gamma} d\bar{r} \end{aligned} \tag{5.3}$$

where c_{in}, σ_{in} and c_{out}, σ_{out} are the mean and STDV values of the elastogram E on two bands, inside and outside of the segmentation surface Γ, as illustrated in Figure 5.4(c). In the computation of the edge strength, a $3 \times 3 \times 3$ Gaussian filtering was performed on the elastograms for noise reduction in the gradients.

5.4 Discussion and Conclusion

We have presented an image processing approach for enhancing MRE data. The approach employs image registration to compensate for motion of patients during the, typically lengthy, acquisition process, in order to improve the accuracy of the reconstructed elastogram. Then, a super-resolution technique is employed to increase the resolution of the

Patient	NCC Difference (%) y	z	CNR Native	Super-res.	MeanEdge (kPa/mm) Native	Super-res.
$P01$	1.12 ± 0.08	2.27 ± 0.11	1.1	1.2	3.1	3.8
$P04$	5.34 ± 0.58	1.21 ± 0.61	5.5	7.8	2.4	3.5
$P05$	0.93 ± 0.15	4.76 ± 0.16	8.9	13.2	1.3	2.5
$P06$	1.21 ± 0.38	4.88 ± 0.51	1.8	2.5	1.5	2.7
$P08$	2.22 ± 0.12	4.28 ± 0.15	9.3	12.5	2.3	2.8
$P10$	0.23 ± 0.05	0.14 ± 0.06	23.1	20.9	3.9	3.3
$P12$	1.62 ± 0.06	3.55 ± 0.10	12.9	7.3	1.2	1.6
$P15$	0.69 ± 0.01	0.11 ± 0.01	0.6	4.3	2.3	3.2
$P17$	0.20 ± 0.06	1.51 ± 0.07	9.9	10.4	2.7	3.6
$P18$	0.13 ± 0.03	0.71 ± 0.09	7.0	7.7	2.6	2.5
$P19$	1.03 ± 0.12	3.36 ± 0.09	10.1	13.6	2.3	3.0
$P20$	0.52 ± 0.40	2.44 ± 0.43	1.9	3.7	1.2	1.8
Mean	1.33 ± 0.55	2.84 ± 0.74	7.7 ± 6.4	8.8 ± 5.7	2.2 ± 0.8	2.9 ± 0.7

Table 5.1: Super-resolution results on clinical data. The increase in NCC of the magnitude images in directions y, z (direction x is the reference) resulting from motion compensation. The contrast-to-noise ratio and edge strength of the prostate in the native and super-resolution elastograms (higher is better).

registered phase images. The proposed approach utilizes unique properties of the MRE acquisition process, namely, the similarity of the "by-product" magnitude images used for compensating motion in the phase images, and the redundancy of the phase images used for super-resolution.

We note that, in MRI, super-resolution has been proven to be of limited benefit in-plane due to the inherent bandlimited nature of the Fourier encoded images [144]. However, in our approach, we employ super-resolution on the phase component of the signal, and assume that the nonlinear residual physical movements of the object (rather than shifts in FOV), and synchronization errors in MRE allow for higher frequency components to be recovered. Indeed, in [132], the authors proposed similar nonlinear deformations for in-plane super-resolution in diffusion MRI.

We have tested the proposed approach on phantom and clinical data of CaP patients. Indeed, the NCC was increased after registration in our motion compensation approach. However, in some cases, the improvement is not significant, which implies that patient's motion was low. In a recent study by our group, [137], the effect of motion compensation on elasticity-based CaP detection was examined. The results are mixed, with classification of lesions being improved on average in the peripheral zone, where the majority of cancer lesions are, but worsened in the central zone. This may be due to the fact that the gland is stiffer in the central zone, while we assumed a homogeneous elasticity regularization. Future work may include an iterative registration process that uses the inhomogeneous elasticity of the reconstructed elastogram in each iteration, similar to [103], for improving estimation accuracy of the deformations.

The evaluation of the super-resolution method on an elasticity phantom showed that, on average, the super-resolution elasticity values were closer to the reported factory values. However, the values of the stiffest inclusion are lower in the super-resolution elastogram. This result might be due to a higher wavelength-to-voxel size ratio that may not be suitable for optimal reconstruction. In general, on both phantom and clinical data experiments, the geometry of the inclusions/prostate in the super-resolution volumes is shown better than in native resolution. In some cases, however, the improvement is not significant, and on some super-resolution images there are image artifacts and patterns, typically around the base and apex, that might be caused by registration error. Nevertheless, on average, the improved contrast and edge strength around the prostate allow better separability of the gland from its surrounding tissue, and may facilitate automatic segmentation algorithms. We note that in the displacement estimation for reconstruction of the super-resolution elastogram, only four samples are used (pairs of registered phase and anti-phase images), rather than eight samples used in the native resolution elastogram. The SNR in the super-resolution image is therefore improved due to the specific utilization of the information.

For simplicity and due to a lack of prior information on the scanner imaging process, we have employed a Gaussian blur in the proposed super-resolution algorithm. However, as future work, the scanner's actual point spread function of phase might be calculated similar to [127] in order to accurately model the blurring. Future work may also include improved reconstruction methods using FEM combined with sparsity regularization [57]. In addition, increasing the vibration frequency to reduce the wavelength-to-voxel size ratio, or acquisition of multi-frequency MRE, may allow for better elasticity reconstruction. However, transperineal excitation beyond 100 Hz may not be feasible due to the high attenuation of the waves near the perineum.

Chapter 6

Optimization-Based Design of Motion Encoding in Magnetic Resonance Elastography

6.1 Introduction

The most prevalent dynamic MRE technique involves the application of a harmonic mechanical excitation that generates shear waves in the tissue. The resulting displacements are estimated by employing an MRI pulse sequence with MEGs. These MEGs are bipolar gradients (typically in shape of a sinusoid or trapezoid) that are synchronized to the mechanical excitation. The phase accumulated by each isochromat is encoded in the phase component, also known as the phase image, of the MRI signal.

Conventional motion encoding in MRE comprises unidirectional MEGs, in which each component of the displacement vector is encoded separately by applying the gradients in the corresponding direction. The measured phase accumulation, i.e., each voxel of the phase images, is a sinusoid with respect to a phase shift between the MEG and the mechanical wave. Thus, a sufficient number of consecutive acquisitions with varying phase shifts are required in order to sample the temporal characteristics of the wave. The amplitude and phase of the displacement at each voxel are then estimated through a DFT of the samples. Elastograms, i.e., images that depict tissue elasticity or stiffness can be reconstructed from the displacements by solving an inverse problem using, e.g., [57, 85, 107, 112, 151].

In [166], a generalized sampling method is proposed in order to achieve a sub-Nyquist sampling rate of two acquisitions per direction using a least-squares approach, thus reducing acquisition time of unidirectional sequences. In practice, however, due to noise in the measured phase images, MRE sequences typically require four or eight acquisitions in each direction in order to provide a displacement map and, in turn, an elastogram, with a reasonable SNR. This yields a longer acquisition time that hinders usage of MRE in some cases due to time constraints and limits on image quality. Longer acquisition times also introduce artifacts in the images due to patient movement.

There are approaches that have been proposed to improve SNR or, alternatively, reduce the acquisition time of MRE [46]. Most approaches propose improved imaging pulse sequences, such as EPI [85] and gradient-echo [44], as opposed to the basic SE sequence. Other approaches deal directly with the design of the MEGs, e.g., fractional encoding [56, 131], in which the mechanical frequency is taken as a fraction of the MEGs oscillation frequency. In [54, 116], sequence designs with combination of MEGs were applied to phase-contrast MRI, a field related to MRE, in order to reduce scan time and increase sensitivity for estimating the magnitude of flow in MR angiography.

Recently, [72, 173] have proposed approaches for encoding the 3-D displacements in MRE by applying the MEGs in all directions simultaneously. These multidirectional sequences have the potential of reducing the number of scans by three, while achieving the same SNR as in unidirectional sequences. In [173], MEGs are applied simultaneously with different frequencies, and the displacement is encoded for each direction by utilizing the filtering condition in [133]. In [72], the authors propose a sample interval modulation MRE, in which MEGs are applied simultaneously with different phase shift intervals, such that the phase accumulation in each direction can be recovered from the total accumulation by using DFT.

In this chapter we focus on optimization of the MEGs design. We parameterize general multidirectional sequences, and formulate the estimation of the 3-D displacement as a linear system in the time-domain. This allows derivation of a least-squares estimator that is optimal under a given design and noise model. We then characterize and set the problem in an experimental design framework, by which we quantify the performance of MEGs sequences, and derive parameters that lead to optimal multidirectional designs under a given optimality criterion. We fit the conventional MEGs sequence in the proposed framework, and compare the sequences on simulation and phantom data.

The remainder of this chapter is organized as follows. First, we present the generalized MEGs and corresponding phase accumulation, and propose a least-squares estimation of wave properties. We then present the framework for optimal design of motion encoding, and derive optimal sequences. We continue with a description of the experiments that were performed to evaluate our approach, and summarize the results. Finally, we conclude with discussion and future research directions. A summary of the notations used throughout this work is provided in Table 6.1.

Notation	Description	Typical values
$\bar{r} = (x, y, z)^T$	spatial coordinate vector	in m
t	time	in s
$\gamma/(2\pi)$	the gyromagnetic ratio	42.58MHz/T
i	spatial index	x, y, z
$\omega_m/(2\pi)$	mechanical frequency	200Hz
ξ_i	displacement amplitude in direction i	To be estimated (in the order of μm)
φ_i	displacement phase in direction i	To be estimated ($[-\pi, \pi)$)
$\omega_i/(2\pi)$	MEG oscillation frequency	200Hz
T_i	MEG period time ($T_i = 2\pi/\omega_i$)	5ms
q_i	fractional encoding ratio $q_i = \omega_m/\omega_i$	$q_i \leq 1$
$\lvert\mathcal{G}_i\rvert$	MEG amplitude	40mT/m
α_i	phase shift between MEG and vibration	$[0, 2\pi)$
β_i	start phase of the MEGs	$[0, 2\pi)$
δ_i	net phase ($\delta_i = \alpha_i - \beta_i$)	$(-2\pi, 2\pi)$
N_i	number of periods MEGs are applied	1
$W_{N_i T_i}(t)$	a window function with a $[0, N_i T_i]$ support	1 for $t \in [0, N_i T_i]$, 0 otherwise
Conventional 3-D design	a sequence comprising 24 unidirectional acquisitions (8 in each direction)	
RME	a sequence comprising a minimal number of 6 unidirectional acquisitions (2 in each direction)	
MD-RME	a sequence comprising a minimal number of 6 multidirectional acquisitions with sign-flips	
Optimal design	a sequence satisfying an optimality criterion (comprising 8 multidirectional acquisitions in our examples)	

Table 6.1: Summary and description of the notations.

6.2 Theory

6.2.1 Parameterized Motion Encoding Gradients

We denote the spatial coordinate vector as $\bar{r} = (x, y, z)^T$ and the time as t. We represent a steady-state harmonic mechanical wave through tissue by its 3-D displacement vector $\bar{\Psi} = (\Psi_x, \Psi_y, \Psi_z)^T$. Without loss of generality, we write

$$\Psi_i(\bar{r}, t) = \mathfrak{Im}\{\, |\xi_i(\bar{r})| e^{j\varphi_i(\bar{r})}\, e^{j\omega_m t} \} = |\xi_i(\bar{r})| \sin(\omega_m t + \varphi_i(\bar{r}))\ , \quad i = x, y, z \tag{6.1}$$

The wave frequency ω_m is the same as the known mechanical excitation frequency. The spatially varying amplitudes and phases in each direction, $|\xi_i|$ and φ_i, are unknown and have to be determined at each imaged voxel based on a number of phase images acquired in different acquisitions. Note that this representation can accommodate locally any type of wave (e.g., traveling or standing), wavefront (e.g., plane or spherical), polarization (e.g., linear or circular) and attenuation.

We parameterize general multidirectional sequences of sinusoidal MEGs, $\bar{G} = (G_x, G_y, G_z)^T$. Specifically, for each direction, we allow control of the (angular) frequency ω_i, the amplitude $|\mathcal{G}_i|$, the start phase β_i, the phase shift relative to the mechanical wave α_i, and the number of periods the gradients are applied $N_i \in \mathbb{N}$. We therefore have

$$G_i(t; \omega_i, N_i, |\mathcal{G}_i|, \alpha_i, \beta_i) = |\mathcal{G}_i| \sin(\omega_i(t - \alpha_i/\omega_i) + \beta_i)\, W_{N_i T_i}(t - \alpha_i/\omega_i)\ , \quad i = x, y, z \tag{6.2}$$

where $W_{N_i T_i}(t)$ is a window function with a $[0, N_i T_i]$ support, and $T_i = 2\pi/\omega_i$ is the time period of each MEG.

The effect of the parameters α_i and β_i on the MEGs is demonstrated on a single acquisition in Figure 6.1. Geometrically, this may be seen as if the gradients are rotating in a (piecewise) helical fashion as a function of time in gradient space.

6.2.2 Parameterized Phase Accumulation

In this chapter, we limit our discussion to MEGs with the same frequency as the mechanical frequency, i.e., $\omega_i = \omega_m$, $\forall i = x, y, z$. However, the theory can be extended to fractional encoding in each direction.

The phases accumulated by the precession of each moving isochromat during the acquisition sequence, as result of the MEGs, are encoded in the measured phase images of the MRI signal. As derived in the Appendix, the phase accumulation at each voxel as a

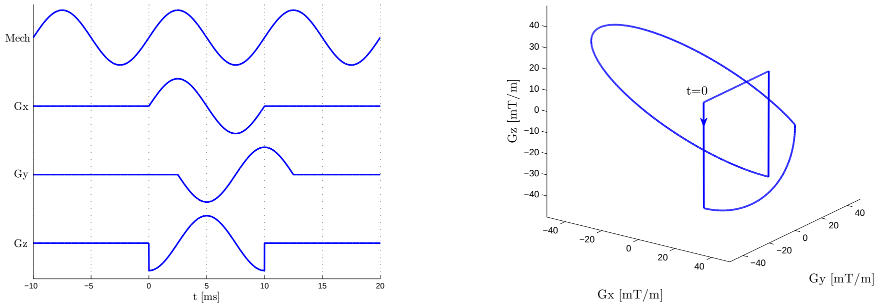

(a) Infinite slew rate

(b) Infinite slew rate

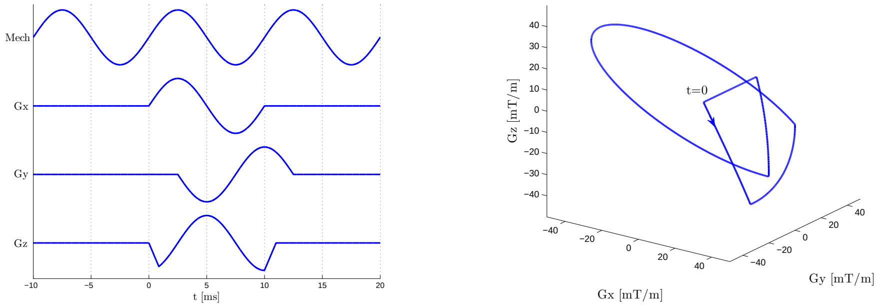

(c) Finite slew rate

(d) Finite slew rate

Figure 6.1: Example of MEGs sequence with $\bar{\alpha} = (0, \frac{\pi}{2}, 0), \bar{\beta} = (0, \pi, \frac{3\pi}{2})$. (a),(c) Plots of the MEGs in time with infinite and finite slew rate. (b),(d) Plots of the sequence in gradient space with infinite and finite slew rate.

function of the MEGs parameters is given by

$$\Phi(\bar{r}; \bar{N}, |\bar{\mathcal{G}}|, \bar{\alpha}, \bar{\beta}) = \sum_{i=x,y,z} \frac{\gamma \pi N_i |\mathcal{G}_i|}{\omega_m} |\xi_i(\bar{r})| \cos\left(\varphi_i(\bar{r}) + \alpha_i - \beta_i\right) \tag{6.3}$$

where γ is the gyromagnetic ratio. This equation is a generalization of the phase accumulation that was originally presented in [100].

In order to formulate the problem as a linear one, for every voxel, we define A_i, B_i to be such that

$$|\xi_i(\bar{r})| = \sqrt{A_i^2(\bar{r}) + B_i^2(\bar{r})} \quad , \quad \varphi_i(\bar{r}) = \arctan\left(\frac{-B_i(\bar{r})}{A_i(\bar{r})}\right) \; , \quad i = x, y, z \tag{6.4}$$

and, using the *harmonic addition theorem*, substitute in (6.3) to obtain

$$\Phi(\bar{r};\bar{N},|\bar{\mathcal{G}}|,\bar{\alpha},\bar{\beta}) = \sum_{i=x,y,z} \frac{\gamma\pi N_i|\mathcal{G}_i|}{\omega_m}\left[A_i(\bar{r})\cos(\alpha_i-\beta_i)+B_i(\bar{r})\sin(\alpha_i-\beta_i)\right] \tag{6.5}$$

Thus, for every voxel, estimation of the amplitudes $|\xi_i|$ and phases φ_i in each direction, is given by estimation of the six unknowns A_i and B_i, $i = x, y, z$. This requires a minimum of six acquisitions, i.e., six acquisitions of the phase image with different MEG parameters.

6.2.3 Optimal Estimation of Wave Properties

In general, we acquire $K \geq 6$ acquisitions with, possibly, different $\alpha_i^{(k)}$, $\beta_i^{(k)}$, $N_i^{(k)}$ and $|\mathcal{G}_i^{(k)}|$ in each direction $i = x, y, z$, and for each acquisition $k = 1, 2, \ldots, K$. We denote $\delta_i^{(k)} = \alpha_i^{(k)} - \beta_i^{(k)}$ as the net phase of each acquisition, and define the $K \times 6$ ("tall") *acquisition design matrix*

$$\mathcal{M} = \frac{\gamma\pi}{\omega_m}\begin{pmatrix} N_x^{(1)}|\mathcal{G}_x^{(1)}|\cos(\delta_x^{(1)}) & N_x^{(2)}|\mathcal{G}_x^{(2)}|\cos(\delta_x^{(2)}) & \cdots & N_x^{(K)}|\mathcal{G}_x^{(K)}|\cos(\delta_x^{(K)}) \\ N_x^{(1)}|\mathcal{G}_x^{(1)}|\sin(\delta_x^{(1)}) & N_x^{(2)}|\mathcal{G}_x^{(2)}|\sin(\delta_x^{(2)}) & \cdots & N_x^{(K)}|\mathcal{G}_x^{(K)}|\sin(\delta_x^{(K)}) \\ N_y^{(1)}|\mathcal{G}_y^{(1)}|\cos(\delta_y^{(1)}) & N_y^{(2)}|\mathcal{G}_y^{(2)}|\cos(\delta_y^{(2)}) & \cdots & N_y^{(K)}|\mathcal{G}_y^{(K)}|\cos(\delta_y^{(K)}) \\ N_y^{(1)}|\mathcal{G}_y^{(1)}|\sin(\delta_y^{(1)}) & N_y^{(2)}|\mathcal{G}_y^{(2)}|\sin(\delta_y^{(2)}) & \cdots & N_y^{(K)}|\mathcal{G}_y^{(K)}|\sin(\delta_y^{(K)}) \\ N_z^{(1)}|\mathcal{G}_z^{(1)}|\cos(\delta_z^{(1)}) & N_z^{(2)}|\mathcal{G}_z^{(2)}|\cos(\delta_z^{(2)}) & \cdots & N_z^{(K)}|\mathcal{G}_z^{(K)}|\cos(\delta_z^{(K)}) \\ N_z^{(1)}|\mathcal{G}_z^{(1)}|\sin(\delta_z^{(1)}) & N_z^{(2)}|\mathcal{G}_z^{(2)}|\sin(\delta_z^{(2)}) & \cdots & N_z^{(K)}|\mathcal{G}_z^{(K)}|\sin(\delta_z^{(K)}) \end{pmatrix}^T \tag{6.6}$$

By (6.5), for each voxel $\bar{r}$ we have a (typically overdetermined) linear system of equations

$$\bar{\Phi} = \mathcal{M}\bar{\mathcal{A}} + \bar{w} \tag{6.7}$$

where $\bar{\Phi} = (\Phi^{(1)}, \ldots, \Phi^{(K)})^T$ is a vector that comprises the measured phase accumulations in each acquisition, $\bar{\mathcal{A}} = (A_x, B_x, A_y, B_y, A_z, B_z)^T$ is the unknown coefficient vector that we need to solve the system for, and $\bar{w}$ is a random equation error that depends on the type of noise in the system.

We can re-write (6.7) as the estimation problem

$$\hat{\bar{\mathcal{A}}} = \arg\min_{\bar{\mathcal{A}}} \|\bar{\Phi} - \mathcal{M}\bar{\mathcal{A}}\| \ , \ \text{given } \mathcal{M},\ \bar{\Phi} \tag{6.8}$$

The distribution of $\bar{w}$, which can be interpreted as the noise introduced into the measured phase images during each acquisition, determines the type of norm in (6.8), and the choice of estimator $\hat{\bar{\mathcal{A}}}$. We model $\bar{w}$ as a white Gaussian noise (see Discussion section) with a variance of σ^2, and assume that $\mathcal{M}$ is full column rank. Under these assumptions, the *Gauss-Markov theorem* [65] states that the ordinary least-squares estimator is optimal (best linear unbiased estimator) in the sense of minimizing the mean squared error (MSE) in the estimation $E\|\hat{\bar{\mathcal{A}}} - \bar{\mathcal{A}}\|^2$. The least-squares estimator is defined by

$$\hat{\bar{\mathcal{A}}} = (\mathcal{M}^T\mathcal{M})^{-1}\mathcal{M}^T\bar{\Phi} = \mathcal{M}^{\dagger}\bar{\Phi} \tag{6.9}$$

where $\mathcal{M}^{\dagger}$ is the Moore-Penrose pseudoinverse of the matrix $\mathcal{M}$.

6.2.4 Optimal Design of Motion Encoding

The proposed MEGs parametrization provides several degrees of freedom that allow us to modify the acquisition design matrix in (6.6). The parameters should be diverse among acquisitions to yield linearly independent rows, such that $\mathcal{M}$ is full column rank. Clearly, the more acquisitions we acquire (larger K), the lower is the estimation error that the least-squares estimator obtains. However, this would increase acquisition time, which is undesirable as explained above.

Another option to reduce error is to increase the MEGs amplitude $|\mathcal{G}_i|$, the number of periods that they are applied N_i, or to decrease their frequency ω_i. However, the allowable range for the parameters above is rather small due to hardware limitations, acquisition time, and the size of the scanned target (such that enough wavelengths are imaged). Therefore, we focus on finding the parameters α_i and β_i that optimize the acquisition design matrix in the sense of minimizing the estimation error by the least-squares estimator in (6.9).

The problem above can be considered as a special case of the *experimental design problem* in statistics [69, 124]. A popular criterion for an optimal design is the so called D-optimality [18, 63], in which the determinant of $\mathcal{M}^T\mathcal{M}$, also known as the information matrix of the design, is maximized. Such D-optimum design minimizes the (generalized) variance of the best linear estimator [68]. Thus, maximizing the determinant of the information matrix is equivalent to minimizing the estimation error.

We can therefore formulate the D-optimal design problem in MRE as

$$\begin{aligned} &(\alpha_i^{(k)}, \beta_i^{(k)}) = \arg\max_{\delta_i^{(k)}} \det(\mathcal{M}^T\mathcal{M}) \ , \quad i = x, y, z \ , \ k = 1, 2, \ldots, K \\ &\text{given} \quad \omega_m, \ N_i^{(k)}, \ |\mathcal{G}_i^{(k)}|, \text{ and possible conditions on } \alpha_i^{(k)}, \beta_i^{(k)} \end{aligned} \tag{6.10}$$

As we typically do not favor any particular direction or acquisition, unless stated otherwise, we choose the same $N_i^{(k)} = N$ and $|\mathcal{G}_i^{(k)}| = |\mathcal{G}|$, $\forall i = x, y, z$, $k = 1, \ldots, K$.

While designs that yield the same determinant are theoretically equivalent in their estimation error, in practice, issues such as TE and TR increase, finite slew-rate, and different flow compensation characteristics affect SNR. Thus, in some cases, to minimize the TE of the sequence in each acquisition, we set the same $\alpha_i^{(k)} = \alpha^{(k)}$, $\forall i = x, y, z$. In other cases, to prevent discontinuities ("jumps") in the MEGs, we set $\beta_i^{(k)} = \{0, \pi\}$.

Looking at (6.6), we have a constant multiplied by a matrix with elements $\cos(\delta_i^{(k)})$ and $\sin(\delta_i^{(k)})$. In general, finding an $L \times L$ matrix that maximizes the (absolute) determinant among all $L \times L$ matrices with elements with an absolute value less or equal to one, is the well-known *Hadamard's maximum determinant problem* [50]. It turns out that such (non-unique) matrix $\mathcal{H}_L$, called a *Hadamard matrix*, is known to exist on the real field for $L = 1, 2$, $L \equiv 0 (\mathrm{mod}\ 4)$, and its elements take the extreme values ±1.

For cases of L in which a Hadamard matrix does not exist, there may still be a D-optimum design matrix [42]. However, it is typically of more value to employ the closest $\mathcal{H}$-matrix [27], which is a non-square matrix $K \times L$ with $K > L$ that comprises elements of ±1, and satisfies $\mathcal{H}_{K\times L}^T \mathcal{H}_{K\times L} = K\mathcal{I}_L$, with $\mathcal{I}_L$ being the $L \times L$ identity matrix. Such matrices are D-optimum with respect to a $K \times L$ design with $\det(\mathcal{H}_{K\times L}^T \mathcal{H}_{K\times L}) = K^L$.

6.2.5 Unidirectional Designs

Here we fit a unidirectional MEGs sequence designs into the proposed framework. This is done in order to compare and evaluate the multidirectional designs that are presented next. This special case is also important as it shows that our framework allows estimation of the displacement map using a unidirectional design with a minimum of two acquisitions for each direction, as suggested in [166].

In order to apply only one MEG direction in each acquisition, we toggle the MEGs amplitudes as $|\mathcal{G}_i^{(k)}| = \{0, |\mathcal{G}_i|\}$. We follow the result of [166], which states that a minimal error with respect to sampling of the phase images is attained with evenly distributed acquisitions (in each direction) over the $[0, \pi)$ range for two acquisitions per direction. Thus, we limit our choice to $\alpha_i^{(k)} = \{0, \frac{\pi}{2}\}$. Finally, we choose zero start phases $\beta_i^{(k)} = 0$.

We therefore define a unidirectional design with a minimum of six acquisitions as

$$\begin{aligned}
&|\mathcal{G}_x^{(1,\ldots,6)}| = (|\mathcal{G}|, |\mathcal{G}|, 0, 0, 0, 0) \\
&|\mathcal{G}_y^{(1,\ldots,6)}| = (0, 0, |\mathcal{G}|, |\mathcal{G}|, 0, 0) \\
&|\mathcal{G}_z^{(1,\ldots,6)}| = (0, 0, 0, 0, |\mathcal{G}|, |\mathcal{G}|) \\
&\alpha_i^{(1,\ldots,6)} = (0,\ \pi/2,\ 0,\ \pi/2,\ 0,\ \pi/2)\ , \quad i = x, y, z \\
&\beta_i^{(1,\ldots,6)} = 0\ , \quad i = x, y, z
\end{aligned} \tag{6.11}$$

This sequence design, referred to as reduced motion encoding (RME) MRE in [166], is illustrated in Figure 6.2, and by (6.6) it yields a simple diagonal design matrix

$$\mathcal{M}_{\text{rme}} = \frac{\gamma\pi N|\mathcal{G}|}{\omega_m}\mathcal{I}_6\ , \quad \text{with } \left[\det\left(\mathcal{M}_{\text{rme}}^T\mathcal{M}_{\text{rme}}\right)\right]^{\frac{1}{2}} = \left(\frac{\gamma\pi N|\mathcal{G}|}{\omega_m}\right)^6 \tag{6.12}$$

For unidirectional designs that comprise more than two acquisitions per direction, [166] shows that α_i should be evenly distributed over the $[0, 2\pi)$ range in each direction. Similar to (6.11), we can construct such sequences and compute their design matrices. We consider a conventional design of 24 acquisitions (8 in each direction) for our evaluation and denote its design as $\mathcal{M}_{\text{con}}$. We note that by explicitly writing the proposed least-squares solution in (6.9) for $\mathcal{M}_{\text{con}}$, it can be shown that the estimated wave properties, $|\xi_i|$ and φ_i, using our time-domain approach coincide with the results achieved by a standard DFT processing of the phase images, in which $|\xi_i|$ and φ_i are estimated by the amplitude and phase of the fundamental frequency.

6.2.6 Multidirectional RME Design

Here we are interested in generating a multidirectional MEGs sequence that takes advantage of the parameterized approach in order to reduce estimation error. We note that employing different phase shifts $\alpha_i \neq \alpha_j$, in two directions or more, increases the TE of the acquisition so as to cover the entire MEGs sequence, which decreases SNR due to a weaker signal. The TE is measured based on the union of the time the MEGs are applied in a single acquisition, rather than from $t = 0$, therefore TE is still minimal even if $\alpha_i \neq 0$, as long as it is the same in all directions.

In addition, employing a start phase $\beta_i \neq \{0, \pi\}$ produces discontinuities in the MEGs waveform. In practice, gradient amplifiers impose a finite slew rate, and limitations on specific absorption rate restrict excessive dB/dt. This introduces errors to the phase accumulation calculation that lead to estimation errors in the displacement. The effect of a

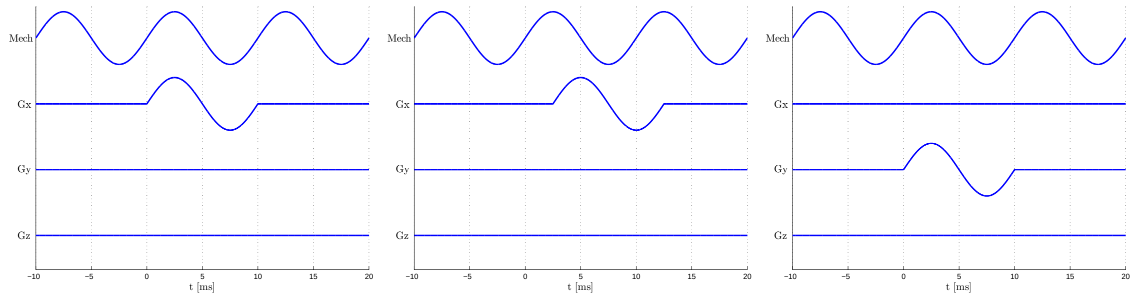

(a) Acquisition 1 (b) Acquisition 2 (c) Acquisition 3

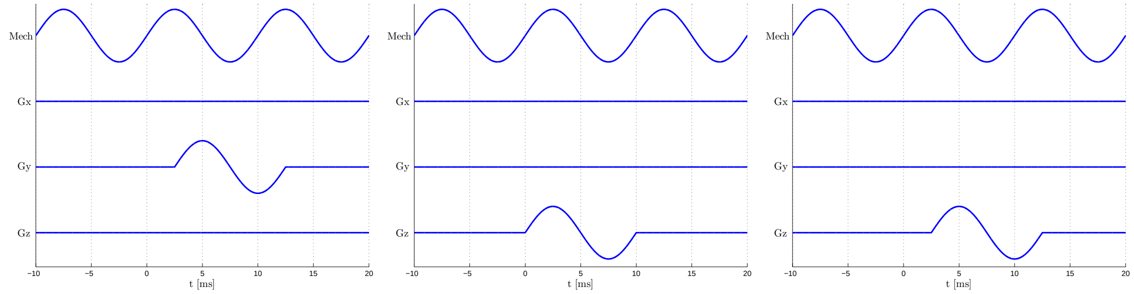

(d) Acquisition 4 (e) Acquisition 5 (f) Acquisition 6

Figure 6.2: RME design. Comprises a minimum number of unidirectional acquisitions.

finite slew rate on the sequence can be observed in Figure 6.1.

Thus, in this example we add to the optimal design problem in (6.10) the constraints $\beta_i = \{0, \pi\}$ and $\alpha_i = \alpha$, $\forall i = x, y, z$. We propose the following design with sign-flips

$$\begin{aligned}
\alpha_i^{(1,\ldots,6)} &= (0,\ \pi/2,\ 0,\ \pi/2,\ 0,\ \pi/2)\ , \quad i = x, y, z \\
\beta_x^{(1,\ldots,6)} &= (\pi,\ \pi,\ 0,\ 0,\ 0,\ 0) \\
\beta_y^{(1,\ldots,6)} &= (0,\ 0,\ \pi,\ \pi,\ 0,\ 0) \\
\beta_z^{(1,\ldots,6)} &= (0,\ 0,\ 0,\ 0,\ \pi,\ \pi) \qquad (6.13)
\end{aligned}$$

Since it comprises the minimum number of acquisitions, we refer to it as a multidirectional reduced motion encoding (MD-RME) design. The sequence is illustrated in Figure 6.3, and yields a Toeplitz design matrix

$$\mathcal{M}_{\text{md-rme}} = \frac{\gamma\pi N|\mathcal{G}|}{\omega_m}\begin{pmatrix} -1 & 0 & 1 & 0 & 1 & 0 \\ 0 & -1 & 0 & 1 & 0 & 1 \\ 1 & 0 & -1 & 0 & 1 & 0 \\ 0 & 1 & 0 & -1 & 0 & 1 \\ 1 & 0 & 1 & 0 & -1 & 0 \\ 0 & 1 & 0 & 1 & 0 & -1 \end{pmatrix},$$

$$\text{with } \left[\det\left(\mathcal{M}^T_{\text{md-rme}}\mathcal{M}_{\text{md-rme}}\right)\right]^{\frac{1}{2}} = 16\left(\frac{\gamma\pi N|\mathcal{G}|}{\omega_m}\right)^6 \tag{6.14}$$

Thus, for the same minimum number of acquisitions, the determinant value of the estimation covariance is reduced by a factor of 16 in comparison with the unidirectional RME sequence. We note that, since we are interested in the estimation error of each couple of coefficients, A_i, B_i, we should look at the elements in the diagonal of the inverse information matrix $(\mathcal{M}^T_{\text{md-rme}}\mathcal{M}_{\text{md-rme}})^{-1}$ that correspond to the variances of each coefficient. We find that these elements are half of their value in the unidirectional RME case, thus we expect the STDV of the estimation error to be reduced by $\sqrt{2}$ using the MD-RME sequence.

6.2.7 Optimal Design with Varying Start Phases

Here, rather than proposing a sequence and evaluating its performance, we take the inverse approach where we find a design that produces an optimal acquisition matrix. In our case $L = 6 \equiv 2 (\text{mod } 4)$, a Hadamard matrix does not exist, and the closest $\mathcal{H}$-matrix is for $K = 8$. Any such (non-unique) matrix can be chosen, and, using the technique in [42], we constructed

$$\mathcal{H}_{8,6} = \begin{pmatrix} 1 & 1 & -1 & 1 & -1 & -1 & 1 & -1 \\ 1 & 1 & 1 & -1 & -1 & -1 & -1 & 1 \\ 1 & -1 & 1 & 1 & -1 & 1 & -1 & -1 \\ 1 & 1 & -1 & 1 & 1 & 1 & -1 & 1 \\ 1 & 1 & 1 & -1 & 1 & 1 & 1 & -1 \\ 1 & -1 & 1 & 1 & 1 & -1 & 1 & 1 \end{pmatrix}^T \tag{6.15}$$

Given constant gradient amplitude and number of periods, the matrix $\mathcal{H}_{8,6}$ suggests that $\delta_i^{(k)} = \{-3\pi/4, -\pi/4, \pi/4, 3\pi/4\}$. The technique to determine $\delta_i^{(k)}$, for each acquisition k and direction i, is to observe the pair of elements $(k, 2i-1)$, $(k, 2i)$. Based on (6.6), these elements are proportional to $\cos(\delta_i^{(k)})$ and $\sin(\delta_i^{(k)})$, respectively. Thus, the value of

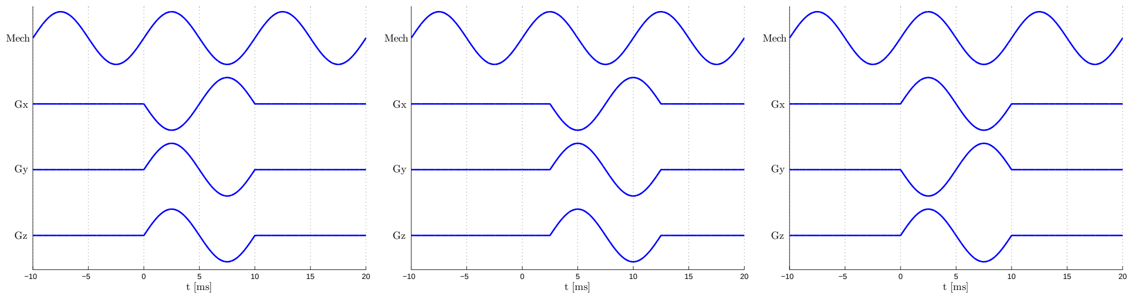

(a) Acquisition 1 (b) Acquisition 2 (c) Acquisition 3

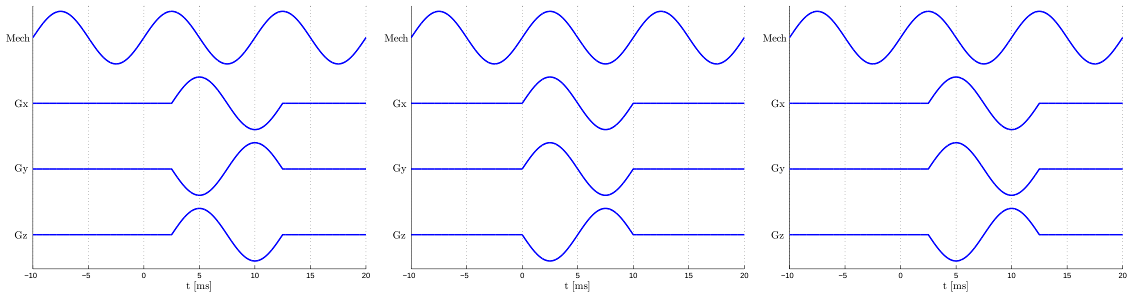

(d) Acquisition 4 (e) Acquisition 5 (f) Acquisition 6

Figure 6.3: MD-RME design. Comprises a minimum number of multidirectional acquisitions, without discontinuities in the MEGs or increase in TE.

$\delta_i^{(k)}$ is determined by the quadrant defined by these elements (e.g., the pair $(1, -1)$ yields $\delta = -\pi/4$).

We can derive several sequences that produce $\mathcal{H}_{8,6}$. Here, in order to minimize TE, we are interested in having no phase shift between directions, i.e., $\alpha_i^{(k)} = \alpha^{(k)}$, $\forall i = x, y, z$. It can be proved that no combination with only $\beta_i^{(k)} = \{0, \pi\}$ can produce $\mathcal{H}_{8,6}$. Thus, we are forced to have discontinuities in the MEGs in this case, and in order to minimize the slew rate effect we use $\beta_i^{(k)} = \{0, \pi\}$ when possible.

We propose the following sequence

$$\begin{aligned}
\alpha_i^{(1,\ldots,8)} &= (\frac{\pi}{4},\ \frac{3\pi}{4},\ \frac{3\pi}{4},\ \frac{3\pi}{4},\ \frac{5\pi}{4},\ \frac{5\pi}{4},\ \frac{5\pi}{4},\ \frac{3\pi}{4})\ , \quad i = x, y, z \\
\beta_x^{(1,\ldots,8)} &= (0,\ \frac{\pi}{2},\ 0,\ \pi,\ 0,\ 0,\ \frac{3\pi}{2},\ 0) \\
\beta_y^{(1,\ldots,8)} &= (0,\ 0,\ \pi,\ \frac{\pi}{2},\ \frac{\pi}{2},\ \pi,\ 0,\ 0) \\
\beta_z^{(1,\ldots,8)} &= (0,\ \pi,\ \frac{\pi}{2},\ 0,\ \pi,\ \frac{3\pi}{2},\ \pi,\ 0) \qquad (6.16)
\end{aligned}$$

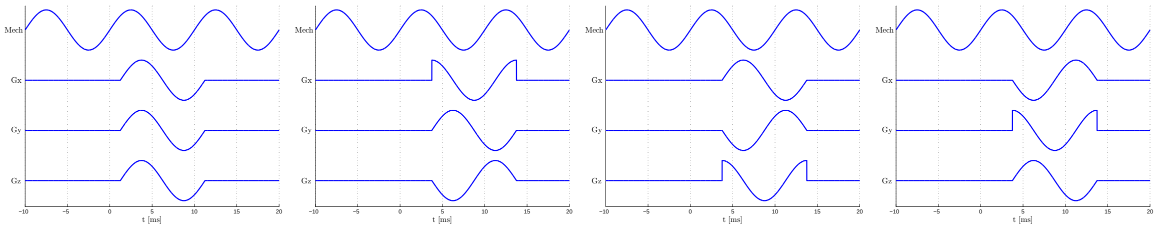

(a) Acquisition 1 (b) Acquisition 2 (c) Acquisition 3 (d) Acquisition 4

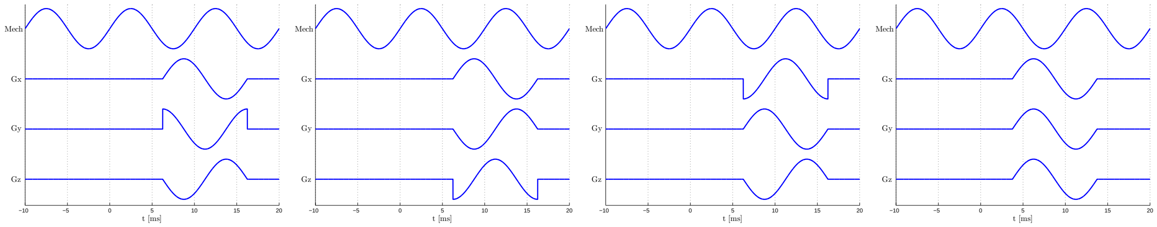

(e) Acquisition 5 (f) Acquisition 6 (g) Acquisition 7 (h) Acquisition 8

Figure 6.4: Optimal design with varying start phases. Notice the discontinuities in the MEGs. Using phase shifts we achieve discontinuity of only one direction per acquisition, without increase in TE.

The sequence is illustrated in Figure 6.4, and yields the design matrix

$$\mathcal{M}_{\text{opt}} = \frac{\gamma\pi N|\mathcal{G}|}{\sqrt{2}\omega_m}\mathcal{H}_{8,6}\ \text{, with}\ \left[\det\left(\mathcal{M}_{\text{opt}}^T\mathcal{M}_{\text{opt}}\right)\right]^{\frac{1}{2}} = 64\left(\frac{\gamma\pi N|\mathcal{G}|}{\omega_m}\right)^6 \tag{6.17}$$

Note we have a $1/\sqrt{2}$ loss (cosine and sine of multiples of $\pi/4$), but the overall gain of 64 of the optimal design compared to the RME design is still significant. By looking at the diagonal of the inverse information matrix, we find that its elements are 0.25 of their value in the RME case, thus we expect the STDV of the estimation error to be reduced by 2 by the optimal design.

Remember that we have used 8 acquisitions for this design, rather than 6 as in the previous designs. In case we employ 8 acquisitions of an RME sequence (by replicating two acquisitions), we have that the optimal design has a gain of 32 relative to such a design. In fact, the gain of this optimal design with only 8 acquisitions equals the gain of the conventional design $\mathcal{M}_{\text{con}}$, which comprises 24 acquisitions.

6.2.8 Optimal Design with Varying Phase Shifts

In the previous optimal design, the single discontinuity in some acquisitions may hinder its usage in practice due to a limited slew rate. In addition, as pointed out in [72], different start phases may affect the SNR in *in vivo* environments, since MEGs with different start phase have different flow compensation characteristics. Thus, here we propose a sequence with a start phase that is limited to $\beta_i^{(k)} = \{0, \pi\}$, but with different phase shifts $\alpha_i^{(k)}$ for each direction. Such multidirectional approach was proposed in [72] as sample interval modulation MRE to modulate the sampling interval such that the phase accumulation in each direction has a different frequency.

As described above, to yield the same optimal design as in (6.17), we derive the values of $\alpha_i^{(k)}$ such that $\delta_i^{(k)}$ are in the corresponding quadrants determined by $\mathcal{H}_{8,6}$. We propose the sequence

$$\begin{aligned}
\alpha_x^{(1,\ldots,8)} &= (\frac{\pi}{4},\ \frac{\pi}{4},\ \frac{3\pi}{4},\ \frac{3\pi}{4},\ \frac{\pi}{4},\ \frac{\pi}{4},\ \frac{3\pi}{4},\ \frac{3\pi}{4}) \\
\alpha_y^{(1,\ldots,8)} &= (\frac{\pi}{4},\ \frac{3\pi}{4},\ \frac{3\pi}{4},\ \frac{\pi}{4},\ \frac{3\pi}{4},\ \frac{\pi}{4},\ \frac{\pi}{4},\ \frac{3\pi}{4}) \\
\alpha_z^{(1,\ldots,8)} &= (\frac{\pi}{4},\ \frac{3\pi}{4},\ \frac{\pi}{4},\ \frac{3\pi}{4},\ \frac{\pi}{4},\ \frac{3\pi}{4},\ \frac{\pi}{4},\ \frac{3\pi}{4}) \\
\beta_x^{(1,\ldots,8)} &= (0,\ 0,\ 0,\ \pi,\ \pi,\ \pi,\ \pi,\ 0) \\
\beta_y^{(1,\ldots,8)} &= (0,\ 0,\ \pi,\ 0,\ 0,\ 0,\ \pi,\ 0) \\
\beta_z^{(1,\ldots,8)} &= (0,\ \pi,\ 0,\ 0,\ 0,\ \pi,\ 0,\ 0)
\end{aligned} \tag{6.18}$$

The sequence is illustrated in Figure 6.5. As discussed in [72], a disadvantage of employing different phase shifts for each direction is an increase of TE. Using the combinations of $\alpha_i^{(k)}$ and $\beta_i^{(k)}$ above, the phase shifts between the directions in each acquisition are minimized such that the maximum phase shift is $\pi/2$, which translates into a TE increase by a quarter of the time period.

6.3 Methods

6.3.1 Simulation of a Plane Wave

We first test our approach by simulating a linearly polarized wave propagating through a 3-D volume of size $64 \times 64 \times 64$ that comprises a background with a spherical inclusion. The stiffer inclusion is associated with a higher propagation speed (lower wave number), and a lower displacement amplitude than the background. We have used a shear wave frequency as in the phantom experiment (200Hz), and chosen the propagation speeds ($\sim$ 10m/s), and amplitudes ($\sim 10\mu$m) to be of the same order of magnitude as in the phantom experiment below. The goal of this simulation is to validate the least-squares wave estimation

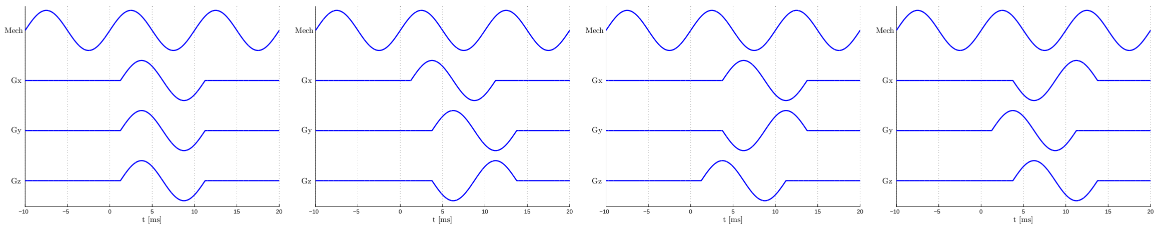

(a) Acquisition 1 (b) Acquisition 2 (c) Acquisition 3 (d) Acquisition 4

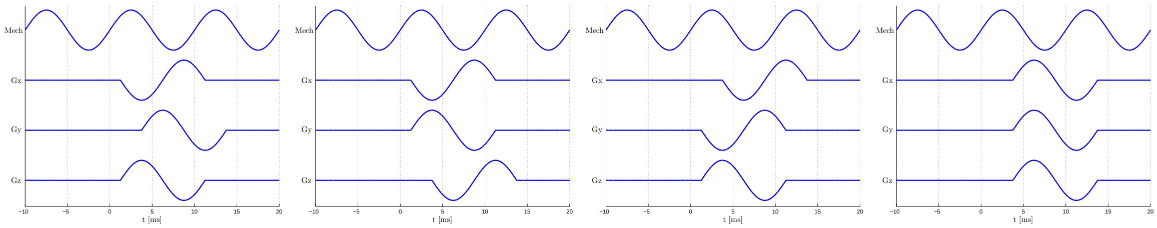

(e) Acquisition 5 (f) Acquisition 6 (g) Acquisition 7 (h) Acquisition 8

Figure 6.5: Optimal design with varying phase shifts. The maximum phase shift at each acquisition dictates the increase in TE. Using sign-flips, this phase shift is at most $\frac{\pi}{2}$.

framework, and theoretical performance analysis of the proposed designs.

We define a gradient sequence with the proposed parametrization of the MEGs, and compute the associated phase images for each acquisition by integrating the product of the wave and MEGs over time. Note that, in order to validate our analytical expression for the phase accumulation, we compute the integral numerically. To model the imaging noise, we add a zero mean Gaussian noise to each voxel of the phase images.

We repeat the simulations for the unidirectional RME, MD-RME and optimal designs proposed above, each with a range of noise variances. We calculate the coefficient vector $\hat{\mathcal{A}}$ by using the least-squares estimator, and derive the estimated amplitude and phase of the wave, $|\hat{\xi}_i|$, $\hat{\varphi}_i$ in each direction and for each voxel. Slices from the estimated volumes are shown in Figure 6.6.

Since we know the ground truth of the wave phases and amplitudes, we may compute the estimation error as the MSE between the estimations and the ground truth, i.e.,

$$\varepsilon_\xi^2 = \frac{1}{|\Omega|}\int_\Omega \sqrt{\sum_{i=x,y,z}\left(|\hat{\xi}_i(\bar{r})| - |\xi_i(\bar{r})|\right)^2}\, d\bar{r} \quad , \quad \varepsilon_\varphi^2 = \frac{1}{|\Omega|}\int_\Omega \sqrt{\sum_{i=x,y,z}\left(\hat{\varphi}_i(\bar{r}) - \varphi_i(\bar{r})\right)^2}\, d\bar{r} \tag{6.19}$$

where Ω and $|\Omega|$ are the volume and its size, respectively.

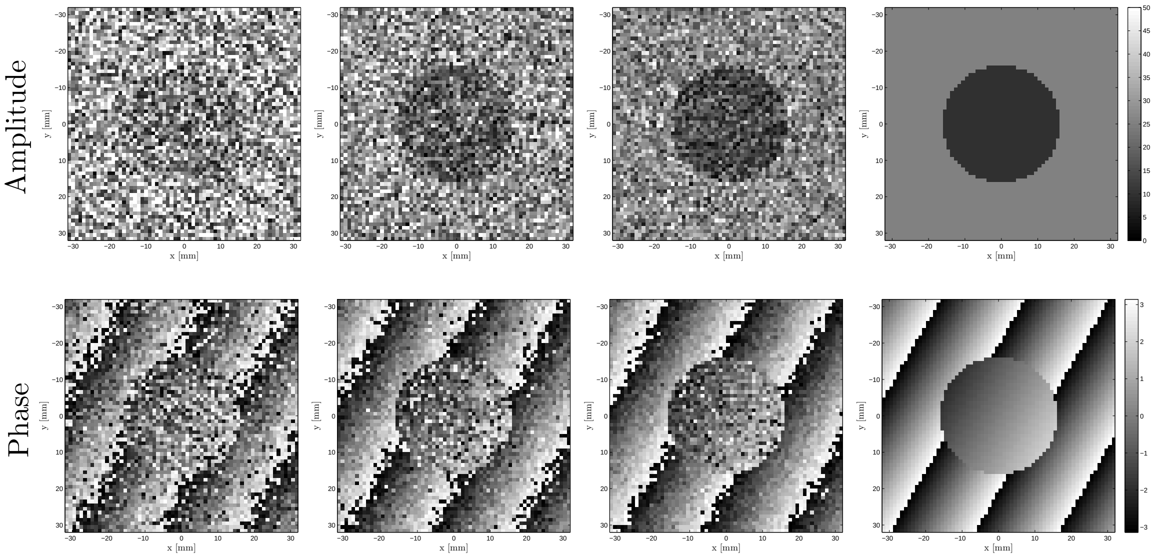

(e) RME (6 acquisitions) (f) MD-RME (6 acq.) (g) Optimal (8 acq.) or Conventional (24 acq.) (h) True

Figure 6.6: Simulation results. The estimated amplitude and phase of the wave using the unidirectional RME, MD-RME and optimal design with minimum acquisitions for a STDV of $\sigma = \pi/5$ of the noise added to the phase accumulation images. The conventional design yields similar results as the optimal design, but with three times the number of acquisitions. Top: The amplitude in the z-axis, intensity scale is in μm. Bottom: The phase in the z-axis (wrapped in $[-\pi, \pi)$), intensity scale is in rad.

6.3.2 Phantom Experiment

We have implemented the RME and the MD-RME sequences on a 3-Tesla system (Achieva 3.0T, Philips, The Netherlands) using a SE-EPI pulse sequence with a TE/TR of 30/1600 ms. A 200 Hz vibration was applied to a rectangular shaped elasticity phantom (Model 049, CIRS, VA, USA) using a custom-made shielded electromagnetic transducer synchronized to the scanner [135]. As seen in Figure 5.2(e), the phantom contains spherical inclusions of different radii and stiffness values relative to the background material that mimic different tissue types. The entire phantom was scanned in a field of view of $128 \times 128 \times 20$ grid, with an isotropic $2 \times 2 \times 2\text{mm}^3$ resolution. The scanning time was 364s per acquisition.

In order to evaluate our approach, we have oversampled the scan of each acquisition in both designs with the phase shifts of the MEGs ranging evenly over $[0, 2\pi)$ relative to the mechanical excitation. A $80 \times 60 \times 20$ region of interest on the acquired axial phase accumulation images was selected, compensated and phase unwrapped. We estimated the displacements using the proposed approach with a corresponding design. We have also gen-

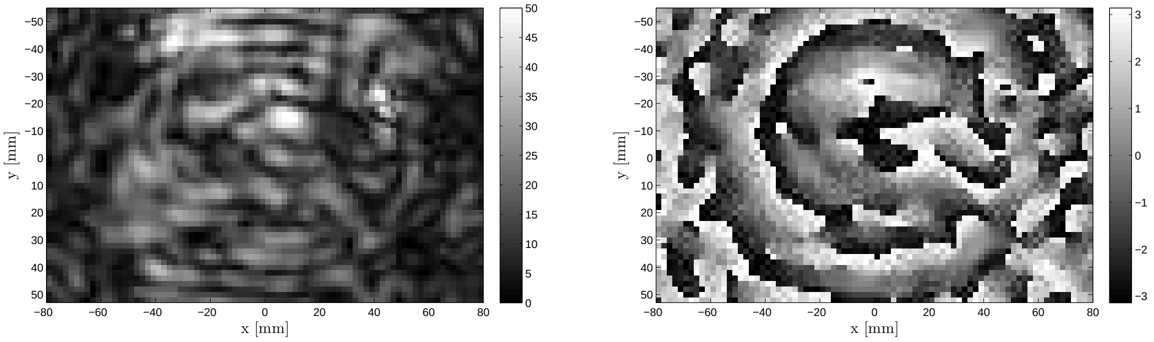

(a) Estimated wave amplitude (in μm)

(b) Estimated wave phase (in rad)

Figure 6.7: Phantom data. A cross-section of the best estimated amplitude and phase of the wave in the z-axis, as obtained by the least-squares approach over the entire set of acquisitions, and used as the “ground truth” for evaluation.

erated an elastogram using a LFE technique [85]. We note that these offline processing steps are performed in the same manner as in standard processing of MRE, with the exception of the displacement estimation that involves multiplications of matrices and inversion of the information matrix instead of the standard DFT computation (total processing times are similar).

We first estimated the displacements using the unidirectional and multidirectional designs with a minimum of 6 acquisitions each (RME and MD-RME). We then repeated for the 12 and 24 acquisition versions of the designs (where we refer to the unidirectional design with 24 acquisitions as the conventional MRE sequence), and evaluated the estimation errors in the amplitude, phase and elasticity. Since we do not have the ground truth of the displacements, we have employed the best estimation obtained by using our least-squares estimation approach over the entire set of acquisitions (i.e., a total of 8×6 acquisitions that include both unidirectional and multidirectional designs). A cross-section of this best estimation’s amplitude and phase is shown in Figure 6.7. The MSE of each design is computed using (6.19).

Further evaluation of the approach is performed by comparing the elastograms to the reported elasticity values of the phantom. We segmented the inclusions, and calculated the MSE between the reconstructed elastograms and the elasticity of each type of tissue over the corresponding region.

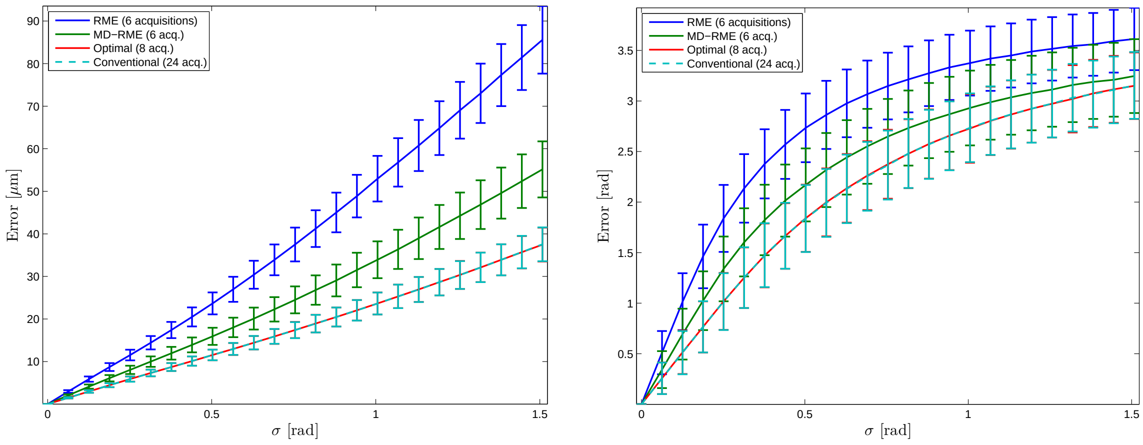

(a) Amplitude Error

(b) Phase Error

Figure 6.8: Simulation Errors. The MSE of the estimated amplitude and phase as a function of the STDV σ of the noise added to the phase accumulation images. The lines and bars represent the mean and half of the STDV of the error over all voxels, respectively.

6.4 Results

6.4.1 Simulation of a Plane Wave

The error plots as a function of the STDV σ of the noise are shown in Figure 6.8. We notice linear and nonlinear relationships between the STDV and the MSE of the amplitude and phase, respectively. As expected, the results using the conventional sequence with 24 unidirectional acquisitions coincide with those of the optimal sequence with 8 acquisitions.

By dividing the amplitude error plots, we find that the estimation errors of the RME design are reduced by 1.51 ± 0.04 and 2.03 ± 0.06 using the MD-RME and optimal designs, respectively. Similar slope ratios were computed for the phase error plots in the linear region that corresponds to small values of STDVs. These results fit the theoretical error reductions of $\sqrt{2}$ and 2 in the estimation of the coefficients, to which, by (6.4), the amplitude and phase are proportional linearly and nonlinearly.

6.4.2 Phantom Experiment

The quantitative results are summarized in Table 6.2. The *ratio* between the amplitude estimation errors of the unidirectional and the multidirectional with sign-flips designs for the 6, 12 and 24 acquisitions experiments were 4.05, 1.19 and 1.47, respectively. Thus, the error reductions by the multidirectional designs are close to the theoretical $\sqrt{2}$ value that was calculated from the information matrices, and in the 6 acquisitions case significantly

	Unidirectional designs			Multidirectional designs		
	6 Acq. (RME)	12 Acq.	24 Acq. (Conventional)	6 Acq. (MD-RME)	12 Acq.	24 Acq.
Amplitude Error (μm)	46.6 ± 33.9	2.2 ± 1.8	2.1 ± 1.7	11.5 ± 8.3	1.8 ± 1.5	1.4 ± 1.1
Phase Error (rad)	1.4 ± 0.9	0.4 ± 0.4	0.3 ± 0.4	0.9 ± 0.8	0.2 ± 0.3	0.2 ± 0.3
Elasticity Error (kPa)	29.6 ± 22.6	3.81 ± 3.3	3.7 ± 3.1	14.9 ± 13.1	2.6 ± 2.2	1.7 ± 1.5

Table 6.2: Phantom results. Estimation errors in comparison with the best estimate obtained by the entire set of acquisitions.

surpasses it.

The elastograms that were reconstructed based on the unidirectional and multidirectional designs for 6, 12 and 24 acquisitions are illustrated in Figure 6.9. The corresponding errors in comparison with the factory reported elasticity are presented in Figure 6.10. We notice that, as expected, the more acquisitions we have, the closer are the elasticity values to their factory values. Also, on average, the values generated from the multidirectional design are closer to their reported values.

6.5 Discussion and Conclusion

In this chapter we have presented a framework for motion encoding design in MRE. The approach was tested and evaluated using simulation and experiments on a phantom. The simulation confirms that optimal sequences have the potential of reducing the number of acquisitions required by unidirectional MRE up to a factor of three while acquiring images with the same SNR. Alternatively, for the same number of acquisitions, the estimation error of displacement amplitude can be reduced up to a factor of two. The produced elastograms are also more accurate, since reconstruction is positively correlated with the accuracy of the displacement input.

A simplified analogy of the problem is the Yates-Hotelling weighing problem, in which it was shown that by using the same number of weighings, individual weights of objects can be estimated better by weighing them in combinations, rather than separately [96]. Here, each acquisition is considered a “weighing,” the measured phase accumulation are the “scale readings,” and using the MEGs parameters we assign each direction a “pan on the scale” or exclude it.

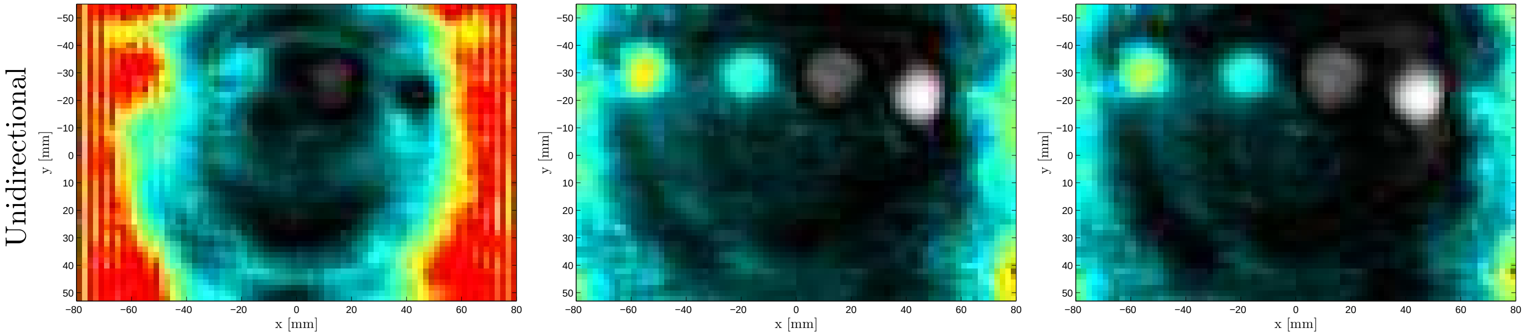
Unidirectional
y [mm]
−50
−40
−30
−20
−10
0
10
20
30
40
50
x [mm]
−80
−60
−40
−20
0
20
40
60
80

(a) RME (6 acquisitions)

(b) 12 Acquisitions

(c) Conventional (24 Acq.)

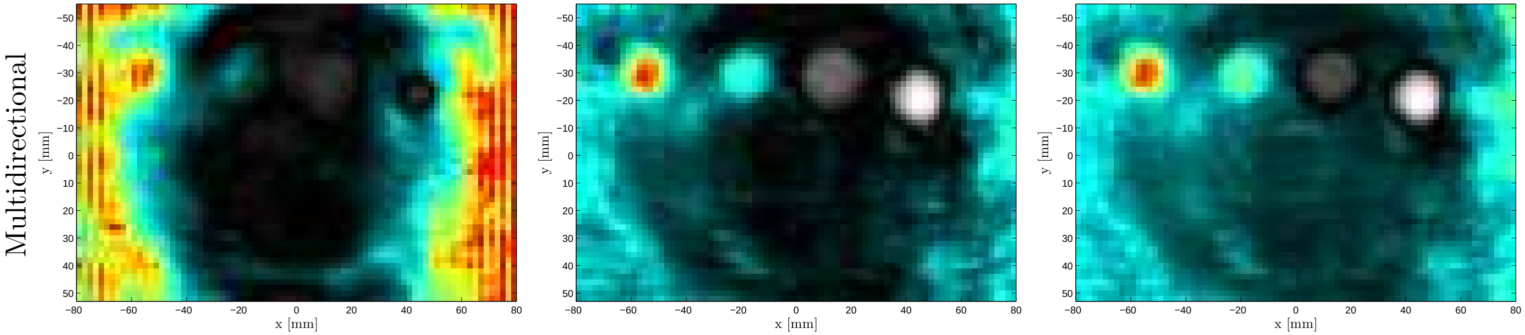
Multidirectional
y [mm]
−50
−40
−30
−20
−10
0
10
20
30
40
50
x [mm]
−80
−60
−40
−20
0
20
40
60
80

(d) MD-RME (6 acquisitions)

(e) 12 Acquisitions

(f) 24 Acquisitions

Figure 6.9: Phantom results. The elastograms (mean over three central slices) that were reconstructed from the estimated amplitude and phase of the wave with a different number of acquisitions. Top: Using the unidirectional design. Bottom: Using the multidirectional design. Intensity scale is in kPa and same as in Figure 5.2(e).

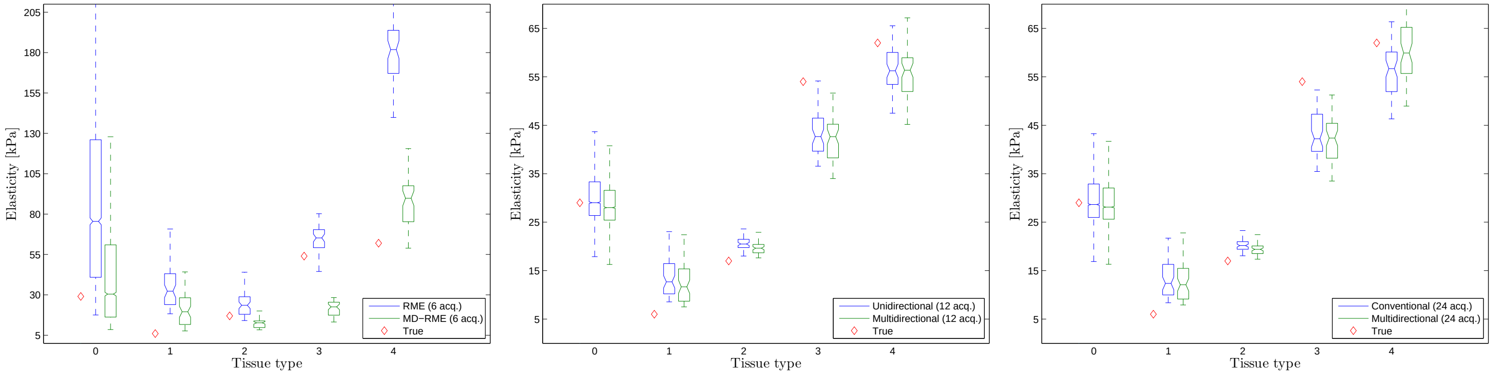

(a) 6 Acquisitions (b) 12 Acquisitions (c) 24 Acquisitions

Figure 6.10: Phantom elasticity errors. Errors between the elastograms of the unidirectional and multidirectional designs in comparison with the true elasticity on each tissue type.

With scanner limitations on the slew rate of the gradients, an optimal design with varying start phases may cause errors in phase accumulation by encoding higher frequency components. Alternative implementations of optimal designs that are not affected by the slew rate, but require longer TE, can be achieved with varying phase shifts as proposed in [72]. Indeed, our framework shows that the sequence in [72] yields an optimal design under the noise model and optimality criterion we assumed, and their DFT approach coincides with the proposed least-squares solution.

Thus, in practice, we have a trade-off of SNR gain by using an optimal design versus SNR loss by lower gradient amplitudes or longer TE. Currently, the MD-RME design and its extension to 12 and 24 acquisitions with sign-flips provide the best of both worlds and are straightforward to implement. Specifically, the 12 acquisition sign-flips sequence attains the same estimation errors compared to a conventional sequence of 24 acquisitions, with half of the acquisition time.

We are also looking into additional parametrization of the acquisition design within our framework. A potential approach is to employ multidirectional fractional encoding ratios [173]. In the Appendix, we extend the parameterized phase accumulation for this case, in which the MEG frequency is higher than the mechanical frequency, and may vary in each direction and acquisition. This may allow derivation of optimal designs without discontinuities in the MEGs and an increase of TE. However, this also affects the encoding efficiency and therefore requires changing the gradient amplitudes in (possibly) large factors to compensate each direction, which may hinder the use of this approach in practice.

We limited our experiments to employ SE-EPI sequences. However, other pulse sequences in the literature, e.g., [44], can be employed to further improve SNR and/or shorten acquisition time. Trapezoidal waveform can also be applied rather than sinusoidal, to maximize encoding efficiency under limitation of the slew rate. Note that applying multidirectional MEGs introduces concomitant-field terms that should be corrected, e.g., by using gradient symmetrization [14]. In the sequences we use, the MEGs are mirrored after the echo pulse and cancel such effects.

We note that modeling the noise in the phase images as white Gaussian noise is justified by the fact that the least-squares solution for the conventional sequence using our approach coincides with the standard DFT processing. Thus, such noise has been implicitly assumed so far in MRE imaging. However, in practice, it might not be the case due to, e.g., change in temperature of the coils between measurements. An advantage of our framework is that we may employ a different noise model with its proper optimal estimator (e.g., weighted least-squares [18]). In addition, optimality criteria other than D-optimality can be considered for evaluating design performance. Our approach may allow to adapt the acquisition matrix accordingly by, e.g., using non-uniform sampling of the acquisitions. The flexibility in shaping the matrix may also be important in incorporating compressed sensing in MRE.

In conclusion, the formulation of motion encoding as both linear estimation and optimal design problems allows employing tools from fields such as optimization, statistics and information theory. A careful design of parameterized multidirectional MEGs yields displacement maps with a better SNR and/or shorter acquisition times. Along with the ongoing improvement in transducers and reconstruction algorithms, accurate elastograms that characterize the mechanical properties of *in vivo* tissue can be derived. In turn, these may pave the way for a broader clinical deployment of MRE.

Chapter 7

Conclusion

In this thesis we have developed algorithms for registration of the prostate in different modalities. Specifically, we considered registration of histopathology of excised prostate specimens with their volumetric MR and US imaging, and registration of preoperative MRI to intraoperative TRUS imaging of the prostate during RALP. The former registration can be applied for training classifiers in order to allow an automatic localization of CaP. The latter registration can be applied to augment the surgeon's console with the preoperative MR image that corresponds to the da Vinci instrument's tooltip, and, combined with a classifier, a corresponding CaP probability map.

We have also studied the reciprocity between registration and MRE, and showed that by utilizing the properties of the registration and elastography acquisition process, MRE can facilitate registration, and *vice versa*. The results of the research presented in the various chapters complement each other, and are intended to be jointly applied as depicted by the diagram in Figure 7.1 and described below.

First, by employing the optimization-based designed motion encoding sequences during a preoperative MRI scanning session, as proposed in Chapter 6, the quality of the acquired MRE data is increased, and/or scanning time (and therefore costs and discomfort to the patient) is reduced. Estimation of the MRE elastograms can be further enhanced or corrected by employing the motion compensation and super-resolution technique discussed in Chapter 5.

In turn, the enhanced elastograms provide accurate biomechanical models of the prostate and periprostatic tissue in preoperative *in vivo* MRI, which may improve the accuracy of its registration to the corresponding postoperative *ex vivo* MRI using the deformable registration method developed in Chapter 3. By composing the resulting deformation map with the transformation between the histological slices and *ex vivo* MRI, as computed using the particle filtering algorithm developed in Chapter 2, we obtain an accurate mapping between histopathology and *in vivo* MRI that can train a classifier for localization of CaP. Finally, during future RALP procedures, a reliable classifier will allow a CaP probability map to be overlaid on MR images that correspond to the robot's tooltip by employing the MRI to TRUS registration algorithm proposed in Chapter 4.

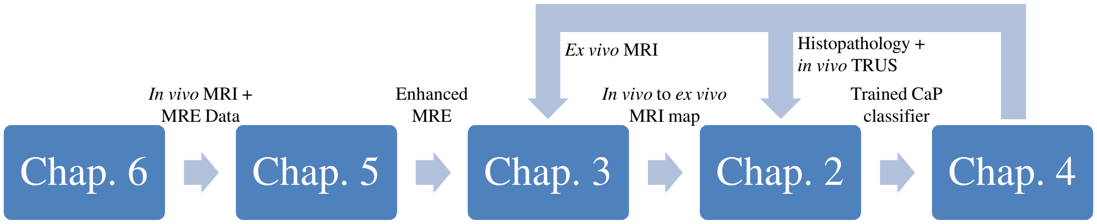

Figure 7.1: Proposed clinical flow.

We note that the data collection that was employed in this thesis was acquired either prior or in parallel to development of the methods, and follows protocols that were set and approved in advance. In retrospect, the multi-parametric MRI settings could have been set to produce images that are, e.g., better correlated with histology, or of higher resolution. Nevertheless, our methods were designed and adapted to contend with the typical data acquired by practical and clinical protocols.

The clinical significance of the research conducted throughout this thesis is that, with MRI correctly displayed on the surgeon's console and automatic localization of CaP, resection of the prostate during RALP can be carried out with minimal damage to adjacent structures. Due to the increasing usage of RALP worldwide, even a slight improvement by using the proposed methods can impact treatment outcomes of thousands of CaP patients. The proposed methods can also benefit other CaP treatments such as image guided biopsy, brachytherapy, and watchful waiting. In addition, the time reduction in acquisition of MRE data increases its potential in clinical deployment.

The main scientific significance lies in the novel registration methods, the usage and study of elastography in registration, and the established interface between MRE acquisition and information theory. Below, we summarize the main contributions that were made in the course of achieving the thesis objectives, describe the limitations, and discuss possible future research directions.

7.1 Contributions and Limitations

Registration of Whole-Mount Histology and Volumetric Imaging:

In Chapter 2, we developed a general framework for multi-slice to volume registration that is applied to align histopathology with volumetric MR and US imaging of the prostate. The registration is formulated as a filtering problem, which allows prior knowledge regarding the physical misalignment mechanisms to be incorporated into the framework in a Bayesian fashion. We also implemented an accompanying visualization tool allows comparison of each histological slice side-by-side with corresponding slices from two other modalities, and yield the intensity histograms of these slices on user selected points, lines and regions.

The registration of histological slices to *ex vivo* MR, *in vivo* MR, and *in vivo* US achieved relatively high area overlaps and registration errors below the diameter of typical lesions that are marked during histopathology analysis ($\sim 10 \pm 5$ mm [34]). The registration is therefore being utilized in ongoing studies to optimize and evaluate CaP detection on a range of imaging modalities. These studies have yielded several publications ([95, 98, 137, 138]) that characterize cancer on US, TRUS-VE, and on both *in vivo* and *ex vivo* MRI and MRE.

The main limitation of the proposed method, which stems from its generality, is the relative high number of parameters that need to be set. These parameters can be chosen by a trial-and-error process on a few training cases. In addition, the registration time may be long when using intensity- or region-based metrics, whereas the point-based metric requires an additional segmentation of the volumetric images. Nevertheless, longer running times are tolerable in histology processing as the algorithm is running offline, and segmentation errors can be taken into account by modeling of the noise in the filtering formulation.

Model-Based Registration Using Elastography:

In Chapter 3, we developed and implemented an algorithm for deformable registration of *ex vivo* and *in vivo* MRI. By allowing a two-step registration with the *ex vivo* MR as an intermediate modality, this algorithm can be integrated with the multi-slice to volume alignment above in order to capture the residual deformations between histological slices and *in vivo* MR.

The method presents the first utilization of measured *in vivo* elasticity by MRE for improving deformable registration. The MRE elastogram is incorporated into the registration framework as a biomechanical model that regularizes the deformation according to physical inhomogeneous elasticity. By studying the effect of inhomogeneity in elasticity on registration errors, we have showed that this approach yields improved registration as opposed to applying a constant elasticity value to the volume, and that, in general, the performance improves with the inhomogeneity of elasticity inside and outside of the prostate. We have also proposed a novel similarity metric that does not require segmentation and meshing of the *in vivo* anatomy, as opposed to explicit FEM-based modeling approaches.

As in other studies that concern deformable registration methods, the ground-truth deformation map is unknown and the results are being evaluated on a sparse set of landmarks and volume overlaps. Another limitation of our study is that the choice of landmarks and segmentations were performed once by one expert, thus we do not have intra- or interobserver variability measurements. Such information would have allowed evaluation of whether the lower accuracy for base and apex stems from the registration itself or from segmentation inaccuracy. A disadvantage of the proposed approach is that the *ex vivo* MRI scan is time consuming and expensive. In addition, current *in vivo* MRE protocols also involve longer scanning time, inconvenience to the patient, and are still not widely accessible. This limitation may be mitigated by the results of Chapter 6.

Registration of Ultrasound and Magnetic Resonance Imaging for Image Guided Interventions:

In Chapter 4, we developed a feasible method for introducing MRI data in the operating room, by registering preoperative MRI to intraoperative TRUS. The proposed approach can employ existing building blocks to enable tracking and display of the MR image that corresponds to the da Vinci instrument's tooltip during RALP. The segmentation-based approach deforms the segmented T2w volume to match its surface with that of an intraoperatively segmented B-mode. The registration is fast and robust, while its performance was found to be plausible, with results comparable to other TRUS-MR registration methods.

A limitation of the proposed approach is that, as in other segmentation-based methods, the quality of the registration depends on the quality of the segmentation. Another limitation is that the registration is only valid with respect to the time the TRUS volume was acquired, thus rendering its usage during later stages of the surgery challenging.

We have also studied the usage of elastography as an inter-modality for registering TRUS and MRI. While we found the elasticity values to be nondescriptive for a deformable intensity-based registration, the phantom and four clinical data sets we used are statistically insufficient to conclude that. Typically, in studies that evaluate new registration methods, data sets in the range of 10-20 patients are being used. However, the required sample size for drawing a statistically significant conclusion in our case should be determined by setting the desired statistical power and significance level, and using power-analysis tools [77].

Motion Compensation and Super-Resolution in MRE:

In Chapter 5, we turned to employ registration for enhancing MRE data. Magnitude images, which are often regarded as a by-product of the MRE acquisition process and ignored, are utilized to compensate for motion of patients during the, typically lengthy, acquisition process. The inherent alignment of the magnitude and phase images allows for the enhancement of elastogram reconstruction by employing a super-resolution technique that increases the resolution of the corresponding registered phase images.

The main contribution in this work is the improvement of existing MRE data by using image processing techniques without altering the current data acquisition protocol. This is possible due to observation and utilization of the redundancy in the data acquired in MRE. We noticed a better separability of objects from their background on the reconstructed higher resolution elastograms in comparison with the native resolution ones.

We note, however, that assuming a Gaussian blurring kernel in the super-resolution technique is inaccurate, and a model of the actual point spread function of the scanner is required in order to yield accurate reconstructions of the high resolution images. In addition, [35] suggested that the highest resolution increase in each axis using two images (each pair of phase images in our case) is by $\sqrt{2}$. Thus, doubling the resolution based on [61] may introduce further inaccuracies to the super-resolution phase images and elastograms.

We also note that other MRI sequences that encode motion were not considered. Specifically, the harmonic phase (HARP) algorithm [110] is popular for detection and tracking cardiac motion using tagged MRI. However, tagged MRI sequences, which employ RF to encode motion, are slower than MEGs and typically do not allow capturing motion in frequencies high enough for dynamic elastography.

Optimization-Based Design of Motion Encoding in MRE:

In Chapter 6, we proposed a general framework for improving MRE acquisition by optimizing designs of the motion encoding process. The framework lays the groundwork for formulating the MRE acquisition problem within fields such as optimization, statistics and information theory, and thus allows employing established tools from these fields for quantification of design performance and derivation of optimal sequences by different criteria.

Generalization and parametrization of the MEGs were introduced, and by using the proposed framework we derived and implemented a multidirectional sequence with a minimum number of acquisitions that does not require an increase in TE, nor discontinuities in the MEGs. The reduced acquisition time and improved data quality that is achieved by the proposed approach may assist in bringing MRE to broader use.

While multidirectional MEGs allow minimization of the variance in motion estimation error, estimations among the different directions become correlated. Thus, if the scanner has inhomogeneity along one direction, the motion estimations in all directions are affected, rather than just the corresponding direction. Physical limitations such as concomitant-field terms should be taken into account when employing multidirectional gradients. In addition, hardware issues or overheating of the coils may limit the maximum gradient amplitude or require cooling down periods between acquisitions of multidirectional sequences.

7.2 Future Work

Based on the results of this thesis, the main future work is to conduct a clinical study for evaluating the performance of the proposed MR-TRUS registration intraoperatively, and perform a cost-benefit analysis of using this approach during RALP, based on evidence and feedback from clinicians. In addition, the two-step registration between histological slices and *in vivo* MR that employs the *ex vivo* MR as an intermediate modality is to be used for training classifiers of CaP. Other possible future research directions that may further improve or extend the proposed methods are summarized below.

Registration of Whole-Mount Histology and Volumetric Imaging:

- Incorporation of a nonrigid registration step in order to improve registration of histology and *in vivo* imaging. Due to the sparsity of slices, a 2-D registration should be applied between each histological slice and its corresponding registered slice on the volumetric image.
- Investigation of other metrics that can describe the similarity between histological slices and volumetric imaging. Specifically, employing a point-based metric between descriptors of intensity-based extracted features.

Model-Based Registration Using Elastography:

- Derivation of forces through intensity-based similarity metrics between *in vivo* and *ex vivo* T2w MRI to eliminate the required segmentation of the *ex vivo* volume.
- Consider nonlinear elasticity to contend with large deformations of the prostate, e.g., in case of employing a transrectal coil during image acquisition.

Registration of Ultrasound and Magnetic Resonance Imaging for Image Guided Interventions:

- Allow a manual selection of corresponding points on MR and TRUS images that are used as anchor points to constrain the registration. This will provide the user with some control over the registration, and the ability to correct it in case the automatic results are not plausible.
- Allow switching the display between different MR images, e.g., diffusion weighted imaging or MRE, which were acquired during the multi-parametric preoperative MRI session, and can be co-registered to the T2w volume (and thus to the TRUS volume).

- Optimization of the code and its implementation on C/C++ to reduce running time, thus making the proposed approach more feasible in a clinical setting.
- Develop a tracking algorithm that allows real-time deformation of the registered MR according to the TRUS volume.
- Study other metrics and the extraction of features that may be better suitable for intensity-based registration of MRE and USE.

Motion Compensation and Super-Resolution in MRE:

- Iterative optimization of motion compensation and elasticity reconstruction, by applying the reconstructed elastogram in the current iteration as regularization for the motion compensation displacements in the next iteration.
- Incorporation of multi-frequency information for adding additional data to the super-resolution technique and improving displacement estimation.
- Considering blurring kernels in the super-resolution technique that model the point spread function of the scanner in order to improve the accuracy of the high resolution image.

Optimization-Based Design of Motion Encoding in MRE:

- Additional parametrization of the MEGs, e.g., including varying fractional encoding ratios in each direction, in order to increase the degrees of freedom in designs within our framework.
- Employment of the proposed framework to extend existing pulse sequences, e.g., [44], into multidirectional in order to maximize encoding efficiency under limitation of the slew rate.
- Employment of different noise models with corresponding optimal estimators.
- Employment of different optimality criteria for evaluating design performance.

Bibliography

[1] P. Abolmaesumi and M. R. Sirouspour. An interacting multiple model probabilistic data association filter for cavity boundary extraction from ultrasound images. *IEEE Transactions on Medical Imaging*, 23(6):772–784, 2004.

[2] T. K. Adebar, M. C. Yip, S. E. Salcudean, R. N. Rohling, C. Y. Nguan, and S. L. Goldenberg. Registration of 3D ultrasound through an air–tissue boundary. *IEEE Transactions on Medical Imaging*, 31(11):2133–2142, 2012.

[3] T. E. Ahlering, D. Woo, L. Eichel, D. I. Lee, R. Edwards, and D. W. Skarecky. Robot-assisted versus open radical prostatectomy: a comparison of one surgeon's outcomes. *Urology*, 63(5):819–822, 2004.

[4] N. Alpert, J. Bradshaw, D. Kennedy, and J. Correia. The principal axes transformation: a method for image registration. *Journal of Nuclear Medicine*, 31(10):1717–1722, 1990.

[5] R. Alterovitz, K. Goldberg, J. Pouliot, I. Hsu, Y. Kim, S. Noworolski, and J. Kurhanewicz. Registration of MR prostate images with biomechanical modeling and nonlinear parameter estimation. *Medical Physics*, 33:446, 2006.

[6] American Cancer Society. Cancer facts & figures 2014. `http://www.cancer.org/` (retrieved on April 18, 2014).

[7] E. R. Arce-Santana, D. U. Campos-Delgado, and A. Alba. Affine image registration guided by particle filter. *IET Image Processing*, 6(5):455–462, 2012.

[8] M. S. Arulampalam and *et al.* A tutorial on particle filters for online nonlinear/non-gaussian Bayesian tracking. *IEEE Transactions on Signal Processing*, 50(2):174–188, 2002.

[9] A. Baghani, A. Brant, S. Salcudean, and R. Rohling. A high-frame-rate ultrasound system for the study of tissue motions. *IEEE Transactions on Ultrasonics, Ferroelectrics and Frequency Control*, 57(7):1535–1547, 2010.

[10] A. Baghani, H. Eskandari, W. Wang, D. Da Costa, M. N. Lathiff, R. Sahebjavaher, S. Salcudean, and R. Rohling. Real-time quantitative elasticity imaging of deep tissue using free-hand conventional ultrasound. *Medical Image Computing and Computer Assisted Intervention (MICCAI)*, pages 617–624, 2012.

[11] R. Bajcsy and S. Kovacic. Multiresolution elastic matching. *Computer Vision Graphics and Image Processing*, 46:1–21, 1989.

[12] S. Bart, P. Mozer, P. Hemar, G. Lenaour, E. Comperat, R. Renard-Penna, E. Chartier-Kastler, and J. Troccaz. MRI-histology registration in prostate cancer. In *Surgetica*, pages 361–367, 2005.

[13] M. Baumann, P. Mozer, V. Daanen, and J. Troccaz. Prostate biopsy tracking with deformation estimation. *Medical Image Analysis*, 2011.

[14] M. A. Bernstein, X. J. Zhou, J. A. Polzin, K. F. King, A. Ganin, N. J. Pelc, and G. H. Glover. Concomitant gradient terms in phase contrast MR: analysis and correction. *Magnetic Resonance in Medicine*, 39(2):300–308, 1998.

[15] P. J. Besl and N. D. McKay. A method for registration of 3-D shapes. *IEEE Transactions on Pattern Analysis and Machine Intelligence*, 14(2):239–256, 1992.

[16] A. Bharatha et al. Evaluation of three-dimensional finite element-based deformable registration of pre-and intraoperative prostate imaging. *Medical Physics*, 28:2551, 2001.

[17] M. Bilgen and M. Insana. Predicting target detectability in acoustic elastography. *IEEE Ultrasonics Symposium*, 2:1427–1430, 1997.

[18] S. Boyd and L. Vandenberghe. *Convex Optimization.* Cambridge University Press, Cambridge UK, 2004.

[19] L. Breiman. Random forests. *Machine learning*, 45(1):5–32, 2001.

[20] C. Broit. *Optimal registration of deformed images.* PhD thesis, Computer and Information Science Dept., University of Pennsylvania, Philadelphia, PA, 1981.

[21] T. Brox and D. Cremers. On local region models and a statistical interpretation of the piecewise smooth mumford-shah functional. *International Journal of Computer Vision*, 84(2):184–193, 2009.

[22] V. Caselles, R. Kimmel, and G. Sapiro. Geodesic active contours. *International Journal of Computer Vision*, 22(1):61–79, 1997.

[23] T. F. Chan and L. A. Vese. Active contours without edges. *IEEE Transactions on Image Processing*, 10(2):266–277, 2001.

[24] J. Chappelow, B. Bloch, N. Rofsky, E. Genega, R. Lenkinski, W. DeWolf, and A. Madabhushi. Elastic registration of multimodal prostate MRI and histology via multiattribute combined mutual information. *Medical Physics*, 38(4):2005, 2011.

[25] G. E. Christensen, R. D. Rabbit, and M. I. Miller. Deformable templates using large deformation kinematics. *IEEE Transactions on Medical Imaging*, 5:1435–1447, 1996.

[26] A. Collignon, F. Maes, D. Delaere, D. Vandermeulen, P. Suetens, and G. Marchal. Automated multi-modality image registration based on information theory. In Y. Bizais, C. Barillot, and R. Di Paola, editors, *Information Processing in Medical Imaging*, pages 263–274. Kluwer Academic Publishers, Dordrecht Netherlands, 1995.

[27] W. A. Coppel. Hadamard's determinant problem. In *Number Theory*, pages 223–259. Springer, 2009.

[28] V. Daanen, J. Gastaldo, J.-Y. Giraud, P. Fourneret, J.-L. Descotes, M. Bolla, D. Collomb, and J. Troccaz. MRI/TRUS data fusion for brachytherapy. *The International Journal of Medical Robotics and Computer Assisted Surgery*, 2(3):256–261, 2006.

[29] C. Davatzikos. Spatial transformation and registration of brain images using elastically deformable models. *Computer Vision and Image Understanding*, 66:207–222, 1997.

[30] A. Doucet, N. de Freitas, and N. Gordon. *Sequential Monte Carlo Methods in Practice.* Springer, New York, 2001.

[31] A. Doucet and A. Johansen. A tutorial on particle filtering and smoothing: fifteen years later. *Handbook of Nonlinear Filtering*, pages 656–704, 2009.

[32] B. Drew, E. Jones, S. Reinsberg, A. Yung, S. Goldenberg, and P. Kozlowski. Device for sectioning prostatectomy specimens to facilitate comparison between histology and in vivo MRI. *Journal of Magnetic Resonance Imaging*, 32(4):992–996, 2010.

[33] R. O. Duda, P. E. Hart, and D. G. Stork. *Pattern Classification.* Wiley-Intersciance, New York, second edition, 2001.

[34] L. Eichelberger, M. Koch, J. Daggy, T. Ulbright, J. Eble, and L. Cheng. Predicting tumor volume in radical prostatectomy specimens from patients with prostate cancer. *American Journal of Clinical Pathology*, 120(3):386–391, 2003.

[35] M. Elad and A. Feuer. Restoration of a single superresolution image from several blurred, noisy, and undersampled measured images. *IEEE Transactions on Image Processing*, 6(12):1646–1658, 1997.

[36] J. I. Epstein, P. C. Walsh, M. Carmichael, and C. B. Brendler. Pathologic and clinical findings to predict tumor extent of nonpalpable (stage t1 c) prostate cancer. *The Journal of the American Medical Association (JAMA)*, 271(5):368–374, 1994.

[37] H. Eskandari, O. Goksel, S. E. Salcudean, and R. Rohling. Bandpass sampling of high-frequency tissue motion. *IEEE Transactions on Ultrasonics, Ferroelectrics and Frequency Control*, 58(7):1332–1343, 2011.

[38] M. Ferrant, A. Nabavi, B. Macq, F. Jolesz, R. Kikinis, and S. Warfield. Registration of 3-D intraoperative MR images of the brain using a finite-element biomechanical model. *IEEE Transactions on Medical Imaging*, 20(12):1384–1397, 2001.

[39] V. Ficarra, G. Novara, W. Artibani, A. Cestari, A. Galfano, M. Graefen, G. Guazzoni, B. Guillonneau, M. Menon, F. Montorsi, et al. Retropubic, laparoscopic, and robot-assisted radical prostatectomy: a systematic review and cumulative analysis of comparative studies. *European Urology*, 55(5):1037–1063, 2009.

[40] B. Fischer and J. Modersitzki. Fast inversion of matrices arising in image processing. *Numerical Algorithms*, 22(1):1–11, 1999.

[41] B. Fischer and J. Modersitzki. A unified approach to fast image registration and a new curvature based registration technique. *Linear Algebra and its Applications*, 380:107–124, 2004.

[42] Z. Galil and J. Kiefer. D-optimum weighing designs. *The Annals of Statistics*, pages 1293–1306, 1980.

[43] Y. Gao, R. Sandhu, G. Fichtinger, and A. Tannenbaum. A coupled global registration and segmentation framework with application to magnetic resonance prostate imagery. *IEEE Transactions on Medical Imaging*, 29(10):1781–1794, 2010.

[44] P. Garteiser, R. S. Sahebjavaher, L. C. Ter Beek, S. Salcudean, V. Vilgrain, B. E. Van Beers, and R. Sinkus. Rapid acquisition of multifrequency, multislice and multidirectional MR elastography data with a fractionally encoded gradient echo sequence. *NMR in Biomedicine*, 26(10):1326–1335, 2013.

[45] E. Gibson, C. Crukley, M. Gaed, J. A. Gómez, M. Moussa, J. L. Chin, G. S. Bauman, A. Fenster, and A. D. Ward. Registration of prostate histology images to ex vivo MR images via strand-shaped fiducials. *Journal of Magnetic Resonance Imaging*, 36(6):1402–1412, 2012.

[46] K. J. Glaser, A. Manduca, and R. L. Ehman. Review of MR elastography applications and recent developments. *Journal of Magnetic Resonance Imaging*, 36(4):757–774, 2012.

[47] N. J. Gordon, D. J. Salmond, and A. F. Smith. Novel approach to nonlinear/non-gaussian bayesian state estimation. In *IEE Proceedings F (Radar and Signal Processing)*, volume 140, pages 107–113. IET, 1993.

[48] H. Gray, S. Standring, H. Ellis, and B. Berkovitz. *Gray's anatomy: the anatomical basis of clinical practice*. Gray's Anatomy: The Anatomical Basis of Clinical Practice. Elsevier Churchill Livingstone, 2005.

[49] H. Greenspan. Super-resolution in medical imaging. *The Computer Journal*, 52(1):43–63, 2009.

[50] J. Hadamard. Résolution d'une question relative aux déterminants. *Bulletin des Sciences Mathématiques*, 17(1):240–246, 1893.

[51] B. A. Hadaschik, T. H. Kuru, C. Tulea, P. Rieker, I. V. Popeneciu, T. Simpfendörfer, J. Huber, P. Zogal, D. Teber, S. Pahernik, et al. A novel stereotactic prostate biopsy system integrating pre-interventional magnetic resonance imaging and live ultrasound fusion. *The Journal of Urology*, 186(6):2214–2220, 2011.

[52] S. Haker, L. Zhu, A. Tannenbaum, and S. Angenent. Optimal mass transport for registration and warping. *International Journal of Computer Vision*, 60(3):225–240, 2004.

[53] R. Hartley and A. Zisserman. *Multiple View Geometry in Computer Vision*. Cambridge University Press, 2nd edition, 2004.

[54] R. Hausmann, J. S. Lewin, and G. Laub. Phase-contrast MR angiography with reduced acquisition time: New concepts in sequence design. *Journal of Magnetic Resonance Imaging*, 1(4):415–422, 1991.

[55] M. P. Heinrich, M. Jenkinson, M. Bhushan, T. Matin, F. V. Gleeson, S. M. Brady, and J. A. Schnabel. MIND: Modality independent neighbourhood descriptor for multi-modal deformable registration. *Medical Image Analysis*, 16(7):1423–1435, 2012.

[56] D. Herzka, M. Kotys, R. Sinkus, R. Pettigrew, and A. Gharib. Magnetic resonance elastography in the liver at 3 Tesla using a second harmonic approach. *Magnetic Resonance in Medicine*, 62(2):284–291, 2009.

[57] M. Honarvar, R. S. Sahebjavaher, S. E. Salcudean, and R. Rohling. Sparsity regularization in dynamic elastography. *Physics in Medicine and Biology*, 57(19):5909, 2012.

[58] B. K. P. Horn and B. G. Schunck. Determining optical flow. *Artificial Intelligence*, 17:185–203, 1981.

[59] Y. Hu, H. U. Ahmed, Z. Taylor, C. Allen, M. Emberton, D. Hawkes, and D. Barratt. MR to ultrasound registration for image-guided prostate interventions. *Medical Image Analysis*, 16(3):687–703, 2012.

[60] C. Hughes, O. Rouviere, F. Mege-Lechevallier, R. Souchon, and R. Prost. Robust alignment of prostate histology slices with quantified accuracy. *IEEE Transactions on Biomedical Engineering*, 60(2):281–291, 2013.

[61] M. Irani and S. Peleg. Improving resolution by image registration. *CVGIP: Graphical Models and Image Processing*, 53(3):231–239, 1991.

[62] M. Ishida, A. Schuster, S. Takase, G. Morton, A. Chiribiri, B. Bigalke, T. Schaeffter, H. Sakuma, and E. Nagel. Impact of an abdominal belt on breathing patterns and scan efficiency in whole-heart coronary magnetic resonance angiography: comparison between the uk and japan. *Journal of Cardiovascular Magnetic Resonance*, 13:71, 2011.

[63] R. S. John and N. R. Draper. D-optimality for regression designs: a review. *Technometrics*, 17(1):15–23, 1975.

[64] S. Kabus, A. Franz, and B. Fischer. Spatially varying elasticity in image registration. *Methods of Information in Medicine*, 46(3):287–291, 2007.

[65] T. Kailath, A. H. Sayed, and B. Hassibi. *Linear estimation*, volume 1. Prentice Hall New Jersey, 2000.

[66] M. Kass, A. Witkin, and D. Terzopoulos. Snakes: Active contour models. *International Journal of Computer Vision*, 1(4):321–331, 1988.

[67] S. Kichenassamy, A. Kumar, P. Olver, A. Tannenbaum, and A. Yezzi. Gradient flows and geometric active contour models. *International Conference on Computer Vision*, pages 810–815, 1995.

[68] J. Kiefer. Optimum designs in regression problems, ii. *The Annals of Mathematical Statistics*, pages 298–325, 1961.

[69] J. Kiefer and J. Wolfowitz. Optimum designs in regression problems. *The Annals of Mathematical Statistics*, pages 271–294, 1959.

[70] S. Kimm, T. Tarin, J. Lee, B. Hu, K. Jensen, D. Nishimura, and J. Brooks. Methods for registration of magnetic resonance images of ex vivo prostate specimens with histology. *Journal of Magnetic Resonance Imaging*, 2012.

[71] A. Kirkham, M. Emberton, and C. Allen. How good is MRI at detecting and characterising cancer within the prostate? *European Urology*, 50(6):1163–1175, 2006.

[72] D. Klatt, T. K. Yasar, T. J. Royston, and R. L. Magin. Sample interval modulation for the simultaneous acquisition of displacement vector data in magnetic resonance elastography: theory and application. *Physics in Medicine and Biology*, 58(24):8663–8675, 2013.

[73] I. Kolesov, J. Lee, P. Vela, and A. Tannenbaum. A stochastic approach for non-rigid image registration. *SPIE Medical Imaging*, 86550:U1–U15, 2013.

[74] K. Konig, U. Scheipers, A. Pesavento, A. Lorenz, H. Ermert, and T. Senge. Initial experiences with real-time elastography guided biopsies of the prostate. *The Journal of Urology*, 174(1):115–117, 2005.

[75] P. Kozlowski et al. Combined prostate diffusion tensor imaging and dynamic contrast enhanced MRI at 3T–quantitative correlation with biopsy. *Magnetic Resonance Imaging*, 28(5):621–628, 2010.

[76] C. Le Guyader and L. Vese. A combined segmentation and registration framework with a nonlinear elasticity smoother. *Computer Vision and Image Understanding*, 2011.

[77] R. V. Lenth. Some practical guidelines for effective sample size determination. *The American Statistician*, 55(3):187–193, 2001.

[78] H. Lester, S. Arridge, K. Jansons, L. Lemieux, J. Hajnal, and A. Oatridge. Non-linear registration with the variable viscosity fluid algorithm. In *Information Processing in Medical Imaging*, pages 238–251. Springer, 1999.

[79] J. Lobo. *Towards intra-operative dosimetry for prostate brachytherapy: improved seed detection and registration to ultrasound using needle detection*. PhD thesis, Electrical and Computer Engineering, University of British Columbia, Vancouver, BC, 2012.

[80] J.-A. Long, B. H. Lee, J. Guillotreau, R. Autorino, H. Laydner, R. Yakoubi, E. Rizkala, R. J. Stein, J. H. Kaouk, and G.-P. Haber. Real-time robotic transrectal ultrasound navigation during robotic radical prostatectomy: initial clinical experience. *Urology*, 80(3):608–613, 2012.

[81] Y. Lotan, J. A. Cadeddu, and M. T. Gettman. The new economics of radical prostatectomy: cost comparison of open, laparoscopic and robot assisted techniques. *The Journal of Urology*, 172(4):1431–1435, 2004.

[82] B. Ma and R. Ellis. Surface-based registration with a particle filter. *Medical Image Computing and Computer Assisted Intervention (MICCAI)*, pages 566–573, 2004.

[83] S. S. Mahdavi, M. Moradi, W. J. Morris, and S. E. Salcudean. Automatic prostate segmentation using fused ultrasound B-mode and elastography images. *Medical Image Computing and Computer Assisted Intervention (MICCAI)*, pages 76–83, 2010.

[84] J. Maintz and M. Viergever. A survey of medical image registration. *Medical Image Analysis*, 2(1):1–36, 1998.

[85] A. Manduca, T. E. Oliphant, M. Dresner, J. Mahowald, S. Kruse, E. Amromin, J. P. Felmlee, J. F. Greenleaf, and R. L. Ehman. Magnetic resonance elastography: non-invasive mapping of tissue elasticity. *Medical Image Analysis*, 5(4):237–254, 2001.

[86] L. Marks, S. Young, and S. Natarajan. MRI–ultrasound fusion for guidance of targeted prostate biopsy. *Current opinion in urology*, 23(1):43, 2013.

[87] S. Martin, M. Baumann, V. Daanen, and J. Troccaz. MR prior based automatic segmentation of the prostate in TRUS images for MR/TRUS data fusion. In *IEEE International Symposium on Biomedical Imaging*, pages 640–643. IEEE, 2010.

[88] A. Mejia-Rodriguez, E. Arce-Santana, E. Scalco, D. Tresoldi, M. Mendez, A. Bianchi, G. Cattaneo, and G. Rizzo. Elastic registration based on particle filter in radiotherapy images with brain deformations. In *Engineering in Medicine and Biology Society (EMBC)*, pages 8049–8052. IEEE, 2011.

[89] M. Menon, A. Tewari, B. Baize, B. Guillonneau, and G. Vallancien. Prospective comparison of radical retropubic prostatectomy and robot-assisted anatomic prostatectomy: the vattikuti urology institute experience. *Urology*, 60(5):864–868, 2002.

[90] J. Mitra, Z. Kato, R. Martí, A. Oliver, X. Lladó, D. Sidibé, S. Ghose, J. C. Vilanova, J. Comet, and F. Meriaudeau. A spline-based non-linear diffeomorphism for multimodal prostate registration. *Medical Image Analysis*, 16(6):1259–1279, 2012.

[91] T. Miyagawa, S. Ishikawa, T. Kimura, T. Suetomi, M. Tsutsumi, T. Irie, M. Kondoh, and T. Mitake. Real-time virtual sonography for navigation during targeted prostate biopsy using magnetic resonance imaging data. *International Journal of Urology*, 17(10):855–860, 2010.

[92] J. Modersitzki. *Numerical methods for image registration.* Oxford University Press, USA, 2004.

[93] H. Moghari, M. and P. Abolmaesumi. Point-based rigid-body registration using an unscented Kalman filter. *IEEE Transactions on Image Processing*, 26(12):1708–1728, Dec. 2007.

[94] O. Mohareri, M. Ramezani, T. K. Adebar, P. Abolmaesumi, and S. E. Salcudean. Automatic localization of the da vinci surgical instrument tips in 3-d transrectal ultrasound. *IEEE Transactions on Biomedical Engineering*, 60(9):2663–2672, 2013.

[95] O. Mohareri, A. Ruszkowski, J. Lobo, J. Ischia, A. Baghani, G. Nir, H. Eskandari, E. Jones, L. Fazli, L. Goldenberg, et al. Multi-parametric 3D quantitative ultrasound vibro-elastography imaging for detecting palpable prostate tumors. *Medical Image Computing and Computer Assisted Intervention (MICCAI)*, pages 561–568, 2014.

[96] A. M. Mood. On hotelling's weighing problem. *The Annals of Mathematical Statistics*, 17(4):432–446, 1946.

[97] C. M. Moore, N. L. Robertson, N. Arsanious, T. Middleton, A. Villers, L. Klotz, S. S. Taneja, and M. Emberton. Image-guided prostate biopsy using magnetic resonance imaging–derived targets: a systematic review. *European Urology*, 63(1):125–140, 2013.

[98] M. Moradi, S. S. Mahdavi, G. Nir, O. Mohareri, A. Koupparis, L.-O. Gagnon, L. Fazli, R. G. Casey, J. Ischia, E. C. Jones, et al. Multiparametric 3d in vivo ultrasound vibroelastography imaging of prostate cancer: Preliminary results. *Medical Physics*, 41(7):073505, 2014.

[99] P. S. Moran, M. O'Neill, C. Teljeur, M. Flattery, L. A. Murphy, G. Smyth, and M. Ryan. Robot-assisted radical prostatectomy compared with open and laparoscopic approaches: A systematic review and meta-analysis. *International Journal of Urology*, 20(3):312–321, 2013.

[100] R. Muthupillai, D. Lomas, P. Rossman, J. Greenleaf, A. Manduca, and R. Ehman. Magnetic resonance elastography by direct visualization of propagating acoustic strain waves. *Science*, 269(5232):1854–1857, 1995.

[101] R. Narayanan, J. Kurhanewicz, K. Shinohara, E. Crawford, A. Simoneau, and J. Suri. MRI-ultrasound registration for targeted prostate biopsy. *IEEE International Symposium on Biomedical Imaging*, pages 991–994, 2009.

[102] G. Nir, R. S. Sahebjavaher, A. Baghani, R. Sinkus, and S. E. Salcudean. Prostate segmentation in MRI using fused T2-weighted and elastography images. *SPIE Medical Imaging*, 90340:C1–C6, 2014.

[103] G. Nir, R. S. Sahebjavaher, P. Kozlowski, S. D. Chang, R. Sinkus, S. L. Goldenberg, and S. E. Salcudean. Model-based registration of ex vivo and in vivo MRI of the prostate using elastography. *IEEE Transactions on Medical Imaging*, 32(7):1349–1361, 2013.

[104] G. Nir, R. S. Sahebjavaher, R. Sinkus, and S. E. Salcudean. A framework for optimization-based design of motion encoding in magnetic resonance elastography. *Magnetic Resonance in Medicine*, 2014.

[105] G. Nir and A. Tannenbaum. Temporal registration of partial data using particle filtering. In *IEEE International Conference on Image Processing*, pages 2177–2180. IEEE, 2011.

[106] K. Noe and T. Sørensen. Solid mesh registration for radiotherapy treatment planning. *Biomedical Simulation*, pages 59–70, 2010.

[107] T. E. Oliphant, A. Manduca, R. L. Ehman, and J. F. Greenleaf. Complex-valued stiffness reconstruction for magnetic resonance elastography by algebraic inversion of the differential equation. *Magnetic Resonance in Medicine*, 45(2):299–310, 2001.

[108] J. Ophir, I. Céspedes, H. Ponnekanti, Y. Yazdi, and X. Li. Elastography: a quantitative method for imaging the elasticity of biological tissues. *Ultrasonic Imaging*, 13(2):111–134, 1991.

[109] S. Osher and J. A. Sethian. Fronts propagating with curvature-dependent speed: algorithms based on hamilton-jacobi formulations. *Journal of Computational Physics*, 79(1):12–49, 1988.

[110] N. F. Osman, E. R. McVeigh, and J. L. Prince. Imaging heart motion using harmonic phase MRI. *IEEE Transactions on Medical Imaging*, 19(3):186–202, 2000.

[111] Y. Ou, D. Shen, M. Feldman, J. Tomaszewski, and C. Davatzikos. Non-rigid registration between histological and MR images of the prostate: a joint segmentation and registration framework. In *IEEE Conference on Computer Vision and Pattern Recognition Workshops*, pages 125–132. IEEE, 2009.

[112] S. Papazoglou, J. Rump, J. Braun, and I. Sack. Shear wave group velocity inversion in MR elastography of human skeletal muscle. *Magnetic Resonance in Medicine*, 56(3):489–497, 2006.

[113] S. C. Park, M. K. Park, and M. G. Kang. Super-resolution image reconstruction: a technical overview. *Signal Processing Magazine, IEEE*, 20(3):21–36, 2003.

[114] A. W. Partin, M. W. Kattan, E. N. Subong, P. C. Walsh, K. J. Wojno, J. E. Oesterling, P. T. Scardino, and J. Pearson. Combination of prostate-specific antigen, clinical stage, and gleason score to predict pathological stage of localized prostate cancer: a multi-institutional update. *The Journal of the American Medical Association (JAMA)*, 277(18):1445–1451, 1997.

[115] V. R. Patel, R. Thaly, and K. Shah. Robotic radical prostatectomy: outcomes of 500 cases. *BJU international*, 99(5):1109–1112, 2007.

[116] N. J. Pelc, M. A. Bernstein, A. Shimakawa, and G. H. Glover. Encoding strategies for three-direction phase-contrast MR imaging of flow. *Journal of Magnetic Resonance Imaging*, 1(4):405–413, 1991.

[117] X. Pennec and J. Thirion. A framework for uncertainty and validation of 3-d registration methods based on points and frames. *International Journal of Computer Vision*, 25(3):203–229, 1997.

[118] A. Pesavento and A. Lorenz. Real time strain imaging and in-vivo applications in prostate cancer. *IEEE Ultrasonics Symposium*, 2:1647–1652, 2001.

[119] C. Phillips. Tracking the rise of robotic surgery for prostate cancer. *NCI Cancer Bulletin*, 8(16), 2011.

[120] P. A. Pinto, P. H. Chung, A. R. Rastinehad, A. A. Baccala Jr, J. Kruecker, C. J. Benjamin, S. Xu, P. Yan, S. Kadoury, C. Chua, et al. Magnetic resonance imaging/ultrasound fusion guided prostate biopsy improves cancer detection following transrectal ultrasound biopsy and correlates with multiparametric magnetic resonance imaging. *The Journal of Urology*, 186(4):1281–1285, 2011.

[121] J. G. Pipe et al. Motion correction with PROPELLER MRI: application to head motion and free-breathing cardiac imaging. *Magnetic Resonance in Medicine*, 42(5):963–969, 1999.

[122] J. P. W. Pluim, J. B. A. Maintz, and M. A. Viergever. Mutual information based registration of medical images: a survey. *IEEE Transactions on Medical Imaging*, 22:986–1004, 2003.

[123] W. H. Press, S. A. Teukolsky, W. T. Vetterling, and B. P. Flannery. *Numerical Recipes 3rd Edition: The Art of Scientific Computing.* Cambridge University Press, New York, NY, USA, 3 edition, 2007.

[124] F. Pukelsheim. *Optimal design of experiments*, volume 50. SIAM, 1993.

[125] Y. Rathi, N. Vaswani, and A. Tannenbaum. A generic framework for tracking using particle filter with dynamic shape prior. *IEEE Transactions on Image Processing*, 16(5):1370–1382, 2007.

[126] C. Reynier, J. Troccaz, P. Fourneret, A. Dusserre, C. Gay-Jeune, J.-L. Descotes, M. Bolla, and J.-Y. Giraud. MRI/TRUS data fusion for prostate brachytherapy. preliminary results. *Medical Physics*, 31(6):1568–1575, 2004.

[127] M. D. Robson, J. C. Gore, and R. T. Constable. Measurement of the point spread function in MRI using constant time imaging. *Magnetic Resonance in Medicine*, 38(5):733–740, 1997.

[128] K. Rohr, H. Stiehl, R. Sprengel, T. Buzug, J. Weese, and M. Kuhn. Landmark-based elastic registration using approximating thin-plate splines. *IEEE Transactions on Medical Imaging*, 20(6):526–534, 2001.

[129] O. Rouvière, C. Reynolds, T. Hulshizer, P. Rossman, Y. Le, J. P. Felmlee, and R. L. Ehman. MR histological correlation: a method for cutting specimens along the imaging plane in animal or ex vivo experiments. *Journal of Magnetic Resonance Imaging*, 23(1):60–69, 2006.

[130] D. Rueckert, L. Sonoda, C. Hayes, D. Hill, M. Leach, and D. Hawkes. Nonrigid registration using free-form deformations: application to breast MR images. *IEEE Transactions on Medical Imaging*, 18(8):712–721, 1999.

[131] J. Rump, D. Klatt, J. Braun, C. Warmuth, and I. Sack. Fractional encoding of harmonic motions in MR elastography. *Magnetic Resonance in Medicine*, 57(2):388–395, 2007.

[132] L. Ruthotto, S. Mohammadi, and N. Weiskopf. A new method for joint susceptibility artefact correction and super-resolution for dMRI. *SPIE Medical Imaging*, 90340:P1–P4, 2014.

[133] I. Sack, C. K. Mcgowan, A. Samani, C. Luginbuhl, W. Oakden, and D. B. Plewes. Observation of nonlinear shear wave propagation using magnetic resonance elastography. *Magnetic Resonance in Medicine*, 52(4):842–850, 2004.

[134] R. S. Sahebjavaher, A. Baghani, M. Honarvar, R. Sinkus, and S. E. Salcudean. Transperineal prostate MR elastography: initial in vivo results. *Magnetic Resonance in Medicine*, 69(2):411–420, 2013.

[135] R. S. Sahebjavaher, S. Frew, A. Bylinskii, L. Beek, P. Garteiser, M. Honarvar, R. Sinkus, and S. E. Salcudean. Prostate MR elastography with transperineal electromagnetic actuation and a fast fractionally encoded steady-state gradient echo sequence. *NMR in Biomedicine*, 27(7):784–794, 2014.

[136] R. S. Sahebjavaher, P. Garteiser, B. Van Beers, S. E. Salcudean, and R. Sinkus. Rapid 3D motion-encoding using spoiled FFE: application towards multi-frequency MR rheology in liver. In *European Society for Magnetic Resonance in Medicine and Biology*, page 124, 2011.

[137] R. S. Sahebjavaher, G. Nir, M. Honarvar, L. O. Gagnon, J. Ischa, E. C. Jones, S. D. Chang, L. Fazli, S. L. Goldenberg, R. Rohling, P. Kozlowski, R. Sinkus, and S. E. Salcudean. MR elastography of prostate cancer: quantitative comparison to histopathology, repeatability of methods. *NMR in Biomedicine*, 28(1):124–139, 2015.

[138] R. S. Sahebjavaher, G. Nir, M. Honarvar, E. C. Jones, S. D. Chang, L. O. Gagnon, J. Ischa, A. Yung, L. Fazli, S. L. Goldenberg, R. Rohling, R. Sinkus, P. Kozlowski, and S. E. Salcudean. MR elastography and diffusion-weighted imaging of ex vivo prostate cancer: quantitative comparison to histopathology. *NMR in Biomedicine*, 28(1):89–100, 2015.

[139] S. Salcudean, D. French, S. Bachmann, R. Zahiri-Azar, X. Wen, and W. Morris. Viscoelasticity modeling of the prostate region using vibro-elastography. *Medical Image Computing and Computer Assisted Intervention (MICCAI)*, pages 389–396, 2006.

[140] S. E. Salcudean, R. S. Sahebjavaher, O. Goksel, A. Baghani, S. S. Mahdavi, G. Nir, R. Sinkus, and M. Moradi. Biomechanical modeling of the prostate for procedure guidance and simulation. In Y. Payan, editor, *Soft Tissue Biomechanical Modeling for Computer Assisted Surgery*, volume 11 of *Studies in Mechanobiology, Tissue Engineering and Biomaterials*, pages 169–198. Springer Berlin Heidelberg, 2012.

[141] R. Sandhu, S. Dambreville, and A. Tannenbaum. Point set registration via particle filtering and stochastic dynamics. *IEEE Transactions on Pattern Analysis and Machine Intelligence*, 32(8):1459–1473, 2010.

[142] S. Sara Mahdavi, N. Chng, I. Spadinger, W. J. Morris, and S. E. Salcudean. Semi-automatic segmentation for prostate interventions. *Medical Image Analysis*, 15(2):226–237, 2011.

[143] S. Sara Mahdavi, M. Moradi, X. Wen, W. Morris, and S. Salcudean. Evaluation of visualization of the prostate gland in vibro-elastography images. *Medical Image Analysis*, 15(4):589–600, 2011.

[144] K. Scheffler. Superresolution in MRI? *Magnetic Resonance in Medicine*, 48(2):408–408, 2002.

[145] A. Schned, K. Wheeler, C. Hodorowski, J. Heaney, M. Ernstoff, R. Amdur, and R. Harris. Tissue-shrinkage correction factor in the calculation of prostate cancer volume. *The American Journal of Surgical Pathology*, 20(12):1501–1506, 1996.

[146] B. Schölkopf and A. J. Smola. *Learning with kernels: Support vector machines, regularization, optimization, and beyond.* MIT press, 2002.

[147] J. A. Sethian. *Level Set Methods and Fast Marching Methods Evolving Interfaces in Computational Geometry, Fluid Mechanics, Computer Vision, and Materials Science.* Cambridge University Press, New York, second edition, 1999.

[148] V. Shah, T. Pohida, B. Turkbey, H. Mani, M. Merino, P. Pinto, P. Choyke, and M. Bernardo. A method for correlating in vivo prostate magnetic resonance imaging and histopathology using individualized magnetic resonance-based molds. *Review of Scientific Instruments*, 80:104301, 2009.

[149] M. M. Siddiqui, S. Rais-Bahrami, H. Truong, L. Stamatakis, S. Vourganti, J. Nix, A. N. Hoang, A. Walton-Diaz, B. Shuch, M. Weintraub, et al. Magnetic resonance imaging/ultrasound–fusion biopsy significantly upgrades prostate cancer versus systematic 12-core transrectal ultrasound biopsy. *European Urology*, 64(5):713–719, 2013.

[150] R. Sinkus, J. Lorenzen, D. Schrader, M. Lorenzen, M. Dargatz, and D. Holz. High-resolution tensor MR elastography for breast tumour detection. *Physics in Medicine and Biology*, 45:1649–1664, 2000.

[151] R. Sinkus, M. Tanter, S. Catheline, J. Lorenzen, C. Kuhl, E. Sondermann, and M. Fink. Imaging anisotropic and viscous properties of breast tissue by magnetic resonance-elastography. *Magnetic Resonance in Medicine*, 53(2):372–387, 2005.

[152] S. Smith, K. Wallner, G. Merrick, W. Butler, S. Sutlief, and P. Grimm. Interpretation of pre- versus postimplant TRUS images. *Medical Physics*, 30(5):920–924, 2003.

[153] S.-E. Song, N. B. Cho, G. Fischer, N. Hata, C. Tempany, G. Fichtinger, and I. Iordachita. Development of a pneumatic robot for MRI-guided transperineal prostate biopsy and brachytherapy: New approaches. In *IEEE International Conference on Robotics and Automation (ICRA)*, pages 2580–2585. IEEE, 2010.

[154] A. Sotiras, C. Davatzikos, and N. Paragios. Deformable medical image registration: A survey. *IEEE Transactions on Medical Imaging*, 32(7):1153–1190, 2013.

[155] Stanford University Computer Graphics Laboratory. The Stanford 3D scanning repository. `http://graphics.stanford.edu/data/3Dscanrep/` (retrieved on November 16, 2012).

[156] Y. Sun, J. Yuan, M. Rajchl, W. Qiu, C. Romagnoli, and A. Fenster. Efficient convex optimization approach to 3D non-rigid MR-TRUS registration. *Medical Image Computing and Computer Assisted Intervention (MICCAI)*, pages 195–202, 2013.

[157] F. Taquee, O. Goksel, S. Mahdavi, M. Keyes, W. Morris, I. Spadinger, and S. Salcudean. Deformable prostate registration from MR and TRUS images using surface error driven FEM models. *SPIE Medical Imaging*, 831612:1–10, 2012.

[158] L. Taylor, B. Porter, G. Nadasdy, P. di Sant'Agnese, D. Pasternack, Z. Wu, R. Baggs, D. Rubens, and K. Parker. Three-dimensional registration of prostate images from histology and ultrasound. *Ultrasound in Medicine & Biology*, 30(2):161–168, 2004.

[159] C. Tempany, S. Straus, N. Hata, and S. Haker. MR-guided prostate interventions. *Journal of Magnetic Resonance Imaging*, 27(2):356–367, 2008.

[160] G. M. Treece, R. W. Prager, and A. H. Gee. Stradwin. `http://mi.eng.cam.ac.uk/~rwp/stradwin/` (retrieved on July 12, 2011). Medical Imaging Group, Machine Intelligence Laboratory, Cambridge University, UK.

[161] G. M. Treece, R. W. Prager, and A. H. Gee. Regularised marching tetrahedra: improved iso-surface extraction. *Computers & Graphics*, 23(4):583–598, 1999.

[162] H. Trivedi, B. Turkbey, A. Rastinehad, C. Benjamin, M. Bernardo, T. Pohida, V. Shah, M. Merino, B. Wood, W. Linehan, et al. Use of patient-specific MRI-based prostate mold for validation of multiparametric MRI in localization of prostate cancer. *Urology*, 79(1):233–239, 2012.

[163] A. Tsai, A. Yezzi Jr, W. Wells, C. Tempany, D. Tucker, A. Fan, W. Grimson, and A. Willsky. A shape-based approach to the segmentation of medical imagery using level sets. *IEEE Transactions on Medical Imaging*, 22(2):137–154, 2003.

[164] O. Ukimura, M. M. Desai, S. Palmer, S. Valencerina, M. Gross, A. L. Abreu, M. Aron, and I. S. Gill. 3-dimensional elastic registration system of prostate biopsy location by real-time 3-dimensional transrectal ultrasound guidance with magnetic resonance/transrectal ultrasound image fusion. *The Journal of Urology*, 187(3):1080–1086, 2012.

[165] P. Viola and W. M. Wells III. Alignment by maximization of mutual information. *International Journal of Computer Vision*, 24(2):137–154, 1997.

[166] H. Wang, J. B. Weaver, M. M. Doyley, F. E. Kennedy, and K. D. Paulsen. Optimized motion estimation for MRE data with reduced motion encodes. *Physics in Medicine and Biology*, 53(8):2181–2196, 2008.

[167] A. Ward, C. Crukley, C. McKenzie, J. Montreuil, E. Gibson, J. Gomez, M. Moussa, G. Bauman, and A. Fenster. Registration of in vivo prostate magnetic resonance images to digital histopathology images. *Prostate Cancer Imaging. Computer-Aided Diagnosis, Prognosis, and Intervention*, pages 66–76, 2010.

[168] A. Ward, C. Crukley, C. McKenzie, J. Montreuil, E. Gibson, C. Romagnoli, J. Gomez, M. Moussa, J. Chin, G. Bauman, et al. Prostate: Registration of digital histopathologic images to in vivo MR images acquired by using endorectal receive coil. *Radiology*, 263(3):856–864, 2012.

[169] W. Wein, S. Brunke, A. Khamene, M. R. Callstrom, and N. Navab. Automatic CT-ultrasound registration for diagnostic imaging and image-guided intervention. *Medical Image Analysis*, 12(5):577–585, 2008.

[170] M. White, D. Hawkes, A. Melbourne, D. Collins, C. Coolens, M. Hawkins, M. Leach, and D. Atkinson. Motion artifact correction in free-breathing abdominal MRI using overlapping partial samples to recover image deformations. *Magnetic Resonance in Medicine*, 62(2):440–449, 2009.

[171] G. Xiao, B. Bloch, J. Chappelow, E. Genega, N. Rofsky, R. Lenkinski, J. Tomaszewski, M. Feldman, M. Rosen, and A. Madabhushi. Determining histology-MRI slice correspondences for defining MRI-based disease signatures of prostate cancer. *Computerized Medical Imaging and Graphics*, 35(7):568–578, 2011.

[172] H. Xu, A. Lasso, S. Vikal, P. Guion, A. Krieger, A. Kaushal, L. Whitcomb, and G. Fichtinger. MRI-guided robotic prostate biopsy: A clinical accuracy validation. *Medical Image Computing and Computer Assisted Intervention (MICCAI)*, pages 383–391, 2010.

[173] T. K. Yasar, D. Klatt, R. L. Magin, and T. J. Royston. Selective spectral displacement projection for multifrequency MRE. *Physics in Medicine and Biology*, 58(16):5771, 2013.

[174] A. Yezzi, A. Tsai, and A. Willsky. A statistical approach to snakes for bimodal and trimodal imagery. *International Conference on Computer Vision*, 2:898–903, 1999.

[175] Y. Zhan, Y. Ou, M. Feldman, J. Tomaszeweski, C. Davatzikos, and D. Shen. Registering histological and MR images of prostate for image-based cancer detection. *Academic Radiology*, 14(11):1367, 2007.

[176] O. Zienkiewicz and R. Taylor. *The finite element method for solid and structural mechanics*, volume 2. Butterworth-Heinemann, 2005.

Appendix A

Derivation of the Parameterized Phase Accumulation

Here we derive expressions of the parameterized phase accumulation. Based on the Larmor precession, we calculate the phase accumulated by each isochromat at $\bar{r}$ that moves according to the wave displacement $\bar{\Psi}$ under the MEGs $\bar{G}$ (excluding the constant phase accumulated by the static magnetic field $\bar{B}_0$). We have that

$$\begin{aligned}
\Phi(\bar{r};\omega_i,\bar{N},|\bar{\mathcal{G}}|,\bar{\alpha},\bar{\beta}) &= \gamma\int_{-\infty}^{\infty}\bar{G}(t;\bar{\omega},\bar{N},|\bar{\mathcal{G}}|,\bar{\alpha},\bar{\beta})\cdot\bar{r}(t)\,dt\\
&= \gamma\int_{-\infty}^{\infty}\bar{G}(t;\bar{\omega},\bar{N},|\bar{\mathcal{G}}|,\bar{\alpha},\bar{\beta})\cdot\big(\bar{r}+\bar{\Psi}(\bar{r},t)\big)\ dt\\
&= \sum_{i=x,y,z}\Phi_i(\bar{r};\omega_i,N_i,|\mathcal{G}_i|,\alpha_i,\beta_i)
\end{aligned}$$

By using (6.1) and (6.2), the elements in $\bar{G}\cdot\bar{r}$ are cancelled (integration of a constant multiplied by sinusoid over its time period). For $i = x, y, z$, we have the individual phase accumulations

$$\begin{aligned}
\Phi_i(\bar{r};\omega_i,N_i,|\mathcal{G}_i|,\alpha_i,\beta_i) &= \gamma\int_{\alpha_i/\omega_i}^{\alpha_i/\omega_i+N_iT_i}|\xi_i(\bar{r})|\sin\left(\omega_m t+\varphi_i(\bar{r})\right)|\mathcal{G}_i|\sin\left(\omega_i t-\alpha_i+\beta_i\right)dt\\
&= \frac{\gamma}{2}|\mathcal{G}_i||\xi_i(\bar{r})|\int_{\alpha_i/\omega_i}^{\alpha_i/\omega_i+N_iT_i}[\cos\left((\omega_m-\omega_i)t+\varphi_i(\bar{r})+\alpha_i-\beta_i\right)\\
&\quad-\cos\left((\omega_m+\omega_i)t+\varphi_i(\bar{r})-\alpha_i+\beta_i\right)]\ dt
\end{aligned}$$

In case $\omega_i = \omega_m$, the second cosine is cancelled in the integration and we have

$$\Phi_i(\bar{r};N_i,|\mathcal{G}_i|,\alpha_i,\beta_i) = \frac{\gamma\pi N_i|\mathcal{G}_i|}{\omega_m}|\xi_i(\bar{r})|\cos\left(\varphi_i(\bar{r})+\alpha_i-\beta_i\right)$$

Otherwise, for $\omega_i > \omega_m$, i.e., $q_i = \omega_m/\omega_i < 1$, $i = x, y, z$, we have

$$\begin{aligned}
\Phi_i(\bar{r}; q_i < 1, N_i, |\mathcal{G}_i|, \alpha_i, \beta_i) &= \frac{\gamma}{2}|\mathcal{G}_i||\xi_i(\bar{r})| \left[\frac{1}{(\omega_m - \omega_i)} \sin\left((\omega_m - \omega_i)t + \varphi_i(\bar{r}) + \alpha_i - \beta_i\right)\right. \\
&\qquad \left. - \frac{1}{(\omega_m + \omega_i)} \sin\left((\omega_m + \omega_i)t + \varphi_i(\bar{r}) - \alpha_i + \beta_i\right)\right]_{t=\alpha_i/\omega_i}^{\alpha_i/\omega_i + N_i T_i} \\
&= \frac{\gamma}{2\omega_i}|\mathcal{G}_i||\xi_i(\bar{r})| \left[\frac{1}{(q_i - 1)} \left[\sin\left(q_i(\alpha_i + 2\pi N_i) + \varphi_i(\bar{r}) - \beta_i\right) - \sin\left(q_i\alpha_i + \varphi_i(\bar{r}) - \beta_i\right)\right]\right. \\
&\qquad \left. - \frac{1}{(q_i + 1)} \left[\sin\left(q_i(\alpha_i + 2\pi N_i) + \varphi_i(\bar{r}) + \beta_i\right) - \sin\left(q_i\alpha_i + \varphi_i(\bar{r}) + \beta_i\right)\right]\right] \\
&= \frac{\gamma}{\omega_i}|\mathcal{G}_i||\xi_i(\bar{r})| \sin\left(\pi q_i N_i\right) \left[\frac{1}{(q_i - 1)} \cos\left(q_i\alpha_i + \varphi_i(\bar{r}) - \beta_i + \pi q_i N_i\right)\right. \\
&\qquad \left. - \frac{1}{(q_i + 1)} \cos\left(q_i\alpha_i + \varphi_i(\bar{r}) + \beta_i + \pi q_i N_i\right)\right] \\
&= \frac{\gamma}{\omega_m}|\mathcal{G}_i||\xi_i(\bar{r})| \sin\left(\pi q_i N_i\right) \frac{-q_i}{(1 - q_i^2)} \left[(1 + q_i) \cos\left(q_i\alpha_i + \varphi_i(\bar{r}) - \beta_i + \pi q_i N_i\right)\right. \\
&\qquad \left. + (1 - q_i) \cos\left(q_i\alpha_i + \varphi_i(\bar{r}) + \beta_i + \pi q_i N_i\right)\right] \\
&= \frac{\gamma}{\omega_m}|\mathcal{G}_i||\xi_i(\bar{r})| \sin\left(\pi q_i N_i\right) \frac{-2q_i}{(1 - q_i^2)} \left[\cos\left(\beta_i\right) \cos\left(q_i\alpha_i + \varphi_i(\bar{r}) + \pi q_i N_i\right)\right. \\
&\qquad \left. + q_i \sin\left(\beta_i\right) \sin\left(q_i\alpha_i + \varphi_i(\bar{r}) + \pi q_i N_i\right)\right] \\
&= \frac{\gamma}{\omega_m}|\mathcal{G}_i| \sin\left(\pi q_i N_i\right) \frac{-2q_i \operatorname{sign}(\cos\left(\beta_i\right))}{(1 - q_i^2)} \sqrt{\cos^2\left(\beta_i\right) + q_i^2 \sin^2\left(\beta_i\right)} \\
&\qquad \cdot |\xi_i(\bar{r})| \cos\left(q_i\alpha_i + \varphi_i(\bar{r}) + \pi q_i N_i - \arctan\left(q_i \tan\left(\beta_i\right)\right)\right) \\
&= \frac{-2\gamma q_i \cos\left(\beta_i\right) \sin\left(\pi q_i N_i\right) |\mathcal{G}_i|}{\omega_m(1 - q_i^2)} \sqrt{1 + q_i^2 \tan^2\left(\beta_i\right)} \\
&\qquad \cdot |\xi_i(\bar{r})| \cos\left(q_i\alpha_i + \varphi_i(\bar{r}) + \pi q_i N_i - \arctan\left(q_i \tan\left(\beta_i\right)\right)\right), \quad i = x, y, z
\end{aligned}$$

where we have used trigonometric identities and the harmonic addition theorem.

Specifically, the phase accumulation for $q_i < 1$ when $\beta_i = \{0, \pi\}$ (no discontinuities) is

$$\Phi(\bar{r}; \bar{q} < 1, \bar{N}, |\bar{\mathcal{G}}|, \bar{\alpha}, \bar{\beta} = \{0, \pi\}) = \sum_{i=x,y,z} \frac{\mp 2\gamma q_i \sin\left(\pi q_i N_i\right)}{\omega_m(1 - q_i^2)} |\mathcal{G}_i||\xi_i(\bar{r})| \cos\left(q_i\alpha_i + \varphi_i(\bar{r}) + \pi q_i N_i\right)$$

with a '$-$' sign when $\beta_i = 0$, and a '$+$' sign when $\beta_i = \pi$. The term

$$\frac{\mp 2\gamma q_i \sin\left(\pi q_i N_i\right)}{\omega_m(1 - q_i^2)} |\mathcal{G}_i|$$

is also known as the encoding efficiency [131], and we note that it depends on q_i.